The SAMI Galaxy Survey: The internal orbital structure and mass distribution of passive galaxies from triaxial orbit-superposition Schwarzschild models

Giulia Santucci,[1,2] Sarah Brough,[1,2] Jesse van de Sande,[3,2] Richard M. McDermid,[4,5,2] Glenn van de Ven,[6]
Ling Zhu,[7] Francesco D'Eugenio,[8,9] Joss Bland-Hawthorn,[3,2] Stefania Barsanti,[10,2] Julia J. Bryant,[3,2,11]
Scott M. Croom,[3,2] Roger L. Davies,[12] Andrew W. Green,[13] Jon S. Lawrence,[14] Nuria P.F. Lorente,[14]
Matt S. Owers,[15,5,2] Adriano Poci,[16,5] Samuel N. Richards,[3] Sabine Thater,[6] and Sukyoung Yi[17]

[1]School of Physics, University of New South Wales, NSW 2052, Australia
[2]ARC Centre of Excellence for All Sky Astrophysics in 3 Dimensions (ASTRO 3D)
[3]Sydney Institute for Astronomy, School of Physics, University of Sydney, NSW 2006, Australia
[4]School of Mathematical and Physical Science, Macquarie University, NSW 2109, Australia
[5]Astronomy, Astrophysics and Astrophotonics Research Centre, Macquarie University, Sydney, NSW 2109, Australia
[6]Department of Astrophysics, University of Vienna, Türkenschanzstrasse 17, 1180 Vienna, Austria
[7]Shanghai Astronomical Observatory, Chinese Academy of Sciences, 80 Nandan Road, Shanghai 200030, China
[8]Cavendish Laboratory and Kavli Institute for Cosmology, University of Cambridge, Madingley Rise, Cambridge, CB3 0HA, United Kingdom
[9]Sterrenkundig Observatorium, Universiteit Gent, Krijgslaan 281 S9, B-9000 Gent, Belgium
[10]Research School of Astronomy and Astrophysics, The Australian National University, Canberra, ACT 2611, Australia
[11]Australian Astronomical Optics, AAO-USydney, School of Physics, University of Sydney, NSW 2006, Australia
[12]Astrophysics, Department of Physics, University of Oxford, Denys Wilkinson Building, Keble Rd., Oxford, OX1 3RH, UK
[13]Atlassian, C/O Scott Croom, University of Sydney, NSW 2006 Australia
[14]Australian Astronomical Optics, Faculty of Science & Engineering, Macquarie University. 105 Delhi Rd, North Ryde, NSW 2113, Australia
[15]Department of Physics and Astronomy, Macquarie University, NSW 2109, Australia
[16]Centre for Extragalactic Astronomy, University of Durham, Stockton Road, Durham DH1 3LE, United Kingdom
[17]Department of Astronomy and Yonsei University Observatory, Yonsei University, Seoul 03722, Republic of Korea

ABSTRACT

Dynamical models are crucial for uncovering the internal dynamics of galaxies, however, most of the results to date assume axisymmetry, which is not representative for a significant fraction of massive galaxies. Here, we build triaxial Schwarschild orbit-superposition models of galaxies taken from the SAMI Galaxy Survey, in order to reconstruct their inner orbital structure and mass distribution. The sample consists of 161 passive galaxies with total stellar masses in the range $10^{9.5}$ to $10^{12} M_\odot$. We find that the changes in internal structures within $1R_e$ are correlated with the total stellar mass of the individual galaxies. **The majority of the galaxies in the sample ($73\% \pm 3\%$) are oblate, while $19\% \pm 3\%$ are mildly triaxial and $8\% \pm 3\%$ have triaxial/prolate shape. Galaxies with $\log M_\star/M_\odot > 10.50$ are more likely to be non-oblate. We find a mean dark matter fraction of $f_{\rm DM} = 0.28 \pm 0.20$, within $1R_e$.** Galaxies with higher intrinsic ellipticity (flatter) are found to have more negative velocity anisotropy β_r (tangential anisotropy). β_r also shows an anti-correlation with the edge-on spin parameter $\lambda_{Re,EO}$, so that β_r decreases with increasing $\lambda_{Re,EO}$, reflecting the contribution from disk-like orbits in flat, fast-rotating galaxies. We see evidence of an increasing fraction of hot orbits with increasing stellar mass, while warm and cold orbits show a decreasing trend. We also find that galaxies with different (V/σ - h_3) kinematic signatures have distinct combinations of orbits. These results are in agreement with a formation scenario in which slow- and fast-rotating galaxies form through two main channels.

Corresponding author: Giulia Santucci
g.santucci@student.unsw.edu.au

1. INTRODUCTION

The assembly history of a galaxy is thought to be one of the major factors that determines its internal kinematic structure (e.g., White 1979; Fall & Efstathiou

1980; Park et al. 2019) and so observations of the internal kinematic structure should give an indication of a galaxy's past.

Our current understanding of galaxy formation suggests that massive galaxies form in a two-phase process (e.g., Naab et al. 2009; Oser et al. 2010). During the first phase, at high redshift, they grow by a rapid episode of in-situ star formation, resulting in compact massive systems. After $z \approx 2$, these massive, $\log_{10}(M_\star/M_\odot) > 10.5$, compact galaxies are predicted to be quiescent and grow mostly by accreting mass through gas-poor galaxy mergers that add stars mainly to their outskirts.

Early-type galaxies (ETGs) have been separated into two classes, based on their stellar kinematics: fast rotators and slow rotators (e.g. Emsellem et al. 2004, 2007; Cappellari et al. 2007; Emsellem et al. 2011). Cappellari (2016) suggested that these two classes also indicate two major channels of galaxy formation where fast-rotating ETGs start their life as star-forming disks and evolve through a set of processes dominated by gas accretion, bulge growth and quenching. In contrast, slow-rotating ETGs assemble near the centers of massive halos, via intense star formation at high redshift, and evolve from a set of processes dominated by gas-poor mergers. However, Naab et al. (2014) showed that the detailed formation history of a galaxy cannot be constrained from the slow-fast rotator classification alone, but when combined with the higher-order kinematic signatures, different merger scenarios can be distinguished.

In order to understand the evolutionary history of galaxies, we need a detailed analysis of its intrinsic structure. The Schwarschild orbit-superposition method (Schwarzschild 1979) is a powerful dynamical modelling technique that allows dynamical substructures in galaxies to be revealed. Several different implementations of the Schwarzschild method, with varying degrees of symmetry, have been described (Cretton et al. 1999; Gebhardt et al. 2003; Valluri et al. 2004; van den Bosch et al. 2008; Vasiliev & Athanassoula 2015; Vasiliev & Valluri 2020; Neureiter et al. 2021, e.g.). The Schwarschild method has been used to model supermassive black holes (van der Marel et al. 1998; Verolme et al. 2002; Gebhardt et al. 2003; Valluri et al. 2004; Krajnović et al. 2009; Rusli et al. 2013; Seth et al. 2014; Thater et al. 2017, 2019; Liepold et al. 2020; Quenneville et al. 2021a), the internal orbital structures of globular clusters (van de Ven et al. 2006; Feldmeier-Krause et al. 2017; Fahrion et al. 2019), early-type galaxies (Cappellari et al. 2006; Thomas et al. 2007; van de Ven et al. 2008; Thomas et al. 2014; Poci et al. 2019; Jin et al. 2020; den Brok et al. 2021) and recently expanded to galaxies of all morpholo-

gies (Vasiliev & Athanassoula 2015; Zhu et al. 2018b,c; Vasiliev & Valluri 2020; Lipka & Thomas 2021). The orbit distributions obtained by these models have also been used to identify different dynamical components in these stellar systems (e.g. van de Ven et al. 2006; Cappellari et al. 2007; van den Bosch et al. 2008; Lyubenova et al. 2013; Breddels & Helmi 2014; Krajnović et al. 2015). Zhu et al. (2018b) separated orbits into four different components: a cold component with near circular orbits (with strong rotation), a hot component with near radial orbits (characterized by random motions), a warm component in-between (characterized by weak rotation) and a counter-rotating component (similar to the warm and cold components). The inferred internal orbital distributions were then used to reconstruct the observed photometry and stellar kinematics of each component. However, the majority of these studies only had a few objects available (less than 30 galaxies). A large sample of galaxies, observed with good radial coverage and spatial resolution, is required in order to understand the average evolution history of the general galaxy population.

In the last two decades, Integral Field Spectroscopy (IFS) surveys such as SAURON (Spectroscopic Areal Unit for Research on Optical Nebulae; de Zeeuw et al. 2002), ATLAS^{3D} (Cappellari et al. 2011), CALIFA (Calar Alto Legacy Integral Field Array survey; Sánchez et al. 2012), SAMI (Sydney-Australian-Astronomical-Observatory Multi-object Integral-Field Spectrograph) Galaxy Survey (Croom et al. 2012; Bryant et al. 2015; Croom et al. 2021), MASSIVE (Ma et al. 2014), and MaNGA (Mapping Nearby Galaxies at Apache Point Observatory; Bundy et al. 2015) have provided us with rich observational datasets of galaxies, allowing their structure and evolution to be investigated in detail through the mapping of stellar kinematics across individual galaxies. These IFS surveys have made possible the use of techniques such as Schwarschild orbit-superposition method to dynamically decompose IFS observations to estimate the internal mass distribution, intrinsic stellar shapes and orbit distributions of galaxies across the Hubble sequence (e.g., Zhu et al. 2018a,b,c; Zhuang et al. 2019; Jin et al. 2020; Aquino-Ortíz et al. 2020).

Zhu et al. (2018c) studied a sample of 250 galaxies in the CALIFA survey, with total stellar masses between $10^{8.5}$ and $10^{12}M_\odot$, spanning all morphological types. About 95% of the galaxies in their sample had stellar kinematic maps with $R_{max} > 1R_e$, and $\sim 8\%$ with $R_{max} > 3R_e$. They found that, within 1 R_e, galaxies have more stars in warm orbits than in either cold or hot orbits. Similar results were also found in a sample

of 149 early-type galaxies in the MaNGA survey (Jin et al. 2020), with stellar masses ranging between $10^{9.9}$ and $10^{11.8} M_\odot$ and observations up to 1.5 - 2.5 R_e per galaxy. These studies also found that the changes of internal structures within $1R_e$ are correlated with the stellar mass of the galaxies.

The number of galaxies considered for Schwarzschild model studies to date has been limited and they have often not incorporated higher-order kinematic moments to further constrain the orbital models. Higher-order kinematic signatures are defined as the deviations from a Gaussian line-of-sight velocity distribution (LOSVD). When the LOSVD is parametrized as a Gauss–Hermite series (van der Marel & Franx 1993; Gerhard 1993), its skewness and excess kurtosis are parametrized by the coefficients of the 3rd- and 4th-order Hermite polynomials (h_3 and h_4, respectively). Given the connection between the higher-order stellar kinematic moments and a galaxy's assembly history (Naab et al. 2014), their inclusion in dynamical modelling can help distinguish between different formation scenarios.

In this paper we will apply Schwarzschild modelling to the SAMI Galaxy Survey (Croom et al. 2012; Bryant et al. 2015; Owers et al. 2017) to investigate the evolutionary histories of passive galaxies by studying their internal structures. The SAMI Galaxy Survey data allows us to study the internal orbits of a significant number of galaxies for the first time and allows us to further constrain the Schwarzschild models by adding information on the higher-order kinematic moments. Throughout the paper, we adopt a ΛCDM cosmology with $\Omega_m = 0.3$, $\Omega_\Lambda = 0.7$, and $H_0 = 70$ km s^{-1} Mpc^{-1}.

2. OBSERVATIONS

The Sydney-AAO Multi-object Integral field spectrograph (SAMI) Galaxy Survey is a large, optical Integral Field Spectroscopic (Croom et al. 2012; Bryant et al. 2015; Owers et al. 2017) survey of low-redshift ($0.04 < z < 0.095$) galaxies covering a broad range in stellar mass, $7 < \log_{10}(M_\star/M_\odot) < 12$, morphology and environment. The sample, with ≈ 3000 galaxies, is selected from the Galaxy and Mass Assembly survey (GAMA; Driver et al. 2011) regions (field and group galaxies), as well as eight additional clusters to probe higher-density environments (Owers et al. 2017).

The SAMI instrument (Croom et al. 2012), on the 3.9m Anglo-Australian telescope, consists of 13 "hexabundles" (Bland-Hawthorn et al. 2011; Bryant et al. 2014), across a 1-degree field of view. Each hexabundle consists of 61 individual 1.″6 fibres, and covers a $\sim 15''$ diameter region on the sky. In the typical configuration, 12 hexabundles are used to observe 12 science targets, with the 13th one allocated to a secondary standard star used for calibration. Moreover, SAMI also has 26 individual sky fibers, to enable accurate sky subtraction for all observations without the need to observe separate blank sky frames. The SAMI fibers are fed to the dual-beam AAOmega spectrograph (Sharp et al. 2006).

2.1. IFS Spectra and kinematic maps

SAMI data consist of 3D data cubes: two spatial dimensions and a third spectral dimension.

The wavelength coverage is from 3750 to 5750 Å in the blue arm, and from 6300 to 7400 Å in the red arm, with a spectral resolution of R = 1812 (2.65 Å full-width half maximum; FWHM) and R = 4263 (1.61 Å FWHM), respectively (van de Sande et al. 2017a), so that two data cubes are produced for each galaxy target.

Each galaxy field was observed in a set of approximately seven 30 minute exposures, that are aligned together by fitting the galaxy position within each hexabundle with a two-dimensional Gaussian and by fitting a simple empirical model describing the telescope offset and atmospheric refraction to the centroids. The exposures are then combined to produce a spectral cube with regular 0.5″ spaxels, with a median seeing of 2.1″. More details of the Data Release 3 reduction can be found in Croom et al. (2021)[1].

Stellar kinematic measurements were derived using the penalized pixel fitting code (pPXF; Cappellari & Emsellem 2004; Cappellari 2017), after combining the blue- and red-arm spectra by matching their spectral resolution. A detailed description of the method used to derive the stellar kinematic measurement can be found in van de Sande et al. (2017a,b). In particular, for our analysis, we use the Voronoi-binned kinematic measurements. Bins are adaptively generated to contain a target S/N of 10 Å^{-1}, using the Voronoi binning code of Cappellari & Copin (2003).

The available stellar kinematic measurements consist of 2D maps of stellar rotational velocity V, velocity dispersion σ, and the high kinematic orders (h_3 and h_4). In addition, each kinematic map has kinematic position angle and FWHM of the Point Spread Function (PSF - taken from a star observed at the same time as the galaxies) provided.

2.2. Multi Gaussian Expansion profiles and effective radius

Multi-Gaussian Expansion (MGE; Emsellem et al. 1994; Cappellari 2002) profile fits for the SAMI Galaxy

---

[1] Reduced data-cubes and stellar kinematic data products for all galaxies are available on: https://datacentral.org.au.

Survey are produced from the $r-$band photometry by D'Eugenio et al. (2021). The MGE method consists of a series expansion of galaxy images using 2D Gaussian functions. This method enables us to take the PSF into account; given a value of the inclination and assuming an intrinsic shape, the MGE model can be deprojected *analytically,* which is orders of magnitude faster than the general, integral-based method.

The fits are applied to re-analysed Sloan Digital Sky Survey (SDSS; York et al. 2000) images for GAMA galaxies, reprocessed as described in Hill et al. (2011), and VST/ATLAS (VLT Survey Telescope - ATLAS; Shanks et al. 2015) and SDSS DR9 (Ahn et al. 2012) observations for cluster galaxies, with VST/ATLAS data reprocessed as described in Owers et al. (2017). The images are square cutouts with $400''$ side, centred on the centre of the galaxy, and the MGE fits are calculated using MgeFit (Cappellari 2002) and the regularisation feature described in Scott et al. (2009). **For each fit, the position angle of the Gaussian components were required to be the same.** A more detailed description can be found in D'Eugenio et al. (2021). From the MGE best fit, we use the projected luminosity, size, and flattening of each Gaussian component to model the surface density of each galaxy and to deproject the stellar component to 3D density (the stellar mass distribution is assumed to be axisymmetric in projection, but can be intrinsically triaxial). The effective radius, R_e, used here is that of the major axis in the r-band. The semi-major axis values were taken from MGE fits.

2.3. *Stellar Mass*

Stellar masses are estimated assuming a Chabrier (2003) initial mass function (IMF), from the K-corrected $g-$ and the $i-$ magnitudes using an empirical proxy developed from GAMA photometry (Taylor et al. 2011; Bryant et al. 2015). For cluster galaxies, stellar masses are derived using the same approach (Owers et al. 2017). **We use the photometric stellar masses for our analysis in order to be consistent with previous SAMI studies and to have consistent comparisons with previous results in the literature (e.g. from CALIFA and MaNGA).**

2.4. *Sample Selection*

We use data from the final SAMI data release (described in the Data Release 3 publication Croom et al. 2021). This data release consists of 3068 unique galaxies. Of these, we have MGE profiles from D'Eugenio et al. (2021) for 2957 galaxies ($r-$band images are not available for some galaxies or they have been affected by a bright star in the field of view). **Following van de Sande et al. (2017a), we exclude all galaxies whose kinematics are influenced by mergers, that have strong bars or that have a bright object in their stellar velocity field.** This leaves us with 2834 galaxies with stellar kinematic and MGE measurements.

We exclude all galaxies with masses below $\log_{10}(M_\star/M_\odot) = 9.5$, because the incompleteness of the stellar kinematic sample is larger than 50% of the SAMI galaxy survey sample observed in this mass range. We further exclude 433 galaxies where $R_\mathrm{e} < 2''$ (due to their spatial size being smaller than the instrumental spatial resolution). This leaves us with 1649 galaxies.

Following the recommendations of van de Sande et al. (2017a), for each galaxy we select spaxels that meet the following quality criteria:

Q_1) $S/N > 3$ Å^{-1} & $\sigma_{obs} > 35$ km/s;

Q_2) $V_{ERR} < 30$ km/s & $\sigma_{ERR} < \sigma_{obs} \times 0.1 + 25$ km/s.

Q_3 in van de Sande et al. (2017a) is for measurements with $S/N < 20$ Å^{-1} and $\sigma_{obs} < 70$ km/s. We cautiously include these in this analysis and increase the errors on the measurements that do not meet this criterion to down-weight their contributions. The 1589 galaxies that meet these criteria are shown in Fig. 1.

In this paper we focus on passive galaxies, because the long-term goal of this project is to study the effects of galaxy environment on passive galaxies (Santucci et al. in prep). We use the SAMI spectroscopic classification presented in Owers et al. (2019) to select a homogeneous sample. The SAMI spectroscopic classification labelled galaxies as star-forming, passive, or Hδ-strong, using the absorption- and emission-line properties of each SAMI spectrum. We select 738 passive galaxies.

2.4.1. *Radial coverage and spatial sampling selection*

We compare the spatial resolution and radial extent of our sample to the sample from (Zhu et al. 2018b) who used CALIFA data to derive orbital parameters using the Schwarzschild method. SAMI Voronoi bins are generated to contain a target S/N of 10 Å^{-1}. Since the target S/N is the only requirement for the bins, individual spaxels of $0.5''$ are left unbinned when they meet this requirement. For these single-spaxel bins, the covariance is larger (since they are smaller than the SAMI spatial resolution). In Fig. 1 we show the number of Voronoi bins within $1R_\mathrm{e}$ versus the radial coverage avalable (in units of R_e) for the 1589 SAMI galaxies (in grey) that meet our quality criteria. CALIFA galaxies (in purple; from Zhu et al. 2018b) have a similar distribution in number of bins to SAMI, however their bins were generated with different criteria (their minimum $S/N = 20$
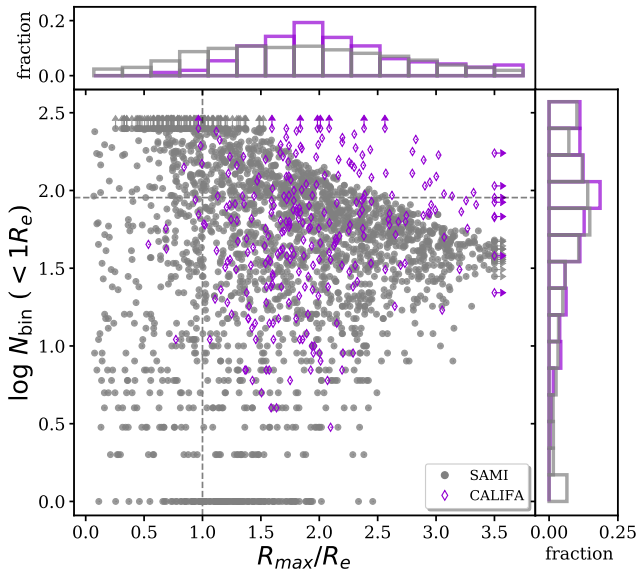
Figure 1. Number of Voronoi bins within $1R_e$ that meet our quality criteria versus the maximum radius available for stellar kinematics (in units of R_e) for the galaxies in the SAMI Galaxy Survey (1589 galaxies; grey circles) and in the CALIFA survey (259 galaxies; violet diamonds). Black dashed lines indicate $R_{max}/R_e = 1$ and Voronoi bins = 85. We calculate the marginalised fractions of galaxies to the total number in each sample, by mass and size, and show them in the top and left panels of the figure. Grey lines are for SAMI galaxies, while the violet lines are for CALIFA galaxies. The CALIFA and the SAMI samples have similar distributions in Voronoi bins and radial coverage, although there are more CALIFA galaxies with measurements up to $2R_e$. For this analysis we select galaxies in the top right corner ($R_{max} > 1R_e$ and Voronoi bins > 85).

and their spaxel size is consistent with their spatial resolution), therefore a direct comparison is not possible. CALIFA and SAMI also show a similar distribution in radial coverage, although there are more CALIFA galaxies with measurements up to $2R_e$.

In this analysis, the first in a series, we select a high-quality subsample of SAMI galaxies, identified by good spatial resolution and good radial coverage (top right corner of Fig. 1). This region is selected as the optimal compromise between best quality data and reasonable sample size, and corresponds to galaxies with 85 Voronoi bins within $1R_e$ and $R_{max} > R_e$. More details about the radial coverage tests we performed can be found in Appendix A.

This quality cut gives us a sample of 179 passive galaxies. We visually inspect the galaxies in this sample using HSC images and exclude the face-on strongly

barred galaxies that were not identified as barred from the square cutouts used for the MGE modelling. This cut gives us a final sample of 161 galaxies. These are shown in Fig. 2 and used hereafter in this analysis. The majority of the galaxies in our sample are early-type galaxies ($\sim 85\%$), $\sim 11\%$ are S0/Early-spirals and $\sim 4\%$ are late-type galaxies (visual morphological classification from Cortese et al. 2016). We note that our final sample is biased toward galaxies that are more massive and larger than the general SAMI passive population. This bias is caused by selecting galaxies with at least 85 Voronoi bins within $1 R_e$.
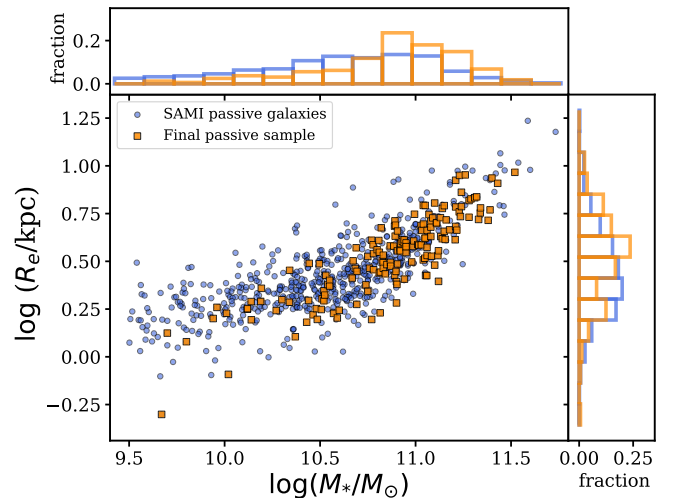
Figure 2. Effective radius, R_e, versus stellar mass. Blue circles are the passive galaxies in the SAMI sample with $\log_{10}(M_\star/M_\odot) > 9.5$ and $R_e > 2''$ (738), orange squares are the galaxies included in the final sample (161). We calculate the marginalised fractions of galaxies with respect to the total number in each sample, by mass and size, and show them in the top and left panels of the figure. Blue lines are for the passive galaxies in the SAMI Galaxy Survey, while the orange lines are for our final sample. The two samples are slightly different in the marginalized mass and size distributions, so that we have higher fractions of massive and large galaxies in the final sample compared to the initial sample. This is due to selecting galaxies with more than 85 Voronoi bins.

3. SCHWARZSCHILD ORBIT-SUPERPOSITION TECHNIQUE

3.1. *Schwarzschild's models and free parameters*

We use the Schwarzschild orbit-superposition technique (Schwarzschild 1979) to model our individual galaxies, using the implementation from van den Bosch et al. (2008), **with the correct orbital mirroring (Quenneville et al. 2021b)**, that allows us to model

triaxial stellar components [2], while most of the results in the literature assume axisymmetry. There are three main steps required to create a Schwarzschild model:

1. Construct a model for the underlying gravitational potential;

2. Calculate a representative library of orbits using the gravitational potential previously modelled;

3. Find a combination of orbits that can reproduce the observed kinematic maps and luminosity distribution.

These steps are fully described in van den Bosch et al. (2008) and Zhu et al. (2018a) and are summarized in the following subsections.

3.2. *Gravitational Potential*

The model gravitational potential of each galaxy is generated using the combination of three components: a stellar and a dark matter distribution and a central super-massive black hole. The triaxial stellar component mass is calculated from the best-fit two-dimensional MGE luminosity density (from D'Eugenio et al. 2021) which is de-projected assuming the orientation in space of the galaxy, described by three viewing angles (θ, ϕ, ψ), to obtain a three-dimensional luminosity density. The space orientation (θ, ϕ, ψ) can be converted directly to the intrinsic shape (p_i, q_i, u_i), where $p_i = B_i/A_i$, $q_i = C_i/A_i$ and $u_i = \sigma_{Gauss,i}^{obs}/\sigma_{Gauss,i}$. A_i, B_i, C_i represent the major, medium and minor axes of the 3D triaxial Gaussian component and $\sigma_{Gauss,i}$ represents the size of each Gaussian component. Moreover, the flattest Gaussian component, having the minimum flattening q_{min}, dictates the allowed space orientation for the de-projection, so that we can take (p_{min}, q_{min}, u_{min}) as our free parameters. This 3D density is then converted into a stellar mass distribution using a radially constant stellar mass-to-light ratio $M_\star/L$ (note that $M_\star/L$ is a free parameter in our modelling). The corresponding stellar gravitational potential $\Phi_\star$ is calculated using the classical formula from Chandrasekhar (1969).

The dark matter halo distribution is assumed to follow a spherical Navarro-Frenk-White profile (NFW; Navarro et al. 1996). The mass, M_{200} (mass enclosed within a radius, R_{200}, where the average density is 200 times the critical density), in a NFW dark matter halo is determined by two parameters. These are the concentration parameter, c, and the fraction of dark matter within R_{200}, $f = M_{200}/M_\star$ (where M_{200} is as defined above and $M_\star$ is the total stellar mass).

The spatial resolution of SAMI data is poorer than the influence radius of the black hole, so its mass leaves no imprint on the stellar kinematic maps and therefore does not affect our results. We therefore fix the black hole mass to the value derived from the stellar velocity dispersion, measured within an aperture of $1R_e$, assuming the relation between black hole mass and the stellar velocity dispersion of a galaxy from McConnell et al. (2011).

Combining the components used to describe the gravitational potential, we have six free parameters (stellar mass-to-light ratio, $M_\star/L$, the intrinsic shape of the flattest Gaussian component (p_{min}, q_{min}, u_{min}), the dark matter halo concentration, c, and dark matter fraction, f) that must be determined. To determine these best-fit parameters for each galaxy, we run an optimised grid-based parameter search as described in Zhu et al. (2018a) and summarized in Sec. 3.4.

3.3. *Orbit library*

To fit a model to our observed data we need an orbit library. To create the orbit library we use a separable triaxial potential, where all orbits are regular and conserve three integrals of motion (energy E, second integral I_2 and third integral I_3) which can be calculated analytically. Four different types of orbits exist: three types of tube orbits (short axis tubes, outer and inner long axis tubes) and box orbits. We create initial conditions for our orbits by sampling from the three integrals of motion. We refer to van den Bosch et al. (2008) for the details of the orbit sampling.

The number of points we sample across the three integrals is $n_E \times n_\theta \times n_R = 21 \times 10 \times 7$, where n_E, n_θ, n_R are the number of intervals taken across the energy E, the azimuthal angle θ and radius R on the (x, z) plane. However, this orbit library includes mostly short axis tubes, long axis tubes and a relatively low fraction of box orbits in the inner region. Since box orbits are essential for creating triaxial shapes, we construct an additional set of box orbits. Box orbits always touch equipotentials (Schwarzschild 1979), so they can be described by combining the energy E with two spherical angles (θ and ϕ). The number of points included in the box orbit set are $n_E \times n_\theta \times n_\phi = 21 \times 10 \times 7$.

We add an additional set of orbits to account for retrograde stars commonly found in early-type galaxies (Bender 1988; Kuijken et al. 1996). This set contains

---

[2] A new implementation of this code, DYNAMITE (DYnamics, Age and Metallicity Indicators Tracing Evolution), has recently been released (Jethwa et al. 2020). This was not available at the beginning of this analysis. Internal tests have been carried out which have verified the consistency between the two implementations.

21 × 10 × 7 orbits to describe the initial conditions for counter-rotating orbits. To summarize, we use three sets of 21 × 10 × 7 orbits: a typical set of (E, I_2, I_3), a box orbits set of (E, θ, ϕ) and a counter-rotating set of also $(E, -I_2, I_3)$.

As in van den Bosch et al. (2008) and Zhu et al. (2018b), we dither every orbit to give 5^3 orbits by perturbing the initial conditions slightly, in order to smooth the model. The orbit trajectories created will be co-added to form a single orbit bundle in our orbit library.

We then use Schwarzschild's method to weight the various orbit contributions to the velocity distribution profile in each bin to construct a model with observational parameters that can be fit to the data (the description of how kinematic maps are fitted can be found in Zhu et al. 2018a). The quantities that will be compared to observations are spatially convolved with the same PSF as the observations. The model and the observed values are then divided by the observational error so that a χ^2 comparison is achieved. The weights are determined by the van den Bosch et al. (2008) implementation, using the Lawson & Hanson (1974) non-negative least squares (NNLS) implementation.

3.4. Best-fit model

In order to find the best-fit model, which contains six free parameters, we run a grid based parameter search. We use a parameter grid with intervals of 0.5, 0.1, 0.2, 0.05, 0.05 and 0.01 in $M_\star/L$, $\log(c)$, $\log(f)$, q_{min}, p_{min} and u_{min}, respectively, and perform an iterative search for the best-fitting models. After each iteration, the best-fit model is selected by using a χ^2 comparison. The best-fit model is defined as the model with minimum kinematic χ^2:

$$\chi^2 = \sum_{n=1}^{N_{kin}} \left[\left(\frac{V_{mod}^n - V_{obs}^n}{V_{obserr}^n} \right)^2 + \left(\frac{\sigma_{mod}^n - \sigma_{obs}^n}{\sigma_{obserr}^n} \right)^2 + \left(\frac{h_{3,\ mod}^n - h_{3,\ obs}^n}{h_{3,\ obserr}^n} \right)^2 + \left(\frac{h_{4,\ mod}^n - h_{4,\ obs}^n}{h_{4,\ obserr}^n} \right)^2 \right] \quad (1)$$

where V_{mod}^n, σ_{mod}^n, $h_{3,\ mod}^n$ and $h_{4,\ mod}^n$ are the model values for each bin n, V_{obs}^n, σ_{obs}^n, $h_{3,\ obs}^n$ and $h_{4,\ obs}^n$ are the observed values in each bin and V_{obserr}^n, σ_{obserr}^n, $h_{3,\ obserr}^n$ and $h_{4,\ obserr}^n$ represent the observational errors. N_{kin} is the number of bins in the kinematic maps. We define a confidence level around that minimum value and select all the models whose χ^2 is within that confidence level: $\chi^2 - \chi_{min}^2 < \chi_s^2 \times \sqrt{(N_{obs} - N_{par})}$, with $\chi_s^2 = 2$, $N_{obs} = 4N_{kin}$, as we use V, σ, h_3 and h_4 as model constraints, and N_{par} is the number of free parameters (6 here). We then create new models around

the existing models with lower kinematic χ^2 values by walking two steps in every direction of the parameter grid from each of the selected models. In this way, the searching process goes in the direction of smaller χ^2 on the parameter grid, and it stops when the minimum χ^2 model is found. Next, we continue the iteration by using a larger value of χ_s^2, to ensure all the models within 1σ confidence are calculated before the iteration finishes. The values of χ_s^2 are chosen empirically so that it is neither too small (finding only local minimums) nor too large. For the final step, we reduce the parameter intervals by half to get a better estimate of the best-fit parameters. The models whose χ^2 are within the confidence level are included for calculating the statistical uncertainties of the model parameters for single data analysis. The maximum and minimum values of the parameters or properties in these models are treated as upper and lower limits in 1σ error regions.

The kinematic maps for the best-fit models of example galaxies 9403800123, **9019900793, 220465 and 9008500323 are presented in Fig. 3, Fig. 4, Fig. 5 and Fig. 6. We selected these four galaxies as representative of the sample, with 9403800123 being a non edge-on oblate galaxy (with 255 Voronoi bins within $1R_e$), 9011900793 an edge-on oblate galaxy (with 87 Voronoi bins within $1R_e$), 220465 a triaxial galaxy (142 Voronoi bins within $1R_e$) and 9008500323 a prolate galaxy (with 104 Voronoi bins within $1R_e$). Even when the spatial sampling is low, as in the case of 9011900793, the model is able to reproduce the best-fit maps well ($\chi_{red}^2 = 2.22$ for galaxy 9403800123, $\chi_{red}^2 = 1.72$ for galaxy 9011900793, $\chi_{red}^2 = 1.79$ for galaxy 220465 and $\chi_{red}^2 = 1.99$ for galaxy 9008500323[3]).** We also show the explored parameter grids and the obtained internal mass distribution, orbit circularity, triaxiality and tangential anisotropy for the best fits of these four galaxies in Appendix B. These parameters are fully described in the following section.

4. RESULTS

In this section and the next we present the results we obtain modelling a sample of 161 passive galaxies in the SAMI Galaxy Survey with the Schwarzschild orbit-superposition technique. **For each galaxy we explore**

---

[3] The reduced χ^2 is defined as $\chi_{red}^2 = \frac{\chi^2}{4N_{kin}-N_{par}}$, with χ^2 calculated following Eq. 1. **The values of χ_{red}^2 are not always equal to 1 for the best-fit models of the galaxies in our sample. This is because the input kinematic maps of the galaxies in our sample were not symmetrised. Therefore, comparing the observed maps to the model maps, which are symmetric, can result in values of χ_{red}^2 higher than 1.**
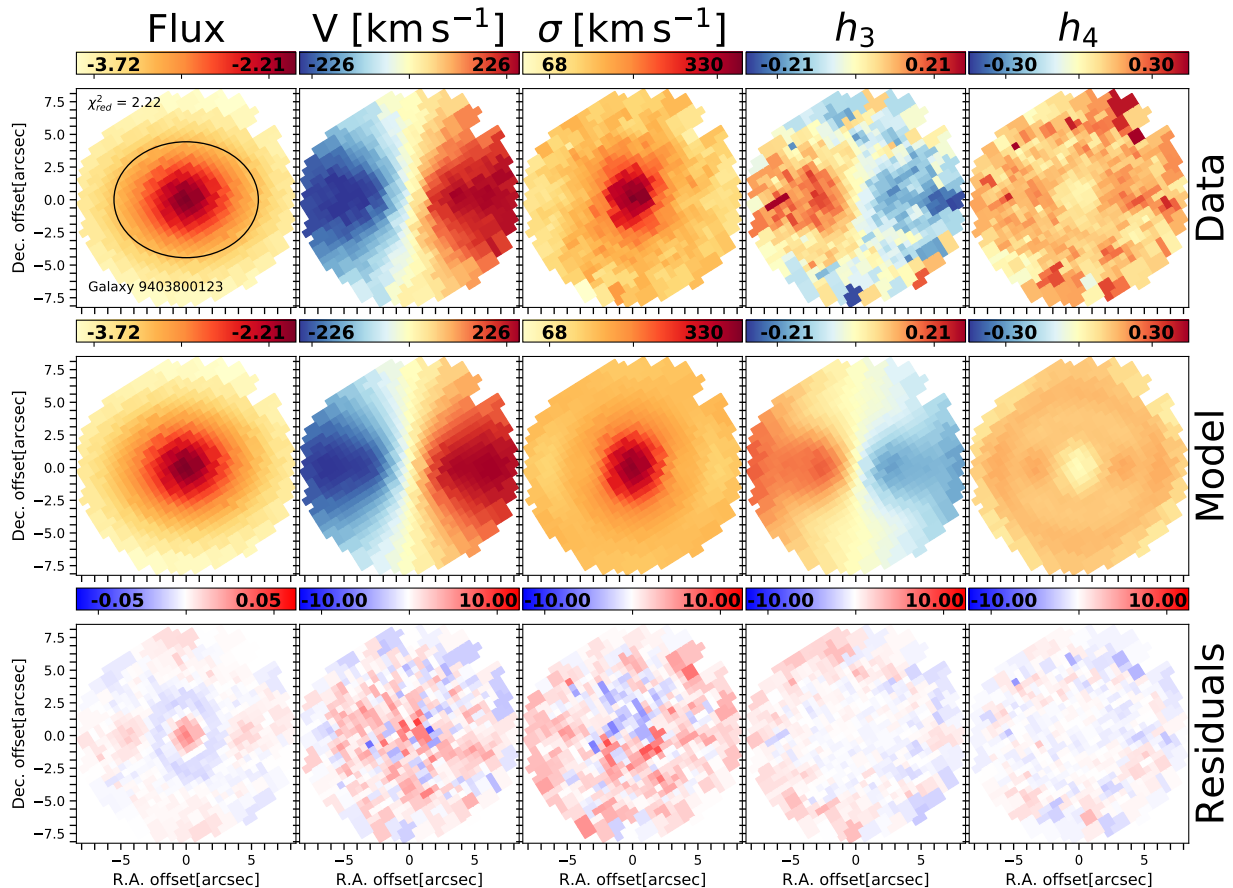
Figure 3. Example of a galaxy with excellent spatial sampling: SAMI CATID 9403800123 in the cluster Abell 4038. This galaxy ($\log M_\star/M_\odot = 11.05$ and $R_e = 5.52''$) is a non edge-on oblate galaxy and has stellar kinematic measurements up to 1.36 R_e and counts 255 spatial bins within $1R_e$ (black ellipse). Columns show 2D maps for, from left to right, flux, velocity, velocity dispersion, h_3 and h_4. First row shows the observed maps, second row shows the best-fit maps derived from the Schwarzschild modelling and the third row shows the residuals, calculated as the difference between the observation and the model, divided by the observational uncertainties. The best-fit model maps ($\chi^2_{red} = 2.22$) accurately reconstruct the structures seen in the observations, not only for the velocity and velocity dispersion maps, but also for h_3 and h_4.

a range in parameter space by building on average 1250 different models. By comparing the 2D maps of the flux and kinematic parameters derived from each model and observations we determine the best-fit parameters. From the best-fit model we derive the intrinsic properties of the inner mass distribution (for both stellar and dark matter), intrinsic stellar shape (axis ratios and ellipticity), velocity anisotropy and the orbit circularity distribution. We take as our best-fit values the parameters calculated at or averaged within an aperture of $1R_e$, depending on the parameter. Uncertainties on the measured values are calculated using Monte Carlo realisations, as described in Appendix C, combined with the 1σ confidence levels for the parameters fluctuations from the best-fit model that we describe in Sec. 3.4.

4.1. *Inner mass distribution*

The total mass (M_{tot}) radial distribution is one of the fundamental parameters of the Schwarzschild model,

which includes a stellar component and a dark matter component (M_{dark}). A black hole mass component is included as well, but not discussed here as its contribution to the total mass distribution is negligible. The distribution of the fraction of dark matter $(f_{DM} = M_{dark}/M_{tot})$ within $1R_e$ for the galaxies in our sample is shown in Fig. 7. The average value of the dark matter fraction is 0.28, with a standard deviation of 0.20. Similar to Cappellari et al. (2013), we fit a quadratic function to the f_{DM} versus stellar mass distribution. The best-fit relation follows $f_{DM} \sim 0.10 + 0.17 \times (\log M_\star/M_\odot - 10.59)^2$, although the 1-$\sigma$ scatter along this relation is as high as $\delta f_{DM} = 0.24$.

Above a stellar mass of $\log(M_\star/M_\odot) \sim 10.75$ we see a hint of an increasing f_{DM} as a function of stellar mass. To test whether this trend is statistically significant, we use the Kendall's correlation coefficient τ, using the Python package *scipy.stats.kendalltau* (Virta-
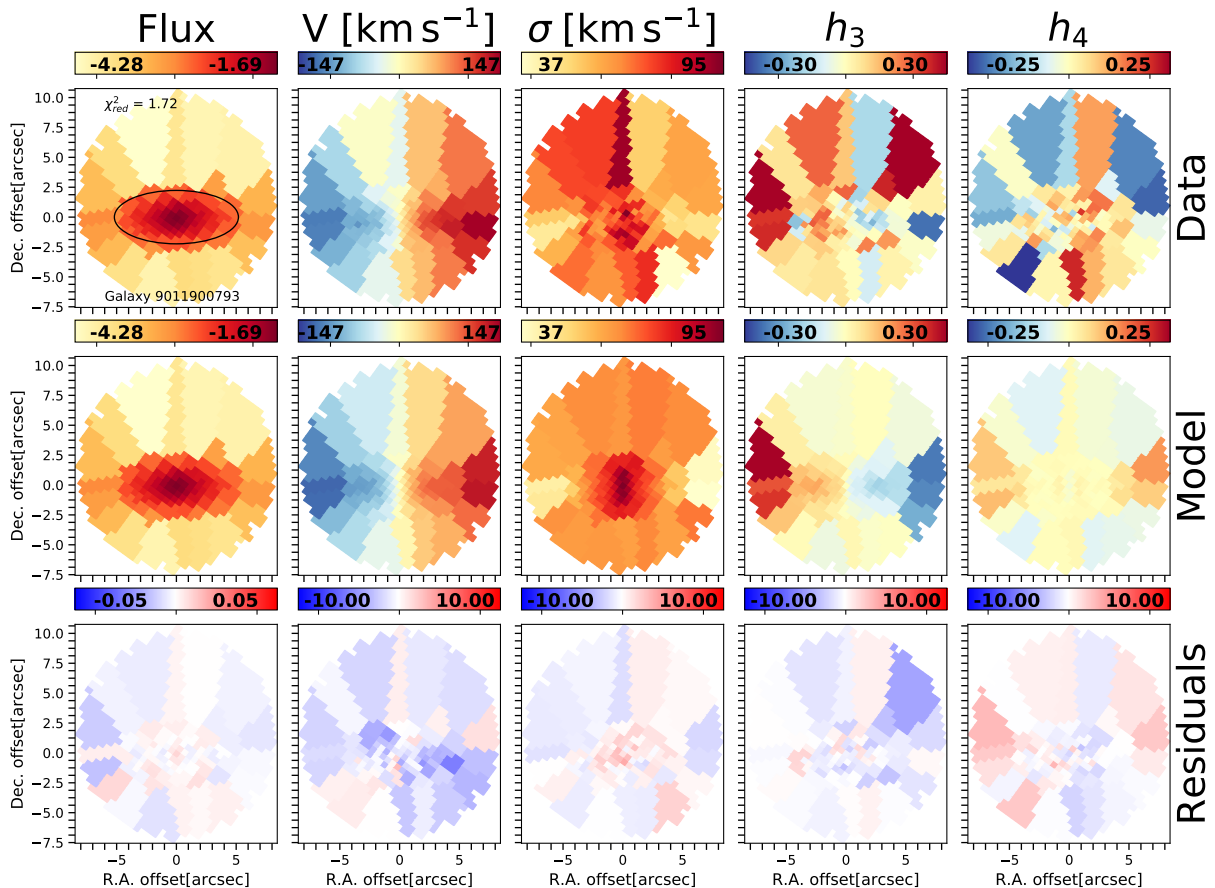
Figure 4. Example of a galaxy near the minimum requirement of 85 spatial bins: SAMI CATID 9091100793 in the cluster Abell 911. This galaxy ($\log M_\star/M_\odot = 10.34$ and $R_e = 5.19''$) is a edge-on oblate galaxy and has stellar kinematic measurements up to 1.45 R_e and 87 spatial bins within $1R_e$. Panels are as in Fig. 3. The best-fit model maps ($\chi^2_{red} = 1.72$) accurately reconstruct the structures seen in the observations.

nen et al. 2019). This correlation coefficient is robust to small sample sizes. A τ value close to 1 indicates strong correlation, whereas a value close to -1 indicates strong anti-correlation. For galaxies with $\log(M_\star/M_\odot) \gtrsim 10.75$ we find a value of $\tau = 0.17$, **with a probability of correlation of 99.73%.** While the trend of increasing fraction of dark matter with increasing stellar mass is mild, it is significant at the 3-σ level.

4.2. *Intrinsic stellar shape*

Next, we investigate the intrinsic shapes of the galaxies in our sample. As shown in Sec. 3.2, three parameters are used to model the dynamically-based intrinsic stellar shape of each galaxy: p, q and u. The intrinsic shape has been shown to be connected to various other galaxy properties such as: stellar mass (Sánchez-Janssen et al. 2010), luminosity (Sánchez-Janssen et al. 2016), spin parameter (e.g. Foster et al. 2017), mean stellar population age (van de Sande et al. 2018) and its environment (Fasano et al. 2010; Rodríguez et al. 2016). Furthermore, theoretical simulations suggest that intrin-

sic shape depends on a galaxy's formation history (Jesseit et al. 2009; Li et al. 2018b,a).

Here, in particular, we analyse the triaxial parameter T_{Re}, calculated at $1R_e$ and defined as:

$$T_{Re} = (1 - p^2_{Re})/(1 - q^2_{Re}). \qquad (2)$$

We show an example of the best-fit intrinsic shape parameters p, q and T as a function of radius in Appendix B, Fig. 30. Based on the triaxiallity parameter T_{Re}, we separate galaxies into three groups according to their dynamically-based intrisic shape: oblate ($T_{Re} = 0$), **prolate** ($T_{Re} = 1$) **and triaxial** ($T_{Re} \neq 0, 1$). In Fig. 8 we show the triaxial parameter T_{Re} as a function of stellar mass $\log(M_\star/M_\odot)$. **The majority of the galaxies in our sample are close to oblate (118 out of 161 galaxies; $73\% \pm 3\%$), 30 galaxies ($19\% \pm 3\%$) show evidence of being mildly triaxial ($0.1 < T_{Re} \leq 0.3$) and 13 galaxies ($8\% \pm 3\%$) have triaxial/prolate shapes (with $T_{Re} > 0.3$). There is evidence of a slight increase of triaxiality with increasing stellar mass ($\tau = 0.1$), however, this**
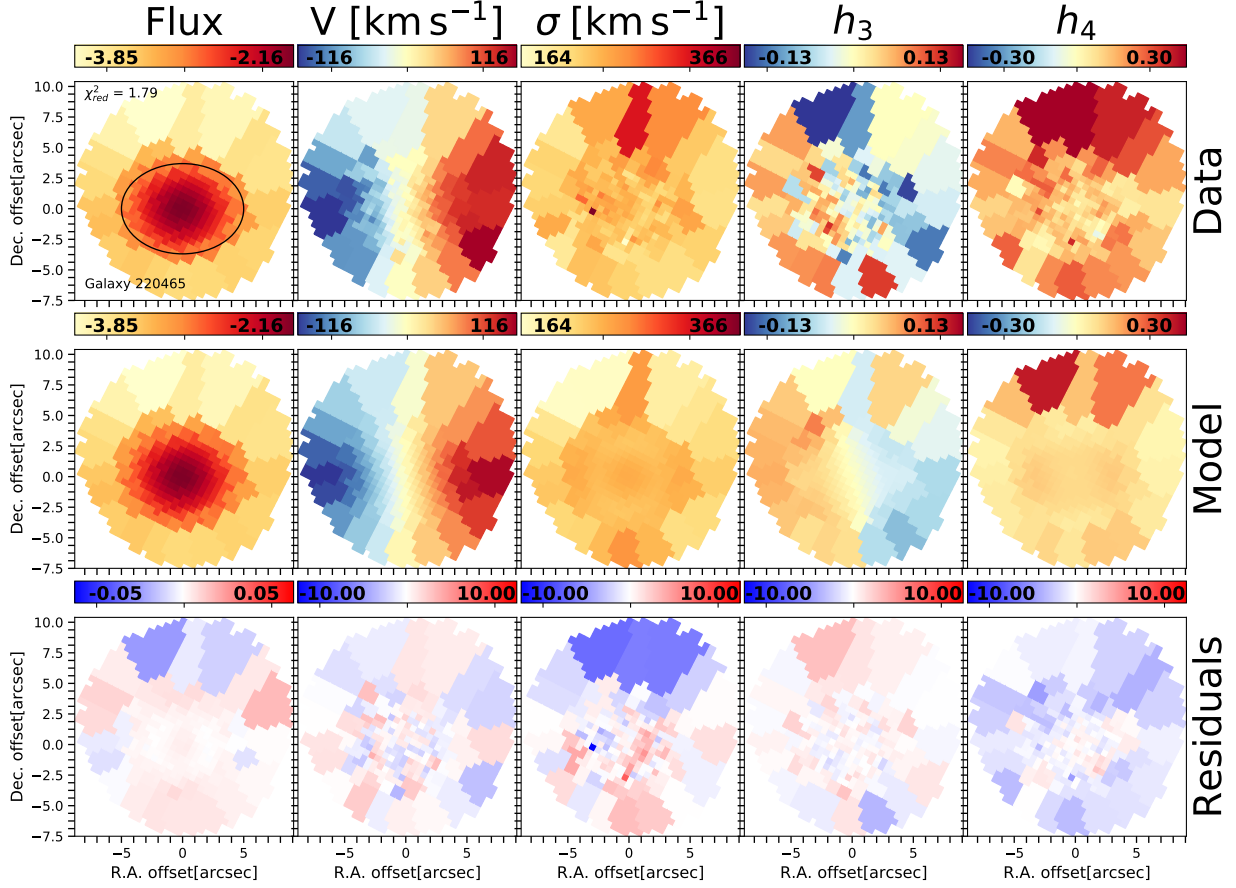
Figure 5. Example galaxy SAMI CATID 220465, in the GAMA region. This galaxy ($\log M_\star/M_\odot = 11.31$ **and** $R_{\rm e} = 5.00''$) **is a triaxial galaxy and has stellar kinematic measurements up to 1.5 $R_{\rm e}$ and 142 spatial bins within** $1R_{\rm e}$. **Panels are as in Fig. 3. The best-fit model maps** ($\chi^2_{red} = 1.79$) **accurately reconstruct the structures seen in the observations, not only for the velocity and velocity dispersion maps, but also for h_3 and h_4.**

trend is only significant at a 1-σ level (with a probability of 82.96%). However, if we consider the fraction of galaxies that have $T_{Re} > 0.1$ (non-oblate galaxies), we find a clear increase of the fraction with stellar mass, with a sharp change at $\sim 10^{10.50} M_\star/M_\odot$, with the fraction of non-oblate galaxies increasing from $12\% \pm 4\%$ to $29\% \pm 2\%$ at this mass.

Non-oblate galaxies must be dispersion-supported, with their shape reflecting the anisotropic velocity dispersion. In contrast, oblate galaxies may have varying degrees of rotation support and anisotropy (e.g. Kireeva & Kondratyev 2019). We analyse the distribution of the velocity dispersion anisotropy in the next section.

4.3. *Velocity anisotropy*

Velocity dispersion anisotropy parameters (e.g. β_r, β_z) are widely used as indicators of the underlying orbit distribution of a galaxy. However, various definitions and approaches exist in the literature. The velocity dispersion anisotropy parameter used in more recent

literature, β_z, is in cylindrical coordinates and has been used in particular to describe the global anisotropy in fast-rotating axisymmetric galaxies (Cappellari et al. 2007). This parameter measures the velocity anisotropy along the radius on the disk plane, in cylindrical coordinates, following the idea of cylindrically aligned ellipsoids in oblate galaxies. However, for triaxial galaxies β_z ($< R_{\rm e}$) will have a contribution from both circular orbits (which have cylindrically-aligned velocity dispersion ellipsoids) as well as radial and box orbits (which have spherically-aligned velocity dispersion ellipsoids). Recent results (Thater et al. 2021) show that the velocity dispersion ellipsoids for the elliptical galaxy NGC 6958 are more closely aligned with spherical coordinates. The misalignment between the measured ellipsoids and the cylindrical coordinates can reach angles as high as 80°. This misalignment can even occur in disk galaxies, most notably, our own Milky Way (Büdenbender et al. 2015; Hagen et al. 2019). Following Thater et al. (2021), we measure the misalignment of the velocity ellipsoids for the galaxies in our sample and find that they are
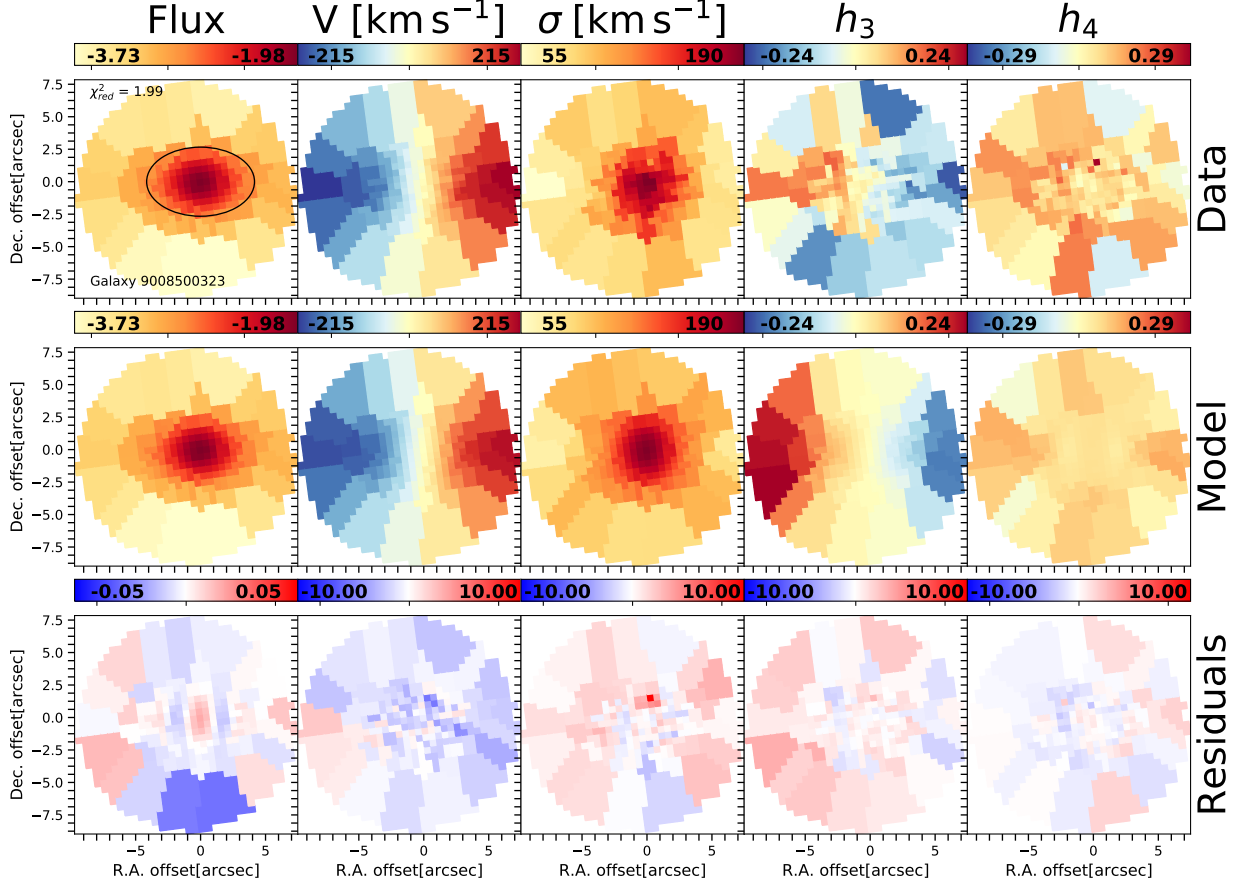
Figure 6. Example galaxy SAMI CATID 9008500323, in the cluster Abell 85. This galaxy ($\log M_\star/M_\odot = 10.78$ and $R_{\rm e} = 4.15''$) is a prolate galaxy and has stellar kinematic measurements up to 1.81 $R_{\rm e}$ and 104 spatial bins within $1R_{\rm e}$. Panels are as in Fig. 3. The best-fit model maps ($\chi^2_{red} = 1.99$) accurately reconstruct the structures seen in the observations, not only for the velocity and velocity dispersion maps, but also for h_3 and h_4.

more closely aligned with spherical coordinates. For this reason, we focus on the radial velocity anisotropy parameter, β_r, in the results presented here. For completeness, we also include the results for β_z in Appendix D.

We define the velocity anisotropy parameter β_r, in spherical coordinates, following Binney & Tremaine (2008):

$$\beta_r = 1 - \frac{\Pi_{tt}}{\Pi_{rr}}, \tag{3}$$

with

$$\Pi_{tt} = \frac{\Pi_{\theta\theta} + \Pi_{\phi\phi}}{2}, \tag{4}$$

(r, θ, ϕ) the standard spherical coordinates, and

$$\Pi_{kk} = \int \rho \sigma_k^2 \, d^3x = \sum_{n=1}^{N} M_n \sigma_{k,n}^2 \tag{5}$$

with σ_k the velocity dispersion along the direction k at a given location inside the galaxy. The summation defines how we computed this quantity from our Schwarzschild models. M_n is the mass contained in each of the N polar bins in the meridional plane of the model, and $\sigma_{k,n}$ is the corresponding mean velocity dispersion along the direction k.

We calculate the value of β_r within $1R_{\rm e}$, excluding the inner regions ($r < 2''$) since this region is affected by atmospheric seeing. $\beta_r > 0$ indicates radial anisotropy, $\beta_r < 0$ indicates tangential anisotropy and $\beta_r = 0$ indicates isotropy. Figure 9 shows the derived values of β_r, for each galaxy, as a function of intrinsic ellipticity. Here, we derive ε using the intrinsic flattening, q_{Re}, from the best-fit model of the galaxy, measured at $1R_{\rm e}$; $\varepsilon_{intr} = 1 - q_{Re}$. In general, galaxies with high ellipticity (flat galaxies, $\varepsilon_{intr} > 0.7$) are close to isotropic or tangentially anisotropic (supported by rotation). We also find that radially anisotropic galaxies are typically more massive than tangentially anisotropic galaxies.

4.4. *Spin Parameter*

The proxy for the spin parameter, λ_r, has previously been used to separate slow-rotating galaxies from fast-rotating galaxies (Emsellem et al. 2007, 2011; Cappellari
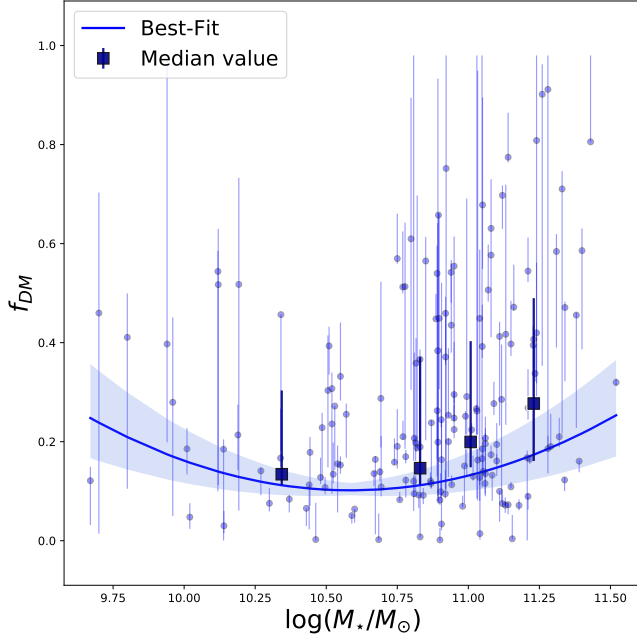
Figure 7. Fraction of dark matter to total mass ($f_{\mathrm{DM}} = M_{dark}/M_{tot}$) within $1R_e$ as a function of stellar mass. The median values of the fraction of dark matter for each of the 4 mass bins are shown as dark blue squares, with the error bars marking the 25th and 75th percentiles. The blue solid line is the parabolic best-fit to the data - $f_{\mathrm{DM}} \sim 0.10 + 0.17 \times (\log \frac{M_\star}{M_\odot} - 10.59)^2$. The shaded region represents the error on the best-fit.

2016). We use the Cortese et al. (2016) definition of the spin parameter to calculate λ_r for each galaxy:

$$\lambda_r = \frac{\sum_{i=0}^{N_{spx}} F_i R_i |V_i|}{\sum_{i=0}^{N_{spx}} F_i R_i \sqrt{V_i^2 + \sigma_i^2}} \qquad (6)$$

where i refers to each spaxel within the ellipse with semi-major axis R_e and ellipticity ε, F_i is the corresponding flux of the ith spaxel, V_i is its stellar velocity, σ_i is the velocity dispersion and R_i is the semi-major axis of the ellipse in which the spaxel lies. Since λ_r is calculated within $1R_e$, it will be referred to as λ_{Re} hereafter.

For completeness, we also measure the ratio of ordered to random motion V/σ, also measured within $1R_e$, using the definition from Cappellari et al. (2007):

$$\left(\frac{V}{\sigma}\right)^2 \equiv \frac{\langle V^2 \rangle}{\langle \sigma^2 \rangle} = \frac{\sum_{i=0}^{N_{spx}} F_i V_i^2}{\sum_{i=0}^{N_{spx}} F_i \sigma_i^2}. \qquad (7)$$

Results obtained using V/σ are similar to those obtained for λ_{Re} and are shown in Appendix E.

Inclination has a strong impact on the observed λ_{Re} and V/σ quantities, in particular when the viewing angle is close to face-on (e.g. Binney et al. 1990). While inclination corrections are now commonly applied to λ_{Re}
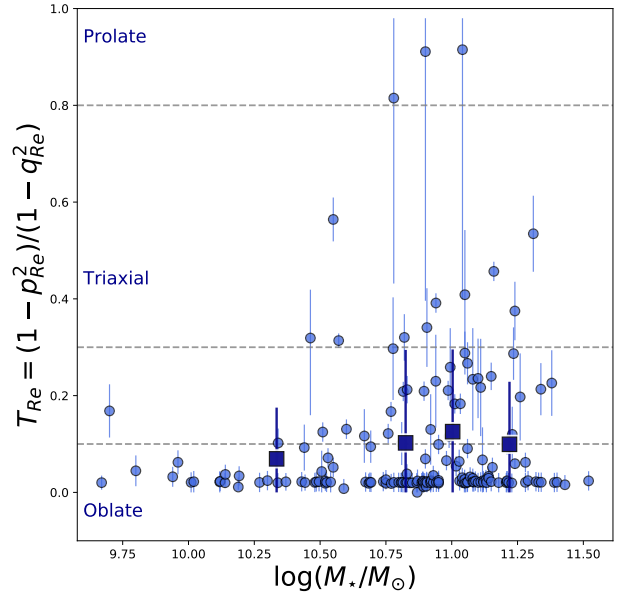
Figure 8. Triaxial parameter $T_{Re} = (1 - p_{Re}^2)/(1 - q_{Re}^2)$ as a function of stellar mass. **Galaxies with $T_{Re} = 0$ are classified as oblate, galaxies with $T_{Re} = 1$ as prolate and those in-between as triaxial. Grey dashed lines represent $T_{Re} = 0.1$, $T_{Re} = 0.3$ and $T_{Re} = 0.8$.** The majority of the galaxies in our sample are oblate, with a few galaxies with non-oblate shape. **The average values of the triaxiality parameter for each of the 4 mass bins are shown as dark blue squares, with the error bars marking the 1-σ scatter. There is a weak increase in the triaxiality parameter with increasing stellar mass. The percentage of galaxies that are non-oblate ($T_{Re} > 0.1$) increases with increasing stellar mass, going from $12\% \pm 4\%$ below $10^{10.50} M_\star/M_\odot$ to $29\% \pm 2\%$ above this mass.**

measurements (e.g. Querejeta et al. 2015; van de Sande et al. 2018; Falcón-Barroso et al. 2019; del Moral-Castro et al. 2020; Fraser-McKelvie et al. 2021) these methods cannot be applied for slow rotating or trixial galaxies (for a detailed discussion see van de Sande et al. 2021a). Our trixial Schwarzschild models now allow us, irrespective of galaxy type, to deproject each galaxy to a consistent edge-on view and reconstruct a best-fit internal orbital distribution for that viewing angle.

In order to reconstruct the edge-on maps, we recalculate and store the orbit library for each galaxy, with a specific projection. Schwarzschild models take into account the PSF of the observations when reproducing the kinematics. To construct 2D maps without the impact of seeing within the Schwarzschild routine, we set the PSF FWHM to 0.01″ for the model to use when projecting the galaxy.
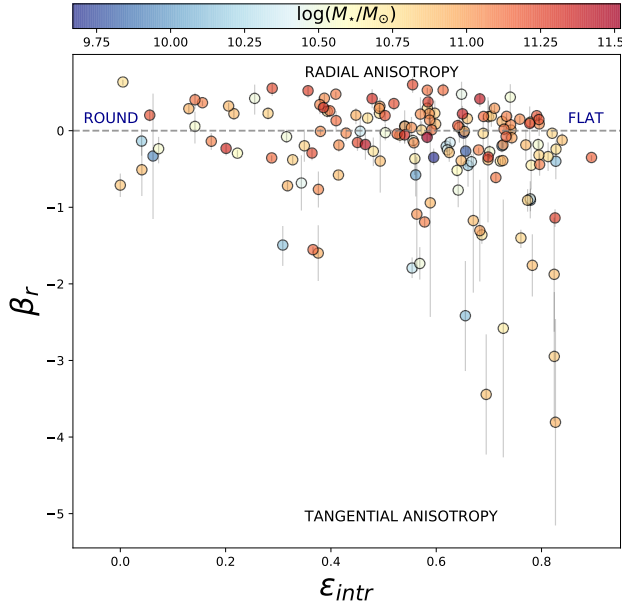
Figure 9. Velocity dispersion anisotropy in spherical coordinates β_r within $1R_e$ as a function of intrinsic ellipticity ($\varepsilon_{intr} = 1 - q$) at 1 R_e, color-coded by stellar mass. The grey dashed line represents isotropy, $\beta_r = 0$. Negative β_r indicates tangentially-anisotropic systems (supported by rotation), while positive β_r are radially-anisotropic systems (supported by random motions). Galaxies with very high ellipticity are close to isotropic or tangentially anisotropic. Radially-anisotropic galaxies are generally more massive.

Once we have constructed the edge-on projected maps, we measure the spin parameter within $1R_e$ by applying Equation 6. In order to produce results comparable to observations, we remeasure the MGE model on our edge-on projected maps to derive R_e, using the `MgeFit` python package (Cappellari 2002). We then derive the ellipticity by finding the model isophote with area $A = \pi R_e^2$, and use its ellipticity as the galaxy ellipticity (D'Eugenio et al. 2021). We show the derived edge-on $\lambda_{Re,EO}$ values as a function of the edge-on intrinsic ellipticity from our MGE fit, $\varepsilon_{intr,EO}$, in Fig. 10, color-coded by their velocity anisotropy β_r. The magenta line corresponds to the relation $\beta_z = 0.65 \times \varepsilon$ for edge-on galaxies as in Cappellari et al. (2007).

We find that $\lambda_{Re,EO}$ increases with increasing intrinsic ellipticity. In particular, galaxies that have low values of $\lambda_{Re,EO}$ are rounder than galaxies with higher values of $\lambda_{Re,EO}$. Moreover, we find that galaxies that are radially anisotropic (positive values of β_r) show low- to mid- values of ellipticity and $\lambda_{Re,EO}$, while galaxies with high ellipticity and $\lambda_{Re,EO}$ are more isotropic or tangentially anisotropic. This is seen more clearly when a locally weighted regression algorithm (LOESS - Cap-

pellari et al. 2013) is applied to the data to recover any mean underlying trend in β_r (Fig. 10, panel b). In general, the variation in β_r seems to mostly be driven by the spin parameter, $\lambda_{Re,EO}$.

The anti-correlation between $\lambda_{Re,EO}$ and β_r can be seen in Fig. 11. Testing the correlation using the Kendall's correlation coefficient τ, **we find a value of $\tau = -0.27$, with a probability of correlation of 99.99% that β_r decreases with increasing $\lambda_{Re,EO}$.** This means that fast-rotating galaxies are, as expected, more tangentially anisotropic than slow-rotating systems, which are more radially anisotropic.

4.5. *Orbital structure*

Stellar orbits can be characterized by two main properties: the time-averaged radius r, representing the size of each orbit, and the circularity $\lambda_z = \overline{L_z}/(r \times \overline{V_c})$, where $\overline{L_z}$ is the time averaged z-component of the orbit's angular momentum $(\overline{xv_y - yv_x})$, $r = \overline{\sqrt{x^2 + y^2 + z^2}}$, and $\overline{V_c} = \sqrt{v_i^2 + v_y^2 + v_z^2 + 2v_xv_y + 2v_xv_z + 2v_yv_z}$. The denominator represents the angular momentum of a typical circular orbit associated with the original orbit. Using the ratio of these two angular momentum terms, we can quantify the orbit circularity. $|\lambda_z| = 1$ represents highly-rotating short-axis tube orbits (circular orbits), while $\lambda_z = 0$ represents mostly box or long-axis tube (radial) orbits. Taking the radius, r, and the circularity, λ_z, of each orbit, and considering their weights given by the solution from the best-fit model, we can use the orbit circularity distribution in the phase space to obtain the probability density of orbits within $1R_e$, for each galaxy.

Figure 12 shows the overall orbit circularity distribution for all the galaxies in our sample, sorted by increasing stellar mass (shown in the top x-axis). The orbit circularity distribution is calculated by integrating the probability distribution of λ_z over all radii within $1R_e$ and normalizing it to unity. The colour of each square represents the normalized density, ω, of the orbits on the phase space. We divide the orbits into four broad categories (similar to Zhu et al. 2018a,c): cold orbits, $\lambda_z \geq 0.80$ (close to circular orbits); warm orbits, $0.25 < \lambda_z < 0.80$ (short-axis tube orbits with a component of rotation but also contribution of random motions); hot orbits, $-0.25 \geq \lambda_z \leq 0.25$ (mostly box orbits and long-axis tube orbits); counter-rotating orbits, $\lambda_z < -0.25$, (similar to the warm and cold components, but with opposite rotation). Overall, the amount of hot orbits increases with increasing stellar mass, while the number of warm and cold orbits becomes smaller with increasing mass.

To better visualize these trends with stellar mass, we calculate the luminosity-weighted fractions of each com-
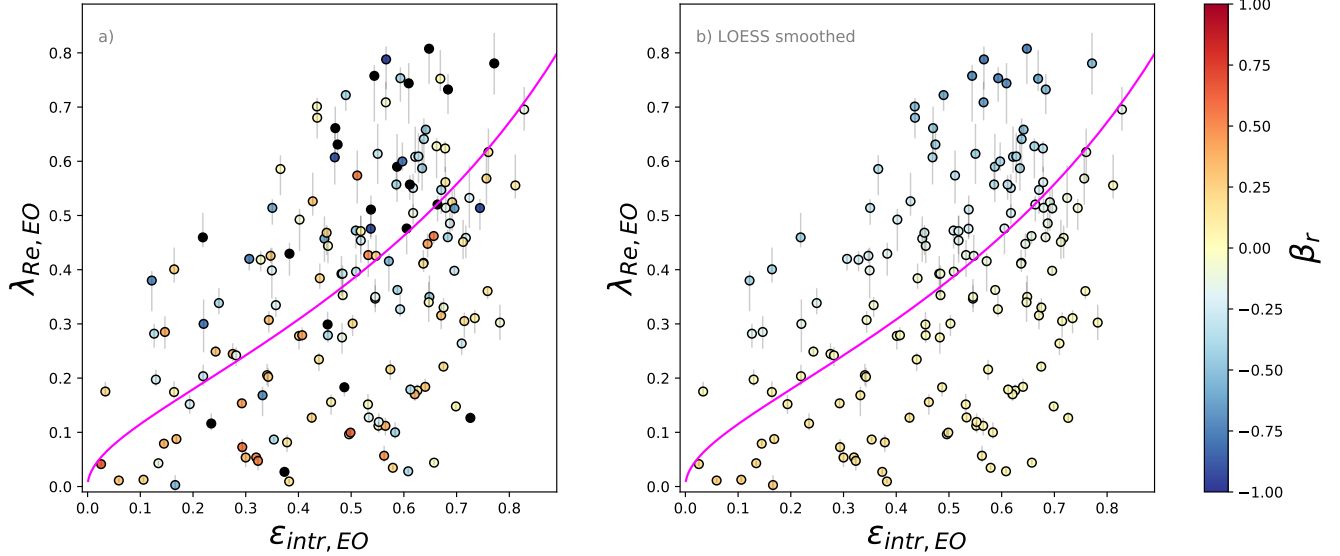
Figure 10. $\lambda_{Re,EO}$ as a function of the ellipticity $\varepsilon_{intr,EO}$ derived from MGE fits to the edge-on projected maps, calculated at $1\,R_e$. The magenta line corresponds to the relation $\beta_z = 0.65 \times \varepsilon$ for edge-on galaxies as in Cappellari et al. (2007). Galaxies are colored by their velocity anisotropy β_r in panel a and LOESS smoothed in panel b. As expected, $\lambda_{Re,EO}$ increases with increasing intrinsic ellipticity. Galaxies that are radially anisotropic show low- to mid- values of ellipticity and λ_{Re}, while galaxies with high ellipticity and $\lambda_{Re,EO}$ are more isotropic or tangentially anisotropic.
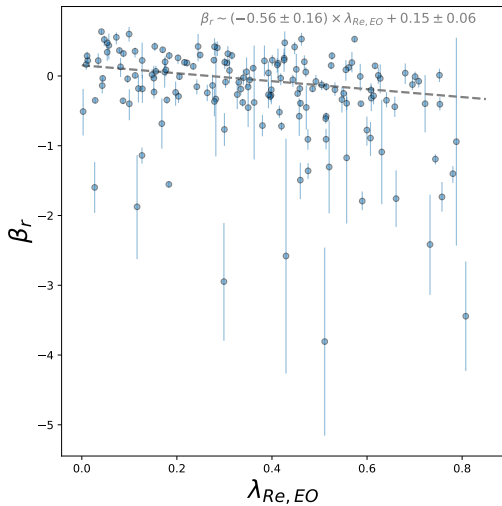
Figure 11. Velocity anisotropy β_r as a function of the intrinsic spin parameter $\lambda_{Re,EO}$. The dashed line is the linear best-fit to the data points (shown in the top right-hand corner). The two parameters are anti-correlated, so that β_r decreases with increasing $\lambda_{Re,EO}$. This means that fast-rotating galaxies are more likely to be tangentially anisotropic.

ponent within $1R_e$ and we show them as a function of stellar mass in Fig. 13, panel a. We also divide the sample into 4 mass bins with 29 galaxies each and we show the median values for each mass bin as bold points. **We find a clear increase in the fraction of hot or-bits with increasing stellar mass ($\tau = 0.16$, with a probability of correlation of 99.71%), while the fraction of warm orbits decreases with increasing stellar mass ($\tau = -0.19$, with a probability of correlation of 99.95%), both of them showing a large scatter. In particular, the fraction of hot and warm orbits seem to have a sharp change above $\log M_\star/M_\odot = 11$. The fraction of cold orbits only have a weak correlation with mass ($\tau = -0.10$, with a probability of correlation of 94.21%), declining towards more massive galaxies. The fraction of counter-rotating orbits does not seem to depend on stellar mass ($\tau = 0.05$, with a probability of correlation of 61.44%).**

We also explore the correlation of the fractions of the orbital components with the bulge to total flux ratio, B/T in panel b, with the intrinsic spin parameter $\lambda_{Re,EO}$ in panel c and with the intrinsic ellipticity ε_{intr} in panel d. B/T ratios are calculated from the r-band photometry, performing a 2D photometric bulge-disk decomposition (Barsanti et al. 2021 for the decomposition of cluster galaxies and Casura et al., in prep, for the galaxies in the GAMA region). Only 97 galaxies in our sample have reliable B/T values for the 2 component decomposition. The orbital fractions show a correlation with the B/T ratios similar to that with stellar mass.

Looking at $\lambda_{Re,EO}$ and ε_{intr} the orbital fractions have similar trends: hot orbits decrease with increasing $\lambda_{Re,EO}$ and ε_{intr}, warm orbits increase with increasing
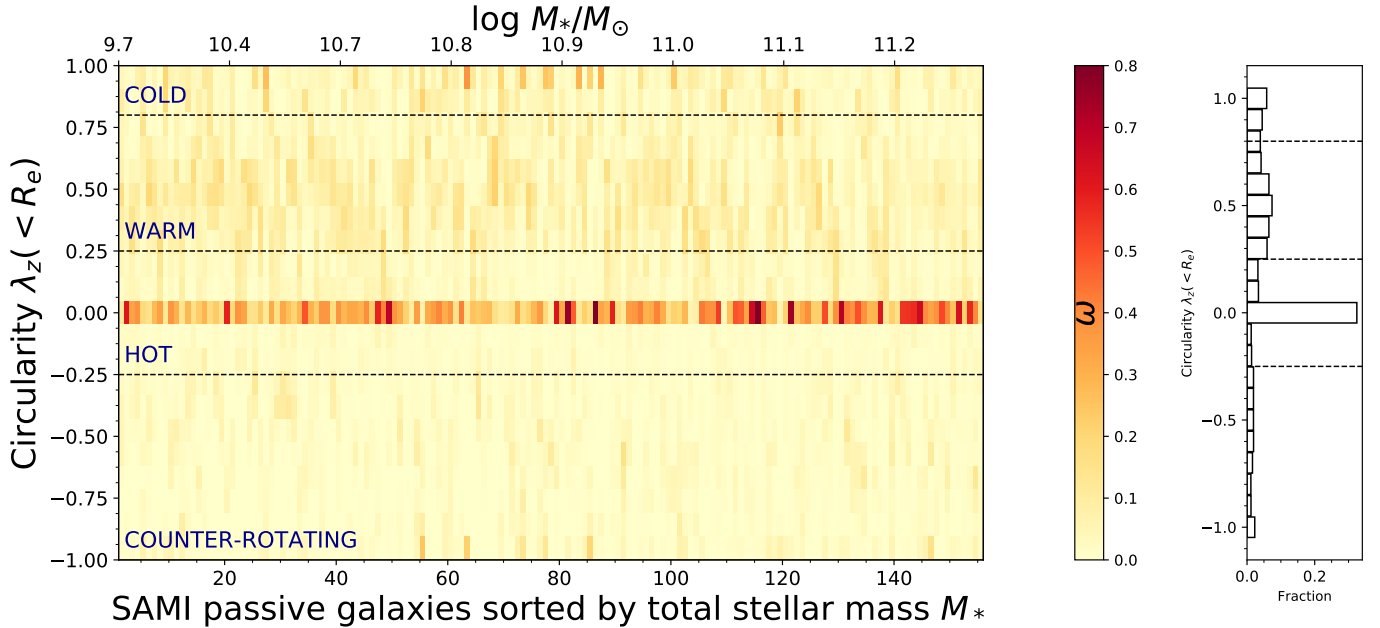
Figure 12. Overall orbit circularity distribution (calculated by integrating the probability distribution of λ_z, over all radii within $1R_e$ and normalizing it to unity), for all the galaxies in our sample, sorted by increasing stellar mass (shown in the top x-axis). The colour indicates the normalized density, ω, of the orbits on the phase space. The orbits are divided into four categories: cold orbits ($\lambda_z \geq 0.80$), warm orbits ($0.25 < \lambda_z < 0.80$), hot orbits ($-0.25 \geq \lambda_z \leq 0.25$) and counter-rotating orbits ($\lambda_z < -0.25$). Darker colors indicate higher probabilities as illustrated by the color bar. The right-hand panel shows the average orbit-circularity distribution within the mass range. Overall, the fraction of hot orbits seems to increase with increasing stellar mass, while the fraction of warm and cold orbits becomes smaller with increasing mass.

$\lambda_{Re,EO}$ and ε_{intr} and cold orbits show an increase in the fractions, **while there is a significant change ($\tau = -0.21$, with a probability of correlation of 99.99%) in the fraction of counter-rotating orbits only with $\lambda_{Re,EO}$, so that the fraction decreases with increasing $\lambda_{Re,EO}$.** In particular, we note that the trends with $\lambda_{Re,EO}$ are tighter than those with stellar mass (average 1-σ scatter ~ 0.09 compared to the average 1-σ scatter ~ 0.12 with stellar mass).

4.6. *Higher-order stellar kinematics and orbital components*

van de Sande et al. (2017a) used the higher-order stellar kinematic moments (h_3 and h_4) to classify galaxies in the SAMI Galaxy Survey into 5 distinct classes based on each galaxy's individual h_3 versus V/σ signature. Galaxies belonging to Class 1 are typically the most massive, large and red. Most of Class 1 galaxies are also classified as slow rotators, indicating that they have more complex dynamical structures as compared to fast rotators. Galaxies in Class 2-5 are all consistent with being oblate rotating axisymmetric spheroids as based on λ_{Re} and ε, but have a range of higher-order kinematic signatures. Galaxies in Class 2 are less massive, but still red, and reside in between slow and fast rotators. True fast rotators are in Class 3 and 4, with

galaxies showing a strong anti-correlation of V/σ and h_3. Galaxies in Class 5 have very high V/σ and ellipticity, but they do not show any anti-correlation with h_3. Here, we examine the connection between the distributions of these classes and the orbital components of the galaxies in our sample.

In Fig. 14 we show the overall orbit circularity distribution for all the galaxies in our sample, grouped by their kinematic classes. The orbit circularity distribution is calculated by integrating the probability distribution of λ_z over all radii within $R_{max,h3h4}$ and normalizing it to unity, similarly to Fig. 12. $R_{max,h3h4}$ is the radius within which the h_3 versus V/σ signatures were derived for each galaxy, due to S/N restrictions (van de Sande et al. 2017a). Within each subpanel in Fig. 14, we have ordered the galaxies by their intrinsic $\lambda_{Re,EO}$ values. The colour indicates the normalized density, ω, of the orbits on the phase space. There is a clear distinction between the orbital distributions, depending on the galaxy kinematic class. In general, hot orbits are more dominant in galaxies belonging to Class 1, and they decrease going towards Class 5, with Class 4 showing the lowest values. The contribution of cold orbits becomes more important in Classes 3, 4 and 5, while warm orbits can also be a significant fraction for galaxies in Class
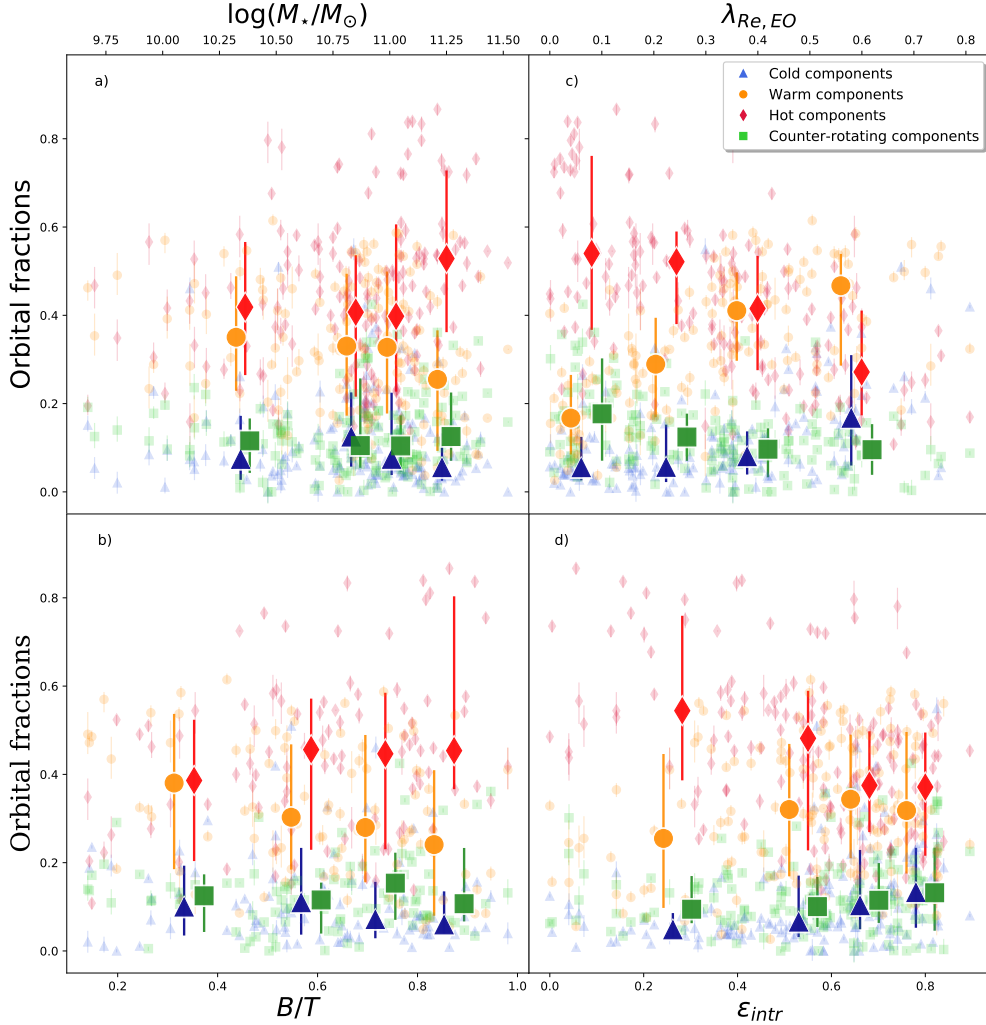
Figure 13. Fractions of orbital components as a function of: a) stellar mass, b) bulge to total flux ratio, B/T, c) $\lambda_{Re,EO}$, d) ε_{intr}. Bold points show the median values for each mass bin, with error bars representing the 1σ scatter around the median value. There is a clear increase of hot orbits (red diamonds) with increasing stellar mass (and B/T ratio), while the fraction of warm orbits (orange circles) decreases with increasing stellar mass (and B/T ratio), both of them showing a large scatter. Hot orbits decrease with increasing $\lambda_{Re,EO}$ (and ε_{intr}), while the fraction of warm orbit increases with increasing $\lambda_{Re,EO}$ (and ε_{intr}).The fraction of cold orbits (blue triangles) is also declining towards more massive galaxies and increases with galaxies becoming flatter. **The fraction of counter-rotating orbits (green squares) does not show any significant trend with B/T ratio or ε_{intr}, but it does decrease with increasing $\lambda_{Re,EO}$.** The correlation between the orbital fractions and $\lambda_{Re,EO}$ shows very little scatter.

2. Counter-rotating orbits do not have any significant contribution for Class 3 and 5.

The distribution of orbits in each class is clearer if we look at their integrated distributions, shown in Fig. 15. Within each class, there are also clear trends of the orbital components with λ_{Re}, so that, as expected, cold orbits are increasing with increasing λ_{Re} (rotationally supported galaxies). Similarly, warm orbits also increase with increasing $\lambda_{Re,EO}$. In contrast, the hot component becomes less important with increasing $\lambda_{Re,EO}$, while the counter-rotating orbits do not show any particular trend. In particular, in slow-rotating galaxies,

the main contribution is given by hot orbits. This is not unexpected, since these galaxies are expected to be pressure-supported. The warm component starts to become important for galaxies in Class 2, with its contribution increasing with increasing $\lambda_{Re,EO}$. Galaxies in Class 3, 4 and 5 show higher contributions from warm and cold orbits for all the galaxies (compared to Class 1 and 2). We do not find strong evidence for a difference in the orbital distribution between the higher-order kinematic Classes 3-5 as derived from the circularity diagram. Nonetheless, the existence of the different signatures in the higher-order moment maps points to kine-

matic features that are not captured in the λ_z–r space. This will be explored further in future work, but is beyond the scope of this paper.

5. DISCUSSION

We have constructed Schwarzschild orbit-superposition models of 161 passive galaxies from the SAMI Galaxy Survey in order to derive intrinsic properties such as the internal mass distribution, intrinsic stellar shape, velocity anisotropy and orbit circularity distribution. We find that changes in the internal structures are mostly correlated with the stellar mass of the galaxies.

5.1. *Comparison with previous studies*

5.1.1. *Fractions of dark matter*

We find an average value of the dark matter fraction of $f_{\rm DM} = 0.28$, with a standard deviation of 0.20, within $1R_e$. In general, our results for $f_{\rm DM}$ are broadly consistent with previous stellar dynamic determinations within $1R_e$ found in the literature which also all assume a NFW dark matter halo distribution (Fig. 16). For example, Gerhard et al. (2001) found $f_{\rm DM}$ = 0.1 − 0.4 from spherical dynamical modelling of 21 ETGs, Cappellari et al. (2006) inferred a median $f_{\rm DM}$ ≈ 0.3 by comparing dynamics and population masses of 25 ETGs, and assuming a universal IMF, Thomas et al. (2007, 2011) measured $f_{\rm DM} = 0.23 \pm 0.17$ via axisymmetric dynamical models of 17 ETGs, Cappellari et al. (2013) measured a $f_{\rm DM}$ of 0.15 for early-type galaxies in ATLAS^{3D} using Jeans Anisotropic Modelling (JAM), with galaxies showing an increasing fraction of dark matter with increasing mass for masses $\log(M_\star/M_\odot) > 10.6$, consistent with our findings here. Similar results were also found by Posacki et al. (2015), $f_{\rm DM} = 0.14$ for 55 early-type galaxies from stellar dynamics and lensing, and by Poci et al. (2017) - $f_{\rm DM} = 0.19$ using JAM to model a sample of 258 early-type galaxies in ATLAS^{3D}. For the Milky Way, Bland-Hawthorn & Gerhard (2016) found a $f_{\rm DM} = 0.3$, showing that baryons dominate the centres of galaxies, especially in our mass range, where the efficiency of galaxy building is peaking.

Jin et al. (2020) found a similar trend for early-type galaxies in the MaNGA sample, with the $f_{\rm DM}$ for the most massive galaxies $(11.0 < \log(M_\star/M_\odot) < 11.5)$ generally above 0.4, similar to what we see for galaxies in the same mass bin. However, we note that, as suggested by model tests with mock data from the Illustris simulations (Jin et al. 2019), estimations of $f_{\rm DM}$ can have a systematic offset as a result of modelling the dark matter halos assuming that galaxies follow a NFW profile, which may not be correct. This is an interesting aspect that will need to be explored further and tested

with a range of simulations and datasets. The trend we see in the $f_{\rm DM}$ with stellar mass is also consistent with predictions from simulations, where galaxies with $\log(M_\star/M_\odot) \sim 10.6$ are the most efficient at forming stars (e.g. Behroozi et al. 2010, 2013; Henriques et al. 2019). The physical interpretation of this behavior is the interplay between the feedback processes that impact star formation efficiency at different galaxy masses. Supernova feedback is more effective at reheating and expelling gas in low-mass galaxies, while AGN feedback is more effective in high-mass galaxies.

5.1.2. *Intrinsic shape distribution*

As seen in Fig. 8, the majority of our galaxies are **very close to oblate axisymmetric ($73\% \pm 3\%$), with $T_{\rm Re} \leq 0.1$, with varying degrees of intrinsic flattening, with $19\% \pm 3\%$ being mildly triaxial $(0.1 < T_{\rm Re} \geq 0.3)$ and a small percentage ($8\% \pm 3\%$) being triaxial/prolate ($T_{\rm Re} > 0.3$). There is a weak increase in the triaxiality parameter with increasing stellar mass. The percentage of galaxies that are non-oblate ($T_{Re} > 0.1$) increases with increasing stellar mass, going from $12\% \pm 4\%$ below $10^{10.50}M_\star/M_\odot$ to $29\% \pm 2\%$ above this mass.**

Triaxial Schwarzschild orbit-superposition dynamical models allow to measure intrinsic shapes directly. Previous studies used statistical methods to derive intrinsic shape properties; for example Kimm & Yi (2007) studied a sample of 3922 galaxies from SDSS (Adelman-McCarthy et al. 2006) and found that more massive galaxies are more likely to be triaxial than lower-mass galaxies. Foster et al. (2017) derived the intrinsic shape of 845 galaxies in the SAMI Galaxy Survey using an algorithm to simultaneously invert the distributions of apparent ellipticities and kinematic misalignments using the methodology of Weijmans et al. (2014). They find the majority ($\sim 85\%$) of the galaxies in their sample to be oblate axisymmetric, in good agreement with Weijmans et al. (2014) and our results. Our result is also in agreement with previous results from the Illustris simulations, where only a very small fraction of galaxies are found to have prolate shapes, with the fraction decreasing to zero prolate galaxies below $\log(M_\star/M_\odot) = 11.48$ (Li et al. 2018b). Jin et al. (2020) found higher fractions of triaxial and prolate galaxies in a sample of 149 early-type galaxies from the MaNGA survey. This discrepancy is partly explained by their higher stellar mass range analysed (their stellar masses ranged between $10^{9.9}$ and $10^{11.8}M_\odot$), and their different sample selection. Jin et al. (2020) also find an increase of the fraction of non-oblate galaxies with increasing stellar mass, in agreement with our results.
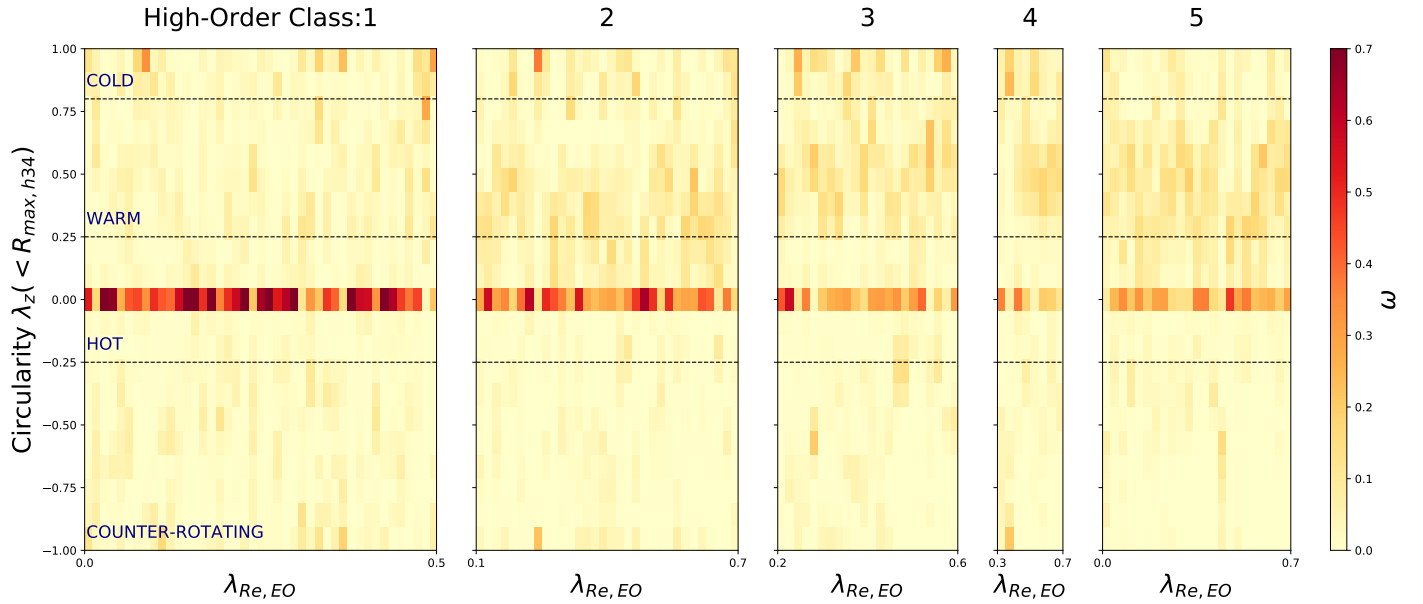
Figure 14. Orbit circularity distribution calculated by integrating the probability distribution of λ_z over all radii within $R_{\mathrm{max,h3h4}}$ and normalizing it to unity, for all the galaxies in our sample, grouped by their kinematic classes from van de Sande et al. (2017a) based on the higher-order (V/σ - h_3) signatures. Each class has been ordered by the intrinsic $\lambda_{Re,EO}$ values. The colour indicates the normalized density, ω, of the orbits on the phase space. Galaxies in Class 1 are dominated by hot orbits. Warm orbits become important for galaxies in Class 2, in particular at higher values of $\lambda_{Re,EO}$, with the warm orbits contribution increasing for Classes 3, 4 and 5. Hot orbits become less important with increasing $\lambda_{Re,EO}$.

5.1.3. *Velocity Anisotropy*

We find that galaxies with higher ellipticities have, in general, more negative values of β_r. This means that flatter galaxies are more tangentially anisotropic than rounder galaxies, while the latter are more likely to be supported by radial anisotropy. Moreover, we find a tight relationship of β_r with $\lambda_{Re,EO}$. This is not unexpected, since both parameters are a measure of rotation. The idea that the most giant early-type galaxies are not flattened by rotation but by anisotropy was proposed in the late 1970s (Bertola & Capaccioli 1977; Illingworth 1977; Binney 1978), however most of the dynamical modelling methods available to date do not allow for triaxiality, which is needed for a significant fraction of massive galaxies in order to construct accurate models.

Our results are also in agreement with more recent studies. For example, Gerhard et al. (2001) found that most of the galaxies in their sample of 21 ETGs were moderately radially anisotropic ($\beta_r \approx 0.2$), in agreement with the values we find in this study.

5.1.4. *Orbital structures*

We find that the hot orbital component generally dominates within R_{e}, becoming the most prevalent component among galaxies with total stellar mass $\log(M_\star/M_\odot) > 11$. As expected, bulge-dominated galaxies have high fractions of hot orbits (consistent with a pressure-supported bulge). In most galaxies a substantial number of stars within R_{e} are on warm orbits, with the contribution becoming more important at lower stellar masses. The cold component rarely dominates within R_{e} and its importance decreases with increasing stellar mass. The counter-rotating component is roughly constant for galaxies at all masses.

Stellar orbit distributions have only been derived explicitly before for two large (N>100) samples of galaxies, in the CALIFA (Zhu et al. 2018c) and MaNGA (Jin et al. 2020) surveys. We show the orbital fractions derived for early-type CALIFA and MaNGA galaxies, as well as the results from this work, in Fig. 17. The variations of the fraction of orbits is in good agreement with the general trends with stellar mass seen by Zhu et al. (2018c) and Jin et al. (2020). Jin et al. (2020) also found an increase in the fraction of hot orbits for massive ($\log(M_\star/M_\odot) > 11$) galaxies, similar to what we find.

Previous studies that did not have access to stellar orbit modelling, commonly used the proxy for the spin parameter λ_{Re}, and the flattening of galaxies, to shed light on galaxy intrinsic properties. Schwarzschild dynamical models allow us to explain the trends in λ_{Re} by showing the contributions from different orbital components, providing a new insight into how λ_{Re} is built-up. We measured the edge-on $\lambda_{Re,EO}$ from our model fits and compared it to the orbital fractions, shown in Fig.
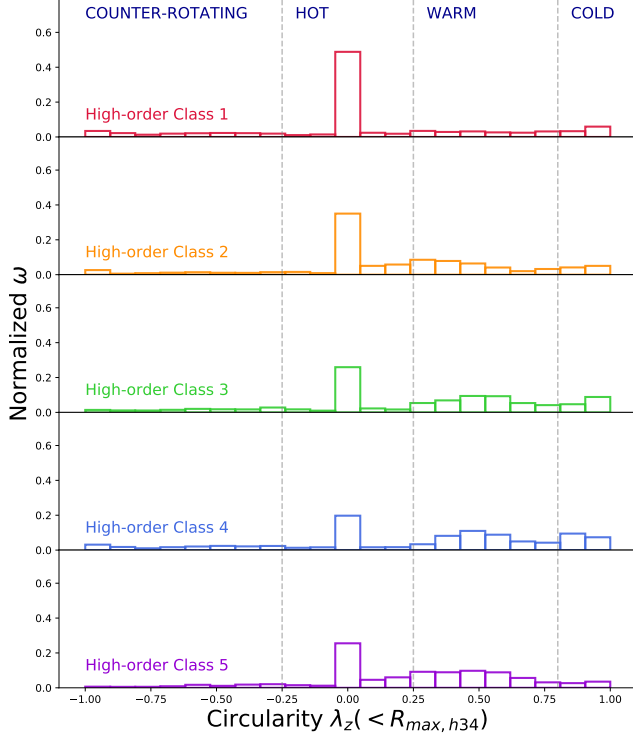
Figure 15. Normalized density of orbits as a function of the orbit circularity λ_z for each kinematic class from van de Sande et al. (2017a) based on the higher-order (V/σ - h_3) signatures. There is a decrease in the contribution from hot orbits going from Class 1 to 5, with Class 4 having the lowest value. Warm orbits become more important from Class 2 to Class 5. Counter-rotating orbits do not have any significant contribution for Class 3 and 5.
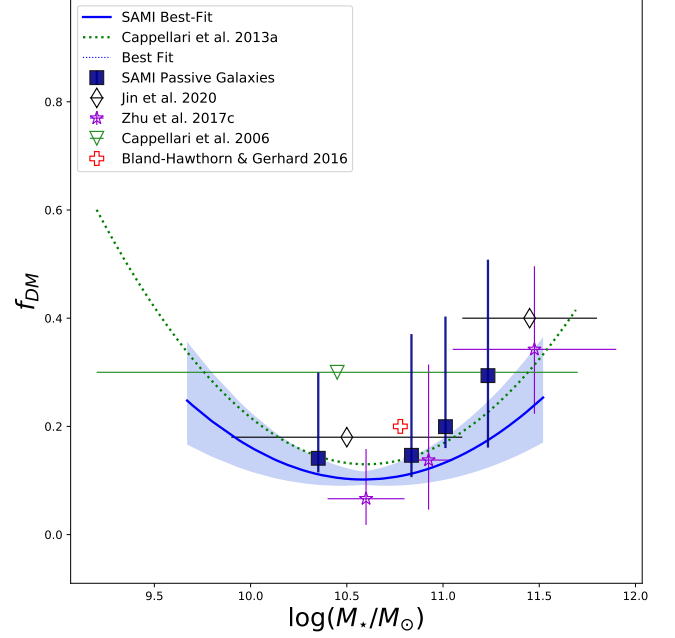
Figure 16. Median values of the fractions of dark matter ($f_{DM} = M_{dark}/M_{tot}$) within 1 R_e as a function of stellar mass for: SAURON (green triangle, Cappellari et al. 2006), ATLAS 3D (green dotted line, Cappellari et al. 2013 - derived with a cosmologically-motivated NFW halo) galaxies, the Milky Way (red cross, Bland-Hawthorn & Gerhard 2016), CALIFA (purple stars, Zhu et al. 2018b), (MaNGA (black diamonds, Jin et al. 2020) and SAMI (dark blue squares and blue solid line). Horizontal error bars delimit the mass range covered by each study. **Vertical error bars mark the 25th and 75th percentiles, when available.** The shaded region represents the error on the best-fit line for SAMI galaxies. Our results are in good agreement with the results presented in the literature.

¹⁰⁸² 14. We find a clear trend of the fractions of orbits with
¹⁰⁸³ $\lambda_{Re,EO}$: hot orbits show a rapid decrease in fraction with
¹⁰⁸⁴ increasing $\lambda_{Re,EO}$, while warm orbits have the opposite
¹⁰⁸⁵ behaviour (increasing rapidly with increasing $\lambda_{Re,EO}$).
¹⁰⁸⁶ Counter-rotating orbits have slightly lower fractions for
¹⁰⁸⁷ galaxies with higher spin parameter, while cold orbits
¹⁰⁸⁸ show low fractions up to $\lambda_{Re,EO} \approx 0.3$, after which
¹⁰⁸⁹ their importance starts to increase. This confirms that
¹⁰⁹⁰ $\lambda_{Re,EO}$ is a good indicator of the underlying orbit distri-
¹⁰⁹¹ bution of a galaxy. The observed spin parameter used in
¹⁰⁹² the literature (e.g. Cappellari et al. 2007; Emsellem et al.
¹⁰⁹³ 2007, 2011; van de Sande et al. 2017a) is a projected
¹⁰⁹⁴ quantity along an often-unknown line-of-sight viewing
¹⁰⁹⁵ angle. Slow rotators are found to be more massive, dom-
¹⁰⁹⁶ inating above $2 \times 10^{11} M_\odot$ (e.g. Emsellem et al. 2011;
¹⁰⁹⁷ Cappellari 2016; Brough et al. 2017; Veale et al. 2017;
¹⁰⁹⁸ Greene et al. 2017; van de Sande et al. 2017b, 2021b).
¹⁰⁹⁹ This is in agreement with our more direct orbit-based
¹¹⁰⁰ finding of an increase of the hot component with increas-

¹¹⁰¹ ing galaxy mass and the hot component starting to be
¹¹⁰² dominating for galaxies with $\log(M_\star/M_\odot) > 10.75$.

¹¹⁰³ ## 5.2. *Implications for galaxy formation*

¹¹⁰⁴ While the degeneracy due to deprojection impacts
¹¹⁰⁵ the reliability of the recovered shape (Rybicki 1987;
¹¹⁰⁶ Krajnović et al. 2005; de Nicola et al. 2020), the
¹¹⁰⁷ Schwarzschild orbit-superposition method is still the
¹¹⁰⁸ best method that exists to derive the true three-
¹¹⁰⁹ dimensional structure of individual galaxies. In this
¹¹¹⁰ paper we find that the changes of internal structures
¹¹¹¹ within $1R_e$ are correlated with the total stellar mass of
¹¹¹² individual galaxies. **In particular, we find a rapid**
¹¹¹³ **change in structure for galaxies above a stellar**
¹¹¹⁴ **mass $\log(M_\star/M_\odot) \sim 11$. Below this stellar mass,**
¹¹¹⁵ **galaxies tend to be oblate and with a substan-**
¹¹¹⁶ **tial number of stars within R_e on warm orbits,**
¹¹¹⁷ **while higher-mass galaxies with $\log(M_\star/M_\odot) > 11$**
¹¹¹⁸ **tend to be more triaxial and dominated by hot**
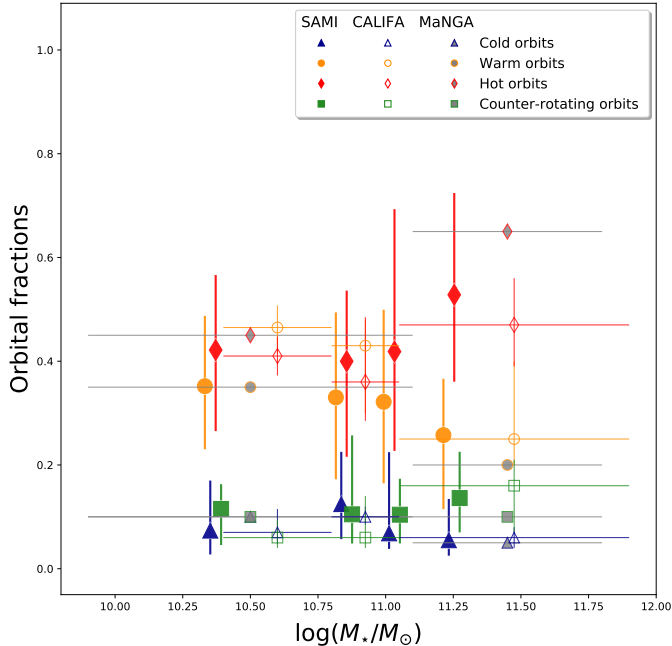
Figure 17. Median values of the fractions of orbital components as a function of stellar mass. The cold component is shown in blue, the warm component in orange, hot component in red and counter rotating in green. SAMI passive galaxies are shown as filled points, MaNGA early-type galaxies as open points (Jin et al. 2020) and the shaded areas represent the median values of early-type galaxies in the CALIFA sample (Zhu et al. 2018c). Horizontal error bars delimit the mass range covered. **Vertical error bars mark the 25th and 75th percentiles, when available.** The distribution of the fractions of orbits in SAMI and MaNGA are similar. All three samples show similar trends of orbital fractions with stellar mass.

orbits. A similar change is also seen in the fraction of dark matter (Fig 7). The change in the hot and warm orbital fractions that we observe in Fig. 13 at stellar masses higher than $\sim 10^{11} M_\star$ and the change in intrinsic shape at similar mass that we see in Fig. 8 could be interpreted as an indication of different formation channels. In particular, major and minor mergers are found to be the main driver of triaxial and prolate shapes, while exclusively very minor mergers are largely associated with triaxial systems and oblate slow rotators are formed in the absence of mergers (Lagos et al. 2020). The increasing fractions of hot orbits with increasing stellar mass supports a scenario where the most massive slow rotators form via gas-poor major mergers (Li et al. 2018b).

The trends we observe in the inner parts of passive galaxies (within $1R_e$) are generally consistent with the two formation paths of early-type galaxies proposed by Cappellari (2016). In this picture slow-rotating ETGs

assemble near the centre of massive dark matter halos via intense star formation at high redshift, and their evolution is dominated by gas-poor mergers. These galaxies are more likely to be triaxial and more massive, in agreement with what we find. By comparison, low-mass fast-rotating ETGs grow via gas accretion and their structures show similarities with that of spiral galaxies. Moreover, since the warm component can be interpreted as being similar to a thick disk, the increasing contribution that we see from warm orbits in fast-rotating galaxies provides further evidence for disk-like components in these systems as indicated by Krajnović et al. (2008).

Simulations suggest that stars on different orbits have different formation paths. The cold components are mostly young stars formed in-situ, the warm component likely traces old stars formed in-situ, or stars being heated from cold disks via secular evolution, and a small fraction of the warm component stars could be accreted (Gómez et al. 2017; Park et al. 2021). The stars on hot orbits in the outer regions should mostly be accreted (Gómez et al. 2017; Tissera et al. 2017) via minor or major mergers, while stars on hot orbits in the inner regions are predicted to have formed at high-redshift. Further comparison with simulations will help us to understand the physical processes that lead to the orbit distribution observed at present times.

5.2.1. *Evidence of early accretion from stellar populations*

Resolved stellar dynamics trace the change in angular momentum and orbital distribution of stars due to mergers, but major mergers are likely to have obscured the effects of earlier interactions. However, evidence of these earlier interactions can be found in the stellar populations. In particular, a galaxy's mean stellar age provides information on when the stars were formed (e.g. Tinsley 1980; Bender et al. 1993; Park et al. 2021). So combining stellar population and stellar kinematic studies can provide unique but complementary insights into how galaxies build-up their stellar mass and angular momentum.

van de Sande et al. (2018) studied a sample of galaxies in the SAMI Galaxy Survey and found that there is a strong relation between V/σ_{Re} and mean stellar age, such that galaxies with young stellar populations are predominantly rotationally supported, whereas galaxies with old stellar populations are more pressure supported by random orbital motion of stars. For the large majority of galaxies that are oblate-rotating spheroids, they found that characteristic stellar age is related to the intrinsic ellipticity of galaxies. They studied a full range of morphologies, but showed that this trend is still ob-

served when galaxies are in early-type or late-type sub-samples.

To check whether this relation holds for our parameters derived using Schwarzschild models, we color-code our data in the $\lambda_{Re,EO} - \varepsilon_{intr,EO}$ plot by luminosity-weighted, mean stellar population age (see Scott et al. 2017) in Fig. 18 and use LOESS smoothing to recover any mean underlying trend. We find a good match to the trends as found by van de Sande et al. (2018), with slow-rotating galaxies being generally older and rounder than fast-rotating galaxies. This relationship is consistent with predictions from hydrodynamical cosmological simulations and observations, where slow-rotating galaxies form via intense star formation at high redshift, and evolve from a set of processes dominated by gas-poor mergers (Cappellari 2016).

All the results presented here are in agreement with a formation scenario in which passive galaxies form through two main channels and where the changes of internal structures within $1R_e$ are generally correlated with the total stellar mass of the individual galaxies.
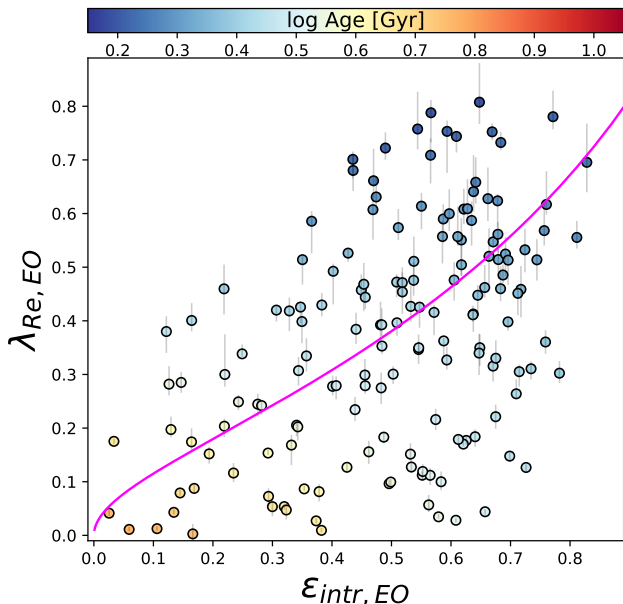
Figure 18. $\lambda_{Re,EO}$ as a function of the intrinsic ellipticity $\varepsilon_{intr,EO}$, calculated at $1R_e$. The magenta line represents the relation between the anisotropy parameter β_z and the intrinsic ellipticity $\varepsilon_{intr,EO}$, for galaxies viewed edge-on, that bounds all regular rotating galaxies. Galaxies are color-coded by log Age, and LOESS smoothed to recover any mean underlying trend. Older galaxies are generally slow-rotating and rounder than younger systems.

6. CONCLUSION

We constructed Schwarzschild orbit-superposition models of 161 passive galaxies, from the SAMI Galaxy Survey, with stellar masses raging from $9.5 < \log(M_\star/M_\odot) < 11.4$. We derived intrinsic properties such as the internal mass distribution (for both stellar and dark matter), intrinsic stellar shape (axis ratios and ellipticity), velocity anisotropy and orbit circularity distribution which gives us the most-detailed insight into their assembly history. We draw the following conclusions:

- Passive galaxies have an average dark matter fraction $f_{DM} = 0.28 \pm 0.20$, consistent with previous results (Fig. 16).

- **The majority of our galaxies are very close to oblate axisymmetric ($73\% \pm 3\%$), with $T_{Re} \leq 0.1$, with varying degrees of intrinsic flattening, with $19\% \pm 3\%$ being mildly triaxial ($0.1 < T_{Re} \geq 0.3$) and a small percentage ($8\% \pm 3\%$) being triaxial/prolate ($T_{Re} > 0.3$). The fraction of non-oblate galaxies increases with increasing stellar mass, with a sudden change at $\sim 10^{10.50} M_\star/M_\odot$ (Fig. 8).**

- Galaxies with high intrinsic ellipticity (flat galaxies, $\varepsilon > 0.7$) are found to be more isotropic ($\beta_r \sim 0$) or more tangentially anisotropic ($\beta_r < 0$; Fig. 9). β_r is anti-correlated with the spin parameter $\lambda_{Re,EO}$, so that β_r decreases with increasing $\lambda_{Re,EO}$, consistent with slow-rotating galaxies being more radially anisotropic and fast-rotating galaxies being more tangentially anisotropic (Fig. 11).

- By dividing the stellar orbital distribution into cold, warm, hot, and counter-rotating components, we find that the hot component generally dominates within R_e, becoming the most prevalent component among galaxies with total stellar mass $\log(M_\star/M_\odot) > 11$. In most galaxies a substantial number ($\sim 40\%$ of stars within R_e are on warm orbits, with the warm contribution becoming more important at lower stellar masses. The contribution from the cold orbital components is small across stellar mass, with its contribution decreasing further with increasing mass. The counter-rotating component is roughly constant for galaxies at all masses (Fig. 13).

- The changes of internal structures (fraction of dark matter, f_{dm}, intrinsic shape and orbital distribution) within $1R_e$ are correlated with the total stellar mass of the individual galaxies.

- The fractions of orbits show tight correlations with the intrinsic $\lambda_{Re,EO}$, with hot orbits being dominant for slow-rotating galaxies and contributions from warm and cold orbits becoming more important with increasing $\lambda_{Re,EO}$. We also find a clear distinction between the orbital distributions of galaxies, depending on their kinematic class (from van de Sande et al. (2017a) based on the higher-order V/σ - h_3 signatures). Class 1 is dominated by hot orbits, with little contribution from other components. The contribution of warm orbits increases from Class 2 to 5, while the contribution from hot orbits become less important. Class 4 and 5 also show contributions from cold and counter rotating components (Fig. 14 and 15).

- These results are in agreement with a formation scenario in which galaxies form through two main different channels. Slow-rotating ETGs assemble near the centre of massive dark matter halos via intense star formation at high redshift, and their evolution is dominated by gas-poor mergers. These galaxies are more likely to be triaxial and more massive, dominated by radial anisotropy, in agreement with what we find. By comparison, low-mass fast-rotating ETGs grow via gas accretion and their structures show similarities with that of spiral galaxies. Moreover, the intrinsic shapes of slow rotators could point to different type of mergers in their evolutionary history.

We recommend the inclusion of the higher-order kinematic moments h_3 and h_4 in future works since even values with high uncertainties improve the model fits. Moreover, since h_3 and h_4 are quantities that are predicted to be connected with a galaxy's assembly history (Naab et al. 2014), studying their relation to the internal orbital structure of galaxies provides an extra tool to help disentangle the different possible formation scenarios. We did not find a significant difference between the orbital components of fast-rotating galaxies in different classes (determined using the V/sigma- h3 correlation) in the $\lambda_z - r$ space (Fig. 14), but this is an interesting aspect that should be further explored in future works with larger samples of accurate h_3 and h_4 values (e.g. the forthcoming Hector survey; Bryant et al. 2016).

ACKNOWLEDGEMENTS

We thank the anonymous referee for their comments that helped to improve this manuscript. We thank

Scipy (Virtanen et al. 2020), UNSW Katana computational cluster (Smith & Betbeder-Matibet 2010).

REFERENCES

Adelman-McCarthy, J. K., Agüeros, M. A., Allam, S. S., et al. 2006, ApJS, 162, 38, doi: 10.1086/497917

Ahn, C. P., Alexandroff, R., Allende Prieto, C., et al. 2012, ApJS, 203, 21, doi: 10.1088/0067-0049/203/2/21

Aquino-Ortíz, E., Sánchez, S. F., Valenzuela, O., et al. 2020, arXiv e-prints, arXiv:2005.09149. https://arxiv.org/abs/2005.09149

Barsanti, S., Owers, M. S., McDermid, R. M., et al. 2021, The colors of bulges and disks in the core and outskirts of galaxy clusters. https://arxiv.org/abs/2012.12480

Behroozi, P. S., Conroy, C., & Wechsler, R. H. 2010, ApJ, 717, 379, doi: 10.1088/0004-637X/717/1/379

Behroozi, P. S., Wechsler, R. H., & Conroy, C. 2013, ApJ, 770, 57, doi: 10.1088/0004-637X/770/1/57

Bender, R. 1988, A&A, 202, L5

Bender, R., Burstein, D., & Faber, S. M. 1993, ApJ, 411, 153, doi: 10.1086/172815

Bertola, F., & Capaccioli, M. 1977, ApJ, 211, 697, doi: 10.1086/154980

Binney, J. 1978, MNRAS, 183, 501, doi: 10.1093/mnras/183.3.501

Binney, J., & Tremaine, S. 2008, Galactic Dynamics: Second Edition

Binney, J. J., Davies, R. L., & Illingworth, G. D. 1990, ApJ, 361, 78, doi: 10.1086/169169

Bland-Hawthorn, J., & Gerhard, O. 2016, ARA&A, 54, 529, doi: 10.1146/annurev-astro-081915-023441

Bland-Hawthorn, J., Bryant, J., Robertson, G., et al. 2011, Optics Express, 19, 2649, doi: 10.1364/OE.19.002649

Breddels, M. A., & Helmi, A. 2014, ApJL, 791, L3, doi: 10.1088/2041-8205/791/1/L3

Brough, S., van de Sande, J., Owers, M. S., et al. 2017, ApJ, 844, 59, doi: 10.3847/1538-4357/aa7a11

Bryant, J. J., Bland-Hawthorn, J., Fogarty, L. M. R., Lawrence, J. S., & Croom, S. M. 2014, MNRAS, 438, 869, doi: 10.1093/mnras/stt2254

Bryant, J. J., Owers, M. S., Robotham, A. S. G., et al. 2015, MNRAS, 447, 2857, doi: 10.1093/mnras/stu2635

Bryant, J. J., Bland-Hawthorn, J., Lawrence, J., et al. 2016, in Society of Photo-Optical Instrumentation Engineers (SPIE) Conference Series, Vol. 9908, Ground-based and Airborne Instrumentation for Astronomy VI, ed. C. J. Evans, L. Simard, & H. Takami, 99081F, doi: 10.1117/12.2230740

Büdenbender, A., van de Ven, G., & Watkins, L. L. 2015, MNRAS, 452, 956, doi: 10.1093/mnras/stv1314

Bundy, K., Bershady, M. A., Law, D. R., et al. 2015, ApJ, 798, 7, doi: 10.1088/0004-637X/798/1/7

Cappellari, M. 2002, MNRAS, 333, 400, doi: 10.1046/j.1365-8711.2002.05412.x

—. 2016, ARA&A, 54, 597, doi: 10.1146/annurev-astro-082214-122432

—. 2017, MNRAS, 466, 798, doi: 10.1093/mnras/stw3020

Cappellari, M., & Copin, Y. 2003, MNRAS, 342, 345, doi: 10.1046/j.1365-8711.2003.06541.x

Cappellari, M., & Emsellem, E. 2004, PASP, 116, 138, doi: 10.1086/381875

Cappellari, M., Bacon, R., Bureau, M., et al. 2006, MNRAS, 366, 1126, doi: 10.1111/j.1365-2966.2005.09981.x

Cappellari, M., Emsellem, E., Bacon, R., et al. 2007, MNRAS, 379, 418, doi: 10.1111/j.1365-2966.2007.11963.x

Cappellari, M., Emsellem, E., Krajnović, D., et al. 2011, MNRAS, 413, 813, doi: 10.1111/j.1365-2966.2010.18174.x

Cappellari, M., McDermid, R. M., Alatalo, K., et al. 2013, MNRAS, 432, 1862, doi: 10.1093/mnras/stt644

Chabrier, G. 2003, ApJL, 586, L133, doi: 10.1086/374879

Chandrasekhar, S. 1969, Ellipsoidal figures of equilibrium

Cortese, L., Fogarty, L. M. R., Bekki, K., et al. 2016, MNRAS, 463, 170, doi: 10.1093/mnras/stw1891

Cretton, N., de Zeeuw, P. T., van der Marel, R. P., & Rix, H.-W. 1999, ApJS, 124, 383, doi: 10.1086/313264

Croom, S. M., Lawrence, J. S., Bland-Hawthorn, J., et al. 2012, Monthly Notices of the Royal Astronomical Society, 421, 872, doi: 10.1111/j.1365-2966.2011.20365.x

Croom, S. M., Owers, M. S., Scott, N., et al. 2021, MNRAS, doi: 10.1093/mnras/stab229

de Nicola, S., Saglia, R. P., Thomas, J., Dehnen, W., & Bender, R. 2020, MNRAS, 496, 3076, doi: 10.1093/mnras/staa1703

de Zeeuw, P. T., Bureau, M., Emsellem, E., et al. 2002, MNRAS, 329, 513, doi: 10.1046/j.1365-8711.2002.05059.x

del Moral-Castro, I., García-Lorenzo, B., Ramos Almeida, C., et al. 2020, A&A, 639, L9, doi: 10.1051/0004-6361/202038091

den Brok, M., Krajnović, D., Emsellem, E., Brinchmann, J., & Maseda, M. 2021, arXiv e-prints, arXiv:2109.14640. https://arxiv.org/abs/2109.14640

24

D'Eugenio, F., Colless, M., Scott, N., et al. 2021, MNRAS, doi: 10.1093/mnras/stab1146

Driver, S. P., Hill, D. T., Kelvin, L. S., et al. 2011, MNRAS, 413, 971, doi: 10.1111/j.1365-2966.2010.18188.x

Emsellem, E., Monnet, G., & Bacon, R. 1994, A&A, 285, 723

Emsellem, E., Cappellari, M., Peletier, R. F., et al. 2004, MNRAS, 352, 721, doi: 10.1111/j.1365-2966.2004.07948.x

Emsellem, E., Cappellari, M., Krajnović, D., et al. 2007, MNRAS, 379, 401, doi: 10.1111/j.1365-2966.2007.11752.x

—. 2011, MNRAS, 414, 888, doi: 10.1111/j.1365-2966.2011.18496.x

Fahrion, K., Lyubenova, M., van de Ven, G., et al. 2019, A&A, 628, A92, doi: 10.1051/0004-6361/201935832

Falcón-Barroso, J., Lyubenova, M., van de Ven, G., et al. 2017, A&A, 597, A48, doi: 10.1051/0004-6361/201628625

Falcón-Barroso, J., van de Ven, G., Lyubenova, M., et al. 2019, A&A, 632, A59, doi: 10.1051/0004-6361/201936413

Fall, S. M., & Efstathiou, G. 1980, MNRAS, 193, 189, doi: 10.1093/mnras/193.2.189

Fasano, G., Bettoni, D., Ascaso, B., et al. 2010, MNRAS, 404, 1490, doi: 10.1111/j.1365-2966.2010.16361.x

Feldmeier-Krause, A., Zhu, L., Neumayer, N., et al. 2017, MNRAS, 466, 4040, doi: 10.1093/mnras/stw3377

Foster, C., van de Sande, J., D'Eugenio, F., et al. 2017, MNRAS, 472, 966, doi: 10.1093/mnras/stx1869

Fraser-McKelvie, A., Cortese, L., van de Sande, J., et al. 2021, MNRAS, 503, 4992, doi: 10.1093/mnras/stab573

Gebhardt, K., Richstone, D., Tremaine, S., et al. 2003, ApJ, 583, 92, doi: 10.1086/345081

Gerhard, O., Kronawitter, A., Saglia, R. P., & Bender, R. 2001, AJ, 121, 1936, doi: 10.1086/319940

Gerhard, O. E. 1993, MNRAS, 265, 213, doi: 10.1093/mnras/265.1.213

Gómez, F. A., Grand, R. J. J., Monachesi, A., et al. 2017, MNRAS, 472, 3722, doi: 10.1093/mnras/stx2149

Greene, J. E., Leauthaud, A., Emsellem, E., et al. 2017, ApJL, 851, L33, doi: 10.3847/2041-8213/aa8ace

Hagen, J. H. J., Helmi, A., de Zeeuw, P. T., & Posti, L. 2019, A&A, 629, A70, doi: 10.1051/0004-6361/201935264

Henriques, B. M. B., White, S. D. M., Lilly, S. J., et al. 2019, MNRAS, 485, 3446, doi: 10.1093/mnras/stz577

Hill, D. T., Kelvin, L. S., Driver, S. P., et al. 2011, MNRAS, 412, 765, doi: 10.1111/j.1365-2966.2010.17950.x

Illingworth, G. 1977, ApJL, 218, L43, doi: 10.1086/182572

Jesseit, R., Cappellari, M., Naab, T., Emsellem, E., & Burkert, A. 2009, MNRAS, 397, 1202, doi: 10.1111/j.1365-2966.2009.14984.x

Jethwa, P., Thater, S., Maindl, T., & Van de Ven, G. 2020, DYNAMITE: DYnamics, Age and Metallicity Indicators Tracing Evolution. http://ascl.net/2011.007

Jin, Y., Zhu, L., Long, R. J., et al. 2020, MNRAS, 491, 1690, doi: 10.1093/mnras/stz3072

—. 2019, MNRAS, 486, 4753, doi: 10.1093/mnras/stz1170

Kimm, T., & Yi, S. K. 2007, ApJ, 670, 1048, doi: 10.1086/522573

Kireeva, E. N., & Kondratyev, B. P. 2019, Astronomy Reports, 63, 713, doi: 10.1134/S106377291909004X

Krajnović, D., Cappellari, M., Emsellem, E., McDermid, R. M., & de Zeeuw, P. T. 2005, MNRAS, 357, 1113, doi: 10.1111/j.1365-2966.2005.08715.x

Krajnović, D., McDermid, R. M., Cappellari, M., & Davies, R. L. 2009, MNRAS, 399, 1839, doi: 10.1111/j.1365-2966.2009.15415.x

Krajnović, D., Bacon, R., Cappellari, M., et al. 2008, MNRAS, 390, 93, doi: 10.1111/j.1365-2966.2008.13712.x

Krajnović, D., Weilbacher, P. M., Urrutia, T., et al. 2015, MNRAS, 452, 2, doi: 10.1093/mnras/stv958

Kuijken, K., Fisher, D., & Merrifield, M. R. 1996, MNRAS, 283, 543, doi: 10.1093/mnras/283.2.543

Lagos, C. d. P., Emsellem, E., van de Sande, J., et al. 2020, arXiv e-prints, arXiv:2012.08060. https://arxiv.org/abs/2012.08060

Lawson, C. L., & Hanson, R. J. 1974, Solving least squares problems

Li, H., Mao, S., Cappellari, M., et al. 2018a, ApJL, 863, L19, doi: 10.3847/2041-8213/aad54b

Li, H., Mao, S., Emsellem, E., et al. 2018b, MNRAS, 473, 1489, doi: 10.1093/mnras/stx2374

Liepold, C. M., Quenneville, M. E., Ma, C.-P., et al. 2020, ApJ, 891, 4, doi: 10.3847/1538-4357/ab6f71

Lipka, M., & Thomas, J. 2021, MNRAS, 504, 4599, doi: 10.1093/mnras/stab1092

Lyubenova, M., van den Bosch, R. C. E., Côté, P., et al. 2013, MNRAS, 431, 3364, doi: 10.1093/mnras/stt414

Ma, C.-P., Greene, J. E., McConnell, N., et al. 2014, ApJ, 795, 158, doi: 10.1088/0004-637X/795/2/158

McConnell, N. J., Ma, C.-P., Gebhardt, K., et al. 2011, Nature, 480, 215, doi: 10.1038/nature10636

Naab, T., Johansson, P. H., & Ostriker, J. P. 2009, ApJL, 699, L178, doi: 10.1088/0004-637X/699/2/L178

Naab, T., Oser, L., Emsellem, E., et al. 2014, MNRAS, 444, 3357, doi: 10.1093/mnras/stt1919

Navarro, J. F., Frenk, C. S., & White, S. D. M. 1996, ApJ, 462, 563, doi: 10.1086/177173

Neureiter, B., Thomas, J., Saglia, R., et al. 2021, MNRAS, 500, 1437, doi: 10.1093/mnras/staa3014

Oser, L., Ostriker, J. P., Naab, T., Johansson, P. H., & Burkert, A. 2010, ApJ, 725, 2312, doi: 10.1088/0004-637X/725/2/2312

Owers, M. S., Allen, J. T., Baldry, I., et al. 2017, MNRAS, 468, 1824, doi: 10.1093/mnras/stx562

Owers, M. S., Hudson, M. J., Oman, K. A., et al. 2019, arXiv e-prints. https://arxiv.org/abs/1901.08185

Park, M.-J., Yi, S. K., Dubois, Y., et al. 2019, ApJ, 883, 25, doi: 10.3847/1538-4357/ab3afe

Park, M. J., Yi, S. K., Peirani, S., et al. 2021, ApJS, 254, 2, doi: 10.3847/1538-4365/abe937

Poci, A., Cappellari, M., & McDermid, R. M. 2017, MNRAS, 467, 1397, doi: 10.1093/mnras/stx101

Poci, A., McDermid, R. M., Zhu, L., & van de Ven, G. 2019, MNRAS, 487, 3776, doi: 10.1093/mnras/stz1154

Posacki, S., Cappellari, M., Treu, T., Pellegrini, S., & Ciotti, L. 2015, MNRAS, 446, 493, doi: 10.1093/mnras/stu2098

Quenneville, M. E., Liepold, C. M., & Ma, C.-P. 2021a, ApJS, 254, 25, doi: 10.3847/1538-4365/abe6a0

—. 2021b, arXiv e-prints, arXiv:2111.06904. https://arxiv.org/abs/2111.06904

Querejeta, M., Eliche-Moral, M. C., Tapia, T., et al. 2015, A&A, 579, L2, doi: 10.1051/0004-6361/201526354

Rodríguez, S., Padilla, N. D., & García Lambas, D. 2016, MNRAS, 456, 571, doi: 10.1093/mnras/stv2660

Rusli, S. P., Thomas, J., Saglia, R. P., et al. 2013, AJ, 146, 45, doi: 10.1088/0004-6256/146/3/45

Rybicki, G. B. 1987, in Structure and Dynamics of Elliptical Galaxies, ed. P. T. de Zeeuw, Vol. 127, 397, doi: 10.1007/978-94-009-3971-4_41

Sánchez, S. F., Kennicutt, R. C., Gil de Paz, A., et al. 2012, A&A, 538, A8, doi: 10.1051/0004-6361/201117353

Sánchez-Janssen, R., Méndez-Abreu, J., & Aguerri, J. A. L. 2010, MNRAS, 406, L65, doi: 10.1111/j.1745-3933.2010.00883.x

Sánchez-Janssen, R., Ferrarese, L., MacArthur, L. A., et al. 2016, ApJ, 820, 69, doi: 10.3847/0004-637X/820/1/69

Schwarzschild, M. 1979, ApJ, 232, 236, doi: 10.1086/157282

Scott, N., Cappellari, M., Davies, R. L., et al. 2009, MNRAS, 398, 1835, doi: 10.1111/j.1365-2966.2009.15275.x

Scott, N., Brough, S., Croom, S. M., et al. 2017, MNRAS, 472, 2833, doi: 10.1093/mnras/stx2166

Seth, A. C., van den Bosch, R., Mieske, S., et al. 2014, Nature, 513, 398, doi: 10.1038/nature13762

Shanks, T., Metcalfe, N., Chehade, B., et al. 2015, Monthly Notices of the Royal Astronomical Society, 451, 4238, doi: 10.1093/mnras/stv1130

Sharp, R., Saunders, W., Smith, G., et al. 2006, in Society of Photo-Optical Instrumentation Engineers (SPIE) Conference Series, Vol. 6269, Society of Photo-Optical Instrumentation Engineers (SPIE) Conference Series, ed. I. S. McLean & M. Iye, 62690G, doi: 10.1117/12.671022

Smith, D., & Betbeder-Matibet, L. 2010, Katana, doi: https://doi.org/10.26190/669x-a286

Taylor, E. N., Hopkins, A. M., Baldry, I. K., et al. 2011, MNRAS, 418, 1587, doi: 10.1111/j.1365-2966.2011.19536.x

Thater, S., Krajnović, D., Cappellari, M., et al. 2019, A&A, 625, A62, doi: 10.1051/0004-6361/201834808

Thater, S., Krajnović, D., Bourne, M. A., et al. 2017, A&A, 597, A18, doi: 10.1051/0004-6361/201629480

Thater, S., Krajnović, D., Weilbacher, P. M., et al. 2021, MNRAS, doi: 10.1093/mnras/stab3210

Thomas, D., Maraston, C., & Johansson, J. 2011, MNRAS, 412, 2183, doi: 10.1111/j.1365-2966.2010.18049.x

Thomas, J., Saglia, R. P., Bender, R., Erwin, P., & Fabricius, M. 2014, ApJ, 782, 39, doi: 10.1088/0004-637X/782/1/39

Thomas, J., Saglia, R. P., Bender, R., et al. 2007, MNRAS, 382, 657, doi: 10.1111/j.1365-2966.2007.12434.x

Tinsley, B. M. 1980, FCPh, 5, 287

Tissera, P. B., Machado, R. E. G., Vilchez, J. M., et al. 2017, A&A, 604, A118, doi: 10.1051/0004-6361/201628915

Valluri, M., Merritt, D., & Emsellem, E. 2004, ApJ, 602, 66, doi: 10.1086/380896

van de Sande, J., Bland-Hawthorn, J., Fogarty, L. M. R., et al. 2017a, ApJ, 835, 104, doi: 10.3847/1538-4357/835/1/104

van de Sande, J., Bland-Hawthorn, J., Brough, S., et al. 2017b, MNRAS, 472, 1272, doi: 10.1093/mnras/stx1751

van de Sande, J., Scott, N., Bland-Hawthorn, J., et al. 2018, Nature Astronomy, 2, 483, doi: 10.1038/s41550-018-0436-x

van de Sande, J., Croom, S. M., Bland-Hawthorn, J., et al. 2021a, MNRAS, doi: 10.1093/mnras/stab2647

van de Sande, J., Vaughan, S. P., Cortese, L., et al. 2021b, MNRAS, 505, 3078, doi: 10.1093/mnras/stab1490

van de Ven, G., de Zeeuw, P. T., & van den Bosch, R. C. E. 2008, MNRAS, 385, 614, doi: 10.1111/j.1365-2966.2008.12873.x

van de Ven, G., van den Bosch, R. C. E., Verolme, E. K., & de Zeeuw, P. T. 2006, A&A, 445, 513, doi: 10.1051/0004-6361:20053061

van den Bosch, R. C. E., van de Ven, G., Verolme, E. K., Cappellari, M., & de Zeeuw, P. T. 2008, MNRAS, 385, 647, doi: 10.1111/j.1365-2966.2008.12874.x

26

van der Marel, R. P., Cretton, N., de Zeeuw, P. T., & Rix, H.-W. 1998, ApJ, 493, 613, doi: 10.1086/305147

van der Marel, R. P., & Franx, M. 1993, ApJ, 407, 525, doi: 10.1086/172534

Vasiliev, E., & Athanassoula, E. 2015, MNRAS, 450, 2842, doi: 10.1093/mnras/stv805

Vasiliev, E., & Valluri, M. 2020, ApJ, 889, 39, doi: 10.3847/1538-4357/ab5fe0

Veale, M., Ma, C.-P., Greene, J. E., et al. 2017, MNRAS, 471, 1428, doi: 10.1093/mnras/stx1639

Verolme, E. K., Cappellari, M., Copin, Y., et al. 2002, MNRAS, 335, 517, doi: 10.1046/j.1365-8711.2002.05664.x

Virtanen, P., Gommers, R., Oliphant, T. E., et al. 2019, arXiv e-prints, arXiv:1907.10121. https://arxiv.org/abs/1907.10121

Virtanen, P., Gommers, R., Oliphant, T. E., et al. 2020, Nature Methods, 17, 261, doi: 10.1038/s41592-019-0686-2

Weijmans, A.-M., de Zeeuw, P. T., Emsellem, E., et al. 2014, MNRAS, 444, 3340, doi: 10.1093/mnras/stu1603

White, S. D. M. 1979, MNRAS, 186, 145, doi: 10.1093/mnras/186.2.145

York, D. G., Adelman, J., Anderson, Jr., J. E., et al. 2000, AJ, 120, 1579, doi: 10.1086/301513

Zhu, L., van de Ven, G., Méndez-Abreu, J., & Obreja, A. 2018a, MNRAS, 479, 945, doi: 10.1093/mnras/sty1521

Zhu, L., van den Bosch, R., van de Ven, G., et al. 2018b, MNRAS, 473, 3000, doi: 10.1093/mnras/stx2409

Zhu, L., van de Ven, G., van den Bosch, R., et al. 2018c, Nature Astronomy, 2, 233, doi: 10.1038/s41550-017-0348-1

Zhuang, Y., Leaman, R., van de Ven, G., et al. 2019, MNRAS, 483, 1862, doi: 10.1093/mnras/sty2916

APPENDIX

A. RADIAL COVERAGE TEST

The SAMI instrument has a fixed field of view ($15''$ diameter), meaning that each galaxy has a different maximum radial coverage. In particular, the most massive galaxies are larger than the SAMI field of view ($R_e > 25''$) and therefore only their inner region is observed ($R_{max} < 1R_e$).

In order to test the reliability of results obtained from applying Schwarzschild models to galaxies with measurements that do not reach the same maximum radial extension and have a limited number of spatial bins, we selected a test sample consisting of 20 randomly selected CALIFA galaxies, covering different radial extents (Fig. 19). For each galaxy we have taken the CALIFA stellar kinematic maps (Falcón-Barroso et al. 2017) and masked them at different radii, in order to have maps for each galaxy that extend up to $R_{max} = 0.5R_e$, $1R_e$, $1.5R_e$ and $2R_e$ (when possible), respectively. We then determined the best-fit model for each realization of the maps, in addition to fitting the whole galaxy (a set of up to 5 maps for each galaxy, depending on their radial coverage). We take the effective radius R_e from Falcón-Barroso et al. (2017).
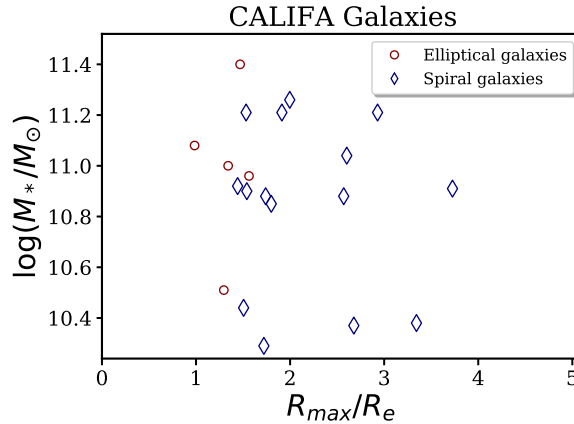

Figure 19. Maximum radial extension (in units of R_e) of the 20 CALIFA galaxies in our test sample. Elliptical galaxies are shown as dark red circles, spiral galaxies as dark blue diamonds. Seven of the galaxies have kinematic maps which extend beyond 2 R_e.

For each of the 20 galaxies in our test sample we compare the retrieved orbital distributions, inclination angle of the galaxy, enclosed dark matter mass and enclosed total mass within $1R_e$, for the five different kinematic maps, to those obtained by Zhu et al. (2018a). In most cases (16/20), the best-fit models reproduce the observed luminosity, velocity and velocity dispersion maps when all the parameters are unconstrained. **However, the models are better able to reproduce the observations (particularly the velocity dispersion) when they are also allowed to model the higher-order stellar kinematic moments (h_3 and h_4), even though they are set to zero, with uncertainties set to 0.5**. We show an example fit in Fig. 20 and 21. The reduced χ^2 decreases significantly from $\chi^2_{red} = 23.71$ when the higher-order moments are not included in the fit, to $\chi^2_{red} = 4.52$ when h_3 and h_4 are free parameters.

In general, our retrieved best-fit values of orbital weights and enclosed mass are comparable to those found in Zhu et al. (2018a). However, galaxies that are found to have low inclination angle ($\approx 40°$ - $50°$) in Zhu et al. (2018a) have a higher inclination angle in our best-fit model ($\approx 65°$). Moreover, due to the higher inclination angle, these galaxies show a lower fraction of cold orbits (required to reproduce the observed velocity dispersion). We note that those galaxies with a low observed inclination angle require stricter priors for the intrinsic shape parameters.
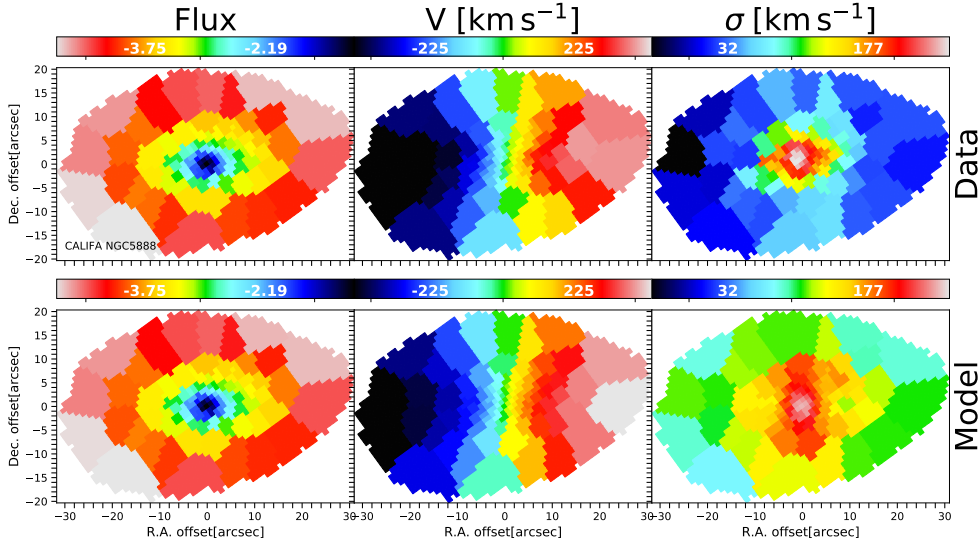
Figure 20. Best-fit model for CALIFA test galaxy NGC5888 using 2-moments maps. Top: Observed luminosity, velocity and velocity dispersion Bottom: best-fit model luminosity, velocity and velocity dispersion. The model does not reproduce the velocity dispersion well.
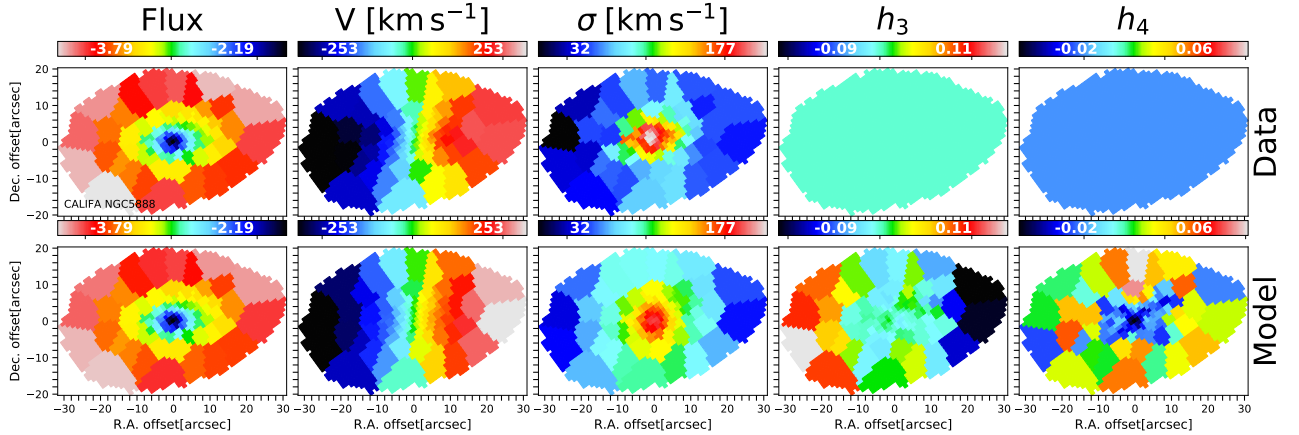
Figure 21. Best-fit model for CALIFA test galaxy NGC5888 using 2-moments maps as per Fig. 20, including the higher-order stellar kinematic moments (h_3 and h_4, set to zero) in the fits. Even though the values of the observed h_3 and h_4 are set to zero, the model is better able to reproduce the velocity dispersion map compared to Fig. 20.

Fig. 22 shows the average residuals between the derived orbital fractions of each of the 4 maps from the values derived from the total maps for the galaxies in our test sample. For each map, the residual for each orbital component is given by:

$$\delta = \frac{f_{orb_{TOT}} - f_{orb_{map}}}{f_{orb_{TOT}}} \tag{A1}$$

where $f_{orb_{TOT}}$ is the orbital fraction for cold, warm, hot or counter-rotating (CR) - derived from the total map and $f_{orb_{map}}$ is the orbital fraction derived for one of the 4 kinematic maps - $R_{max} = 0.5R_e$, $1R_e$, $1.5R_e$ and $2R_e$. Each point in Fig. 22 shows the average of the 4 residuals (one for each orbital component), color-coded by the R_{max} of the maps. **We also show the residuals for the fraction of dark matter within $1R$ (f_{DM}), the mass-to-light**

1713 **ratio in the r-band (M/L_r) and the intrinsic axis ratios at $1R_\mathrm{e}$ - p_Re and q_Re in Fig. 23.** The average
1714 residuals for each of the maps is shown in Table 1.

1715   Comparing the derived values within $1R_\mathrm{e}$ of the different maps for each galaxy, we find a general good agreement for
1716 all input R_{max} maps, with the exception of those retrieved from the $R_{max} = 0.5R_\mathrm{e}$ maps, which show a large scatter.
1717 We are therefore confident in the values estimated within $1R_\mathrm{e}$ calculated using maps that extend to at least $1R_\mathrm{e}$ for
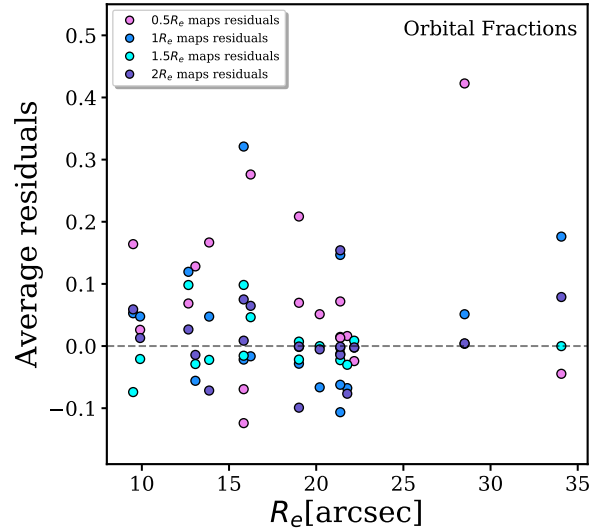1718 the analysis presented here.

Figure 22. Average residuals between the derived orbital fractions of each of the 4 maps from the values derived from the total maps for the galaxies in our test sample, as a function of R_e. For each map, the residuals of the four orbital components are calculated following A1 and then averaged over the orbital components. Each point corresponds to the average value, color-coded by the value of R_{max} of the map as shown in the bottom right corner. Comparing the derived values within $1R_\mathrm{e}$ of the different maps for each galaxy, we find a general good agreement for all input R_{max} maps, with the exception of those retrieved from the $R_{max} = 0.5R_\mathrm{e}$ maps, which show a large scatter.

Radial Coverage	Residuals				
	Orbital Fractions	f_DM	M/L_r	p_{Re}	q_{Re}
$0.5R_\mathrm{e}$	0.080	0.145	0.046	0.428	-0.012
$1R_\mathrm{e}$	0.030	0.086	0.047	0.101	-0.001
$1.5R_\mathrm{e}$	0.001	0.015	0.009	0.027	-0.001
$2R_\mathrm{e}$	0.011	0.002	0.016	-0.013	-0.001

Table 1. Average residuals between the derived orbital fractions, **fraction of dark matter within $1R_\mathrm{e}$, mass-to-light ratio in the r-band ($M_\star/L_r$) and intrinsic axis ratios p_{Re} and q_{Re}** of each of the 4 maps from the values derived from the total maps for the galaxies in our CALIFA test sample. Comparing the derived values within $1R_\mathrm{e}$ of the different maps for each galaxy, we find a general good agreement for all input R_{max} maps, with the exception of those retrieved from the $R_{max} = 0.5R_\mathrm{e}$ maps, which have larger average residual.

1719   B. EXAMPLE GALAXIES 9403800123, 9011900793, 220465 AND 9008500323

1720   **The parameter space for the complete model runs for example galaxies 9403800123, 9011900793,**
1721 **220465 and 9008500323 (Fig. 3,4,5 and 6) are shown in Fig. 24, Fig. 25, Fig. 26 and in Fig. 27,**
1722 **respectively.** The dots represent the parameters we have explored. Models within the best-fit region are color-coded
1723 according to their χ^2 values. The largest red dot highlighted with a black cross indicates the best-fit model. Fig. 28
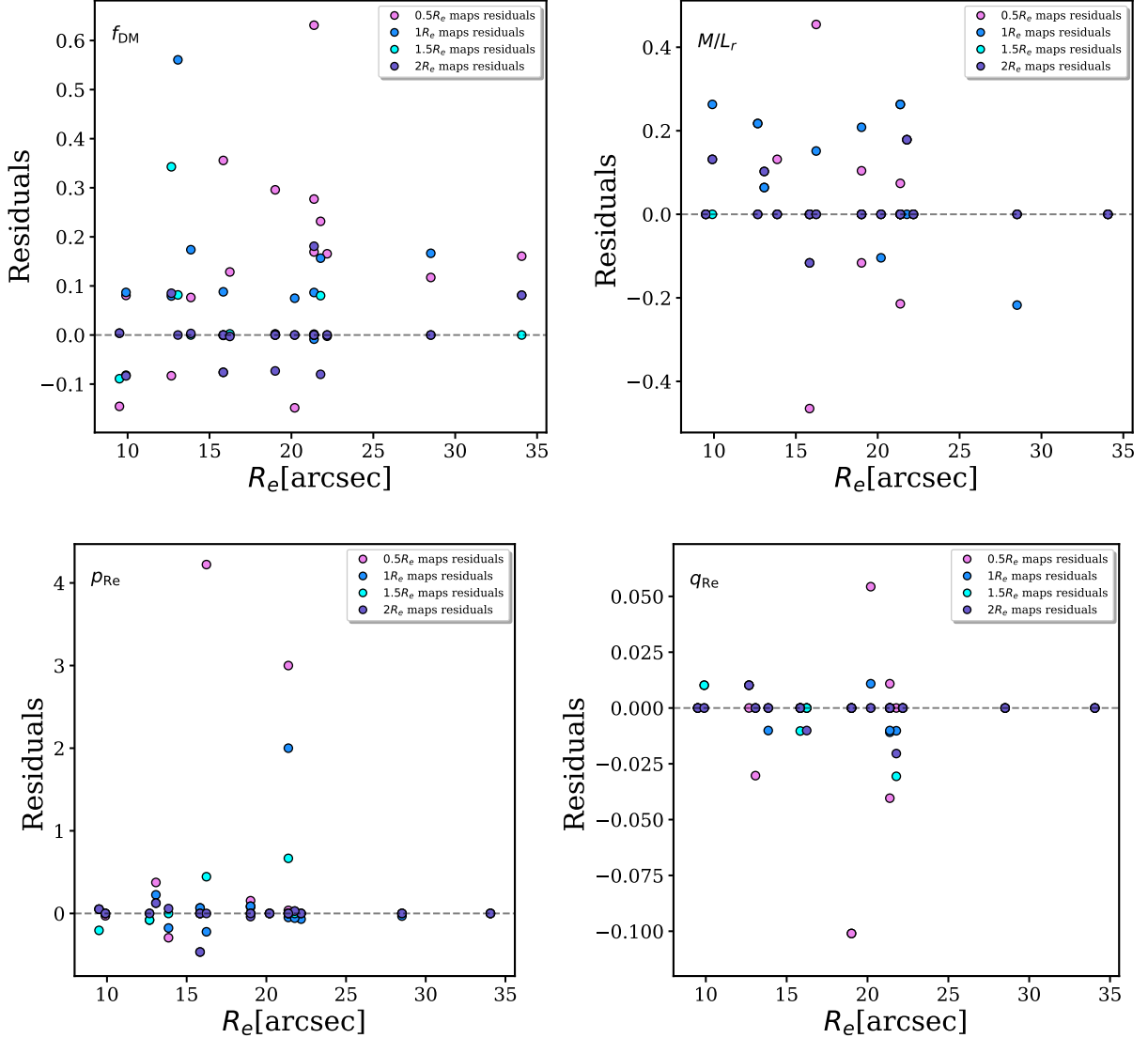
Figure 23. Average residuals between the derived fraction of dark matter within $1R_e$ (f_{DM}; **top left**), mass-to-light ratio in the r-band ($M_\star/L_r$; **top right**) and intrinsic axis ratios p_{Re} (**bottom left**) and q_{Re} (**bottom right**) of each of the 4 maps from the values derived from the total maps for the galaxies in our test sample, as a function of R_e. For each map, the residuals of the four orbital components are calculated following **A1**. Each point is color-coded by the value of R_{max} of the map as shown in the bottom right corner. Comparing the derived values within $1R_e$ of the different maps for each galaxy, we find a general good agreement for all input R_{max} maps, with the exception of those retrieved from the $R_{max} = 0.5R_e$ maps, which show a large scatter.

to Fig. 31 show the obtained internal mass distribution, orbit circularity, triaxiality and tangential anisotropy for the four galaxies.

C. UNCERTAINTIES ON THE MODEL BEST-FIT PARAMETERS

In addition to the 1σ fluctuations from the best-fit model, we use Monte Carlo realisations to estimate the uncertainties on our best-fit values. To this end, we select 16 SAMI galaxies ($\sim 10\%$ of the total sample), spanning different regions in the size - stellar mass plane. We apply Monte Carlo realisations, as described below, to each one of them, and we use the resulting variations from the best-fit parameters as the uncertainties for galaxies located in similar locations of the galaxy mass-size plane. For each galaxy, we take the kinematic values from the best-fit model and perturb them by adding noise, taken from a Gaussian distribution with standard deviation equal to the mean error of
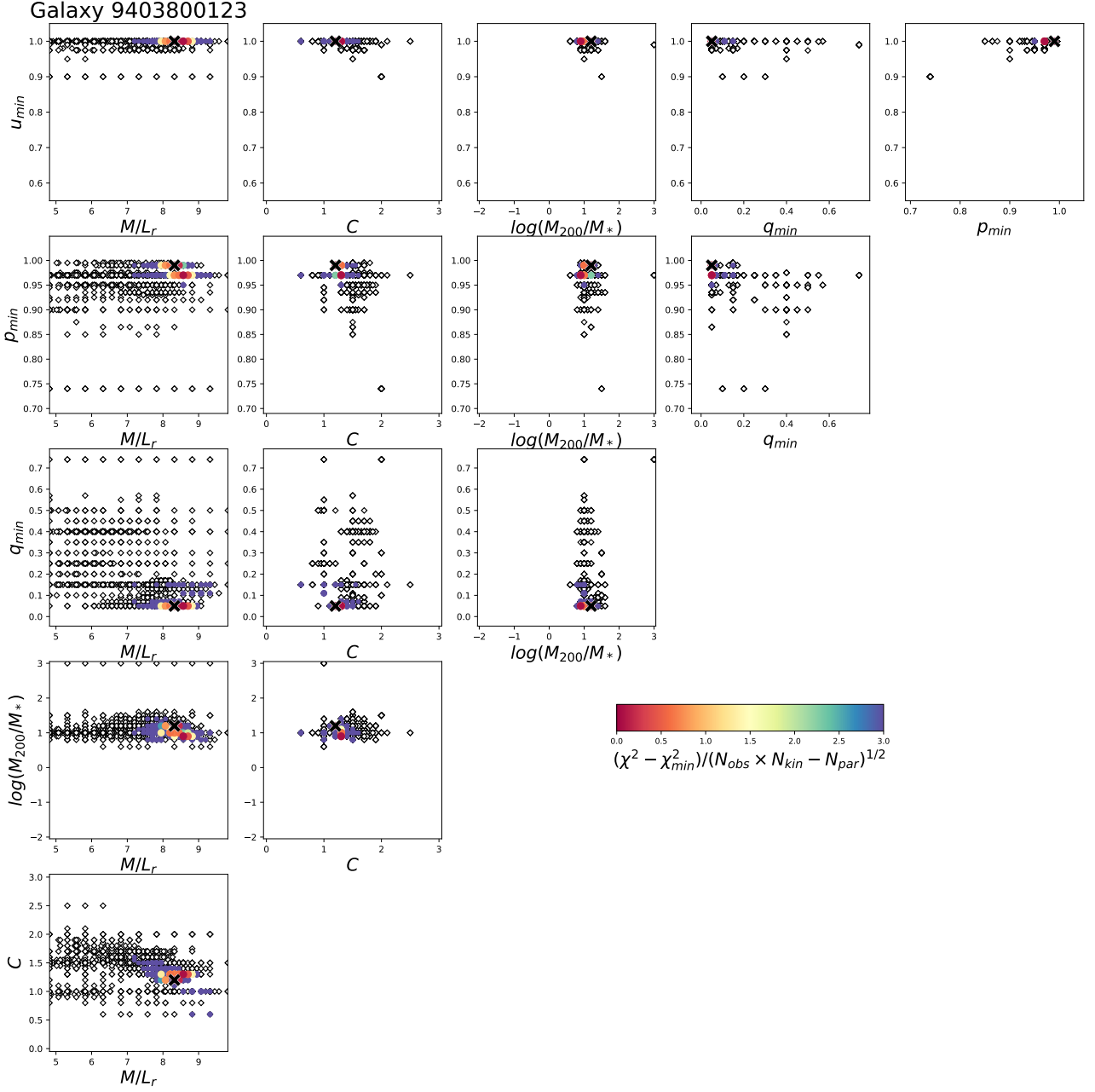
Figure 24. Example galaxy 9403800123: model parameter grid. There are six free parameters: stellar mass-to-light ratio, $M_\star/L_r$ in solar units, the intrinsic shape of the flattest Gaussian component (p_{min}, q_{min}, u_{min}), the dark matter halo concentration, $\log c$, and dark matter fraction, $\log M_{200}/M_\star$. The diamonds represent the parameters explored, with the best-fit model highlighted with a black cross. Models within the best-fit region are color-coded according to their χ^2 values shown in the color bar. The best-fit values are well constrained.

Figure 25. Example galaxy 9011900793: model parameter grid. The diamonds represent the parameters explored, with the best-fit model highlighted with a black cross. Models within the best-fit region are color-coded according to their χ^2 values shown in the color bar.

each observed kinematic moment (V, σ, h_3, h_4). We keep the standard deviation as the uncertainty for each perturbed value. We tested repeating this process to have 30, 50 and 100 different realisations. We then derive the best fit for each of the perturbed kinematic maps. We compare the orbital weights retrieved from each realisation and we find that there is in general good agreement, in particular when looking at the fitted inclination angle and the internal mass distributions values. The left-hand plot of Fig 32 shows the average of the best-fit parameters derived for 30

Figure 26. Example galaxy 220465: model parameter grid. The diamonds represent the parameters explored, with the best-fit model highlighted with a black cross. Models within the best-fit region are color-coded according to their χ^2 values shown in the color bar.

Monte Carlo realisations of the best-fit model of example galaxy 91963. We find that the fraction of the orbits in passive galaxies follow a unimodal distribution. This becomes more evident when considering 50 or 100 realisations (right-hand panels of Fig. 32). We therefore decided to use 50 Monte Carlo realisations as a good compromise in deriving the uncertainties on the best-fit values for SAMI galaxies, since 100 realisations for even 16 galaxies are unfeasibly time-consuming.
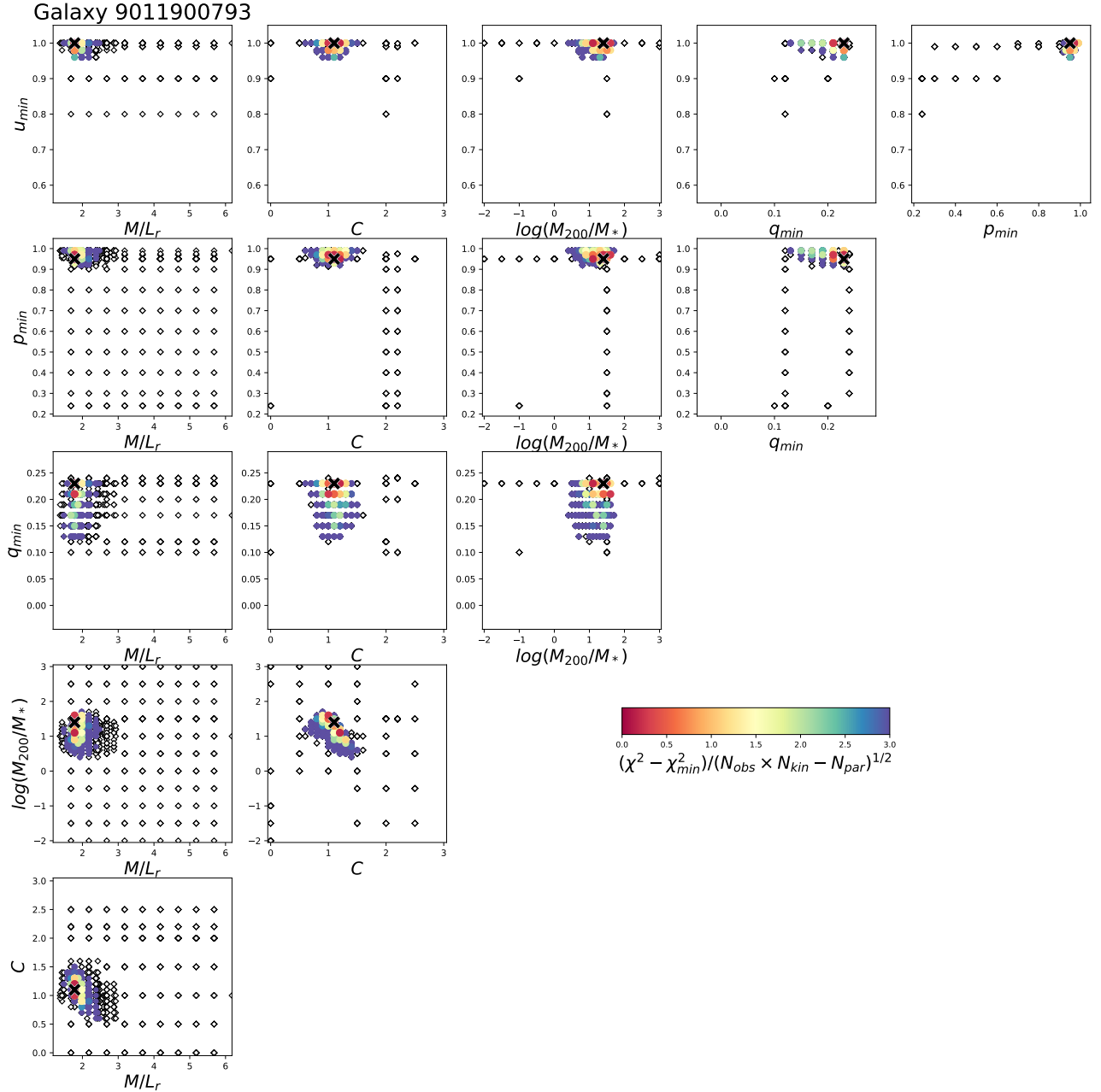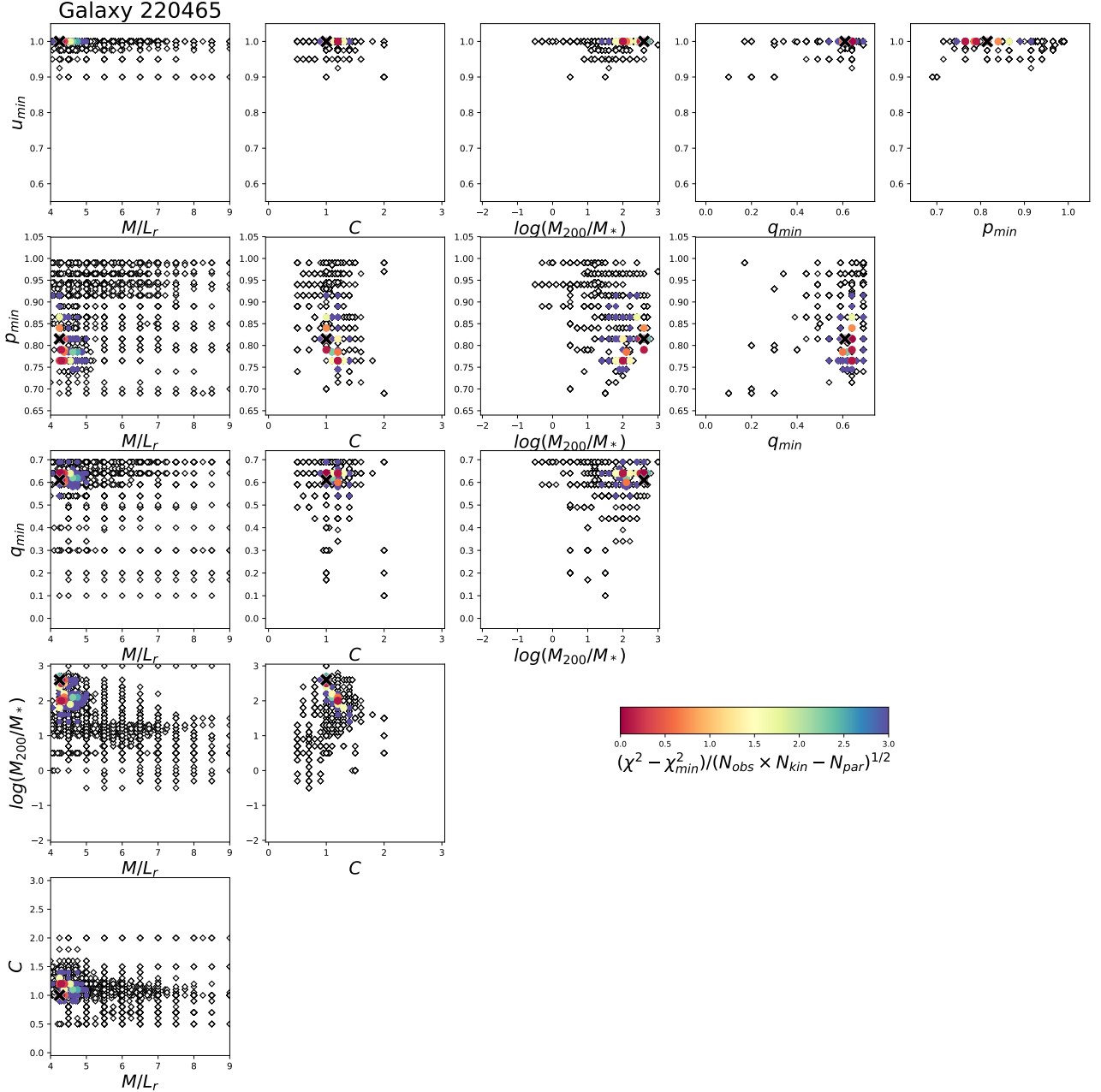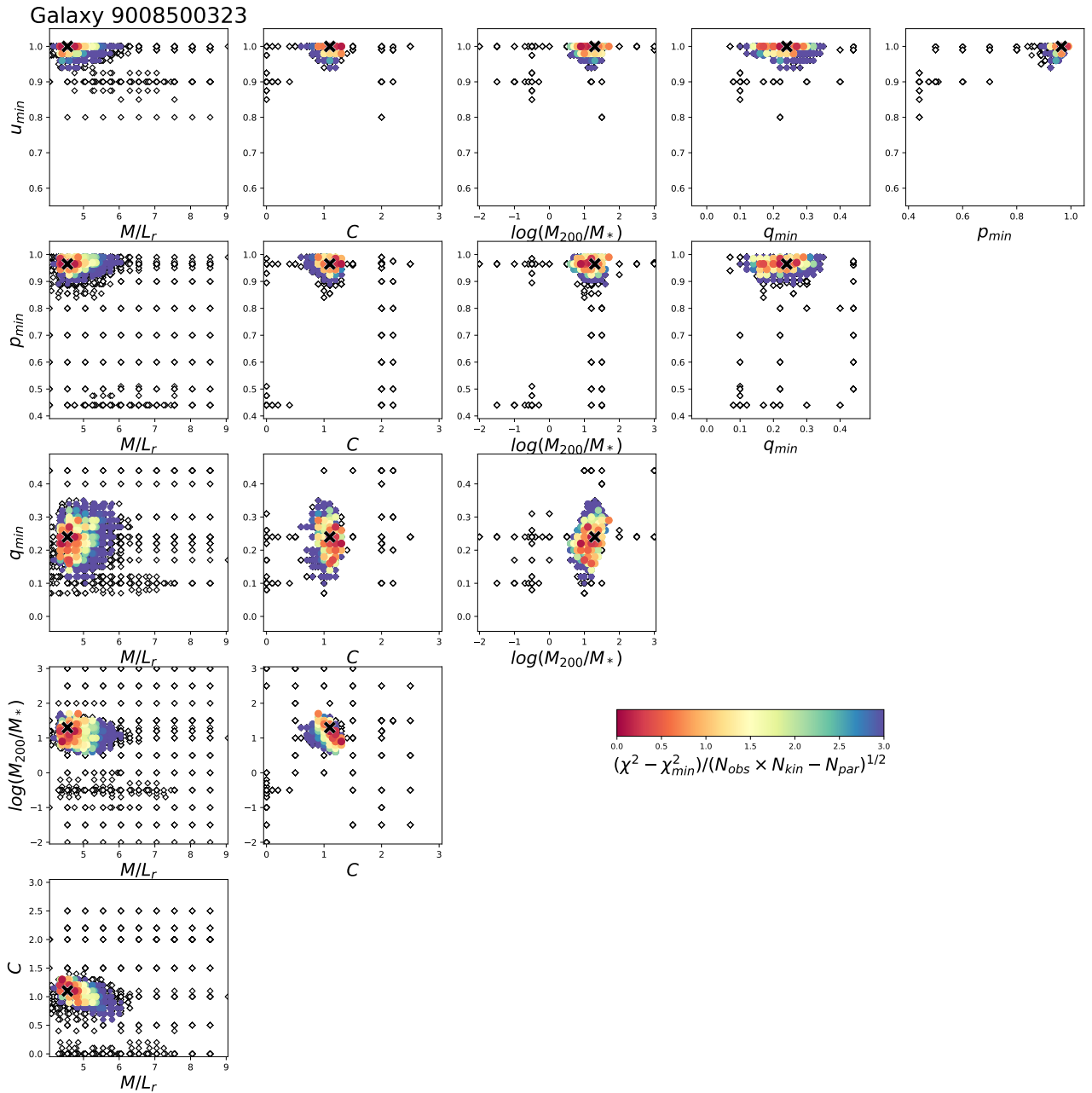
Figure 27. Example galaxy 9008500323: model parameter grid. The diamonds represent the parameters explored, with the best-fit model highlighted with a black cross. Models within the best-fit region are color-coded according to their χ^2 values shown in the color bar.

We take the difference between the 1-σ values of each distribution and the best-fit value of the observed kinematic map as the uncertainties (asymmetric, if the best-fit value is not in the centre of the distribution) on the retrieved best-fit parameters. To the uncertainty of each parameter derived with this method we also add, in quadrature, the 1σ confidence level from the parameter grid, which represents the model fluctuations. This method is applied to derive the uncertainties of all the quantities presented in this work.

Figure 28. Example galaxy 9403800123 (top left panel), 9011900793 (top right panel), 220465 (bottom left panel) and 9008500323 (bottom right panel): enclosed mass. Cumulative total mass (in black), stellar mass (in red) and dark matter mass (in blue) as a function of the radius of the galaxy. Solid lines are the cumulative profiles calculated from the best-fit, while the filled regions indicate the errors. Grey dotted and dash-dotted lines are located at $1R_e$ and at R_{max}, respectively. At larger radii the dark matter contribution becomes more important.

D. VELOCITY ANISOTROPY PARAMETER, β_Z

We define the velocity anisotropy parameter, β_z, in cylindrical coordinates, following Cappellari et al. (2007):

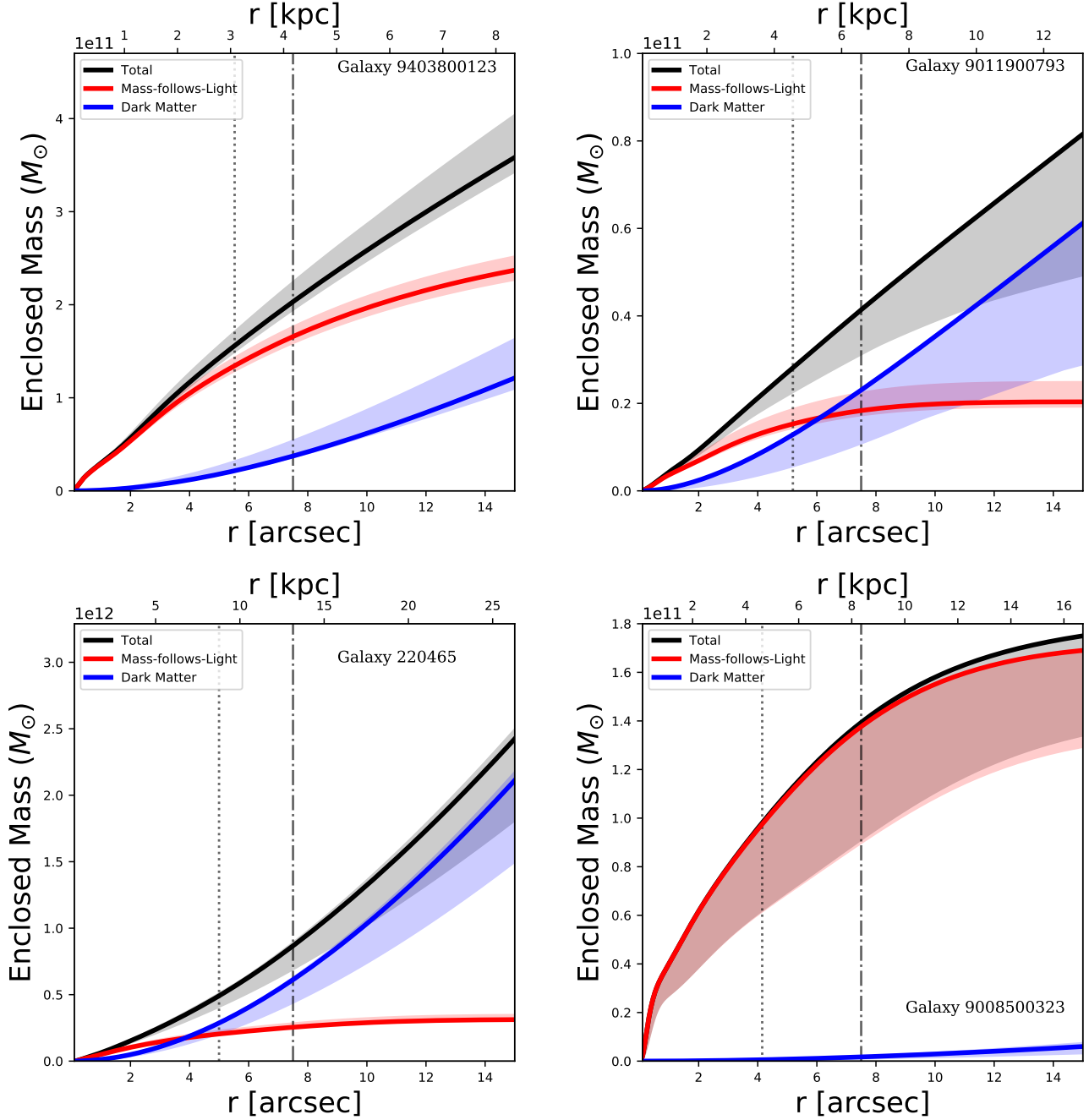$$\beta_z = 1 - \frac{\Pi_{zz}}{\Pi_{RR}}, \tag{D2}$$

Figure 29. Example galaxy 9403800123 (top left panel), 9011900793 (top right panel), 220465 (bottom left panel) and 9008500323 (bottom right panel): orbit circularity. The orbit distribution on the phase space of circularity λ_z versus radius of the best-fit model. The colour indicates the density of the orbits on the phase space, the three horizontal black dashed lines indicate $\lambda_z = 0.8$, $\lambda_z = 0.25$ and $\lambda_z = $ -0.25, dividing the orbits in four regions (cold, warm, hot and counter-rotating orbits). The vertical grey dotted and dash-dotted lines are located at $1R_e$ and at R_{max}, respectively. **Galaxy 9403800123 has is dominated by warm and cold orbits. Galaxies 9011900793, 220465, 9008500323 are dominated by hot orbits, but galaxy 9011900793 also has contributions from warm and cold orbits.**

1749 with Π_{kk} as defined in Equation 5. This parameter describes the global shape of the velocity dispersion tensor in the
1750 (v_R, v_z) plane. We calculate the value of β_z within $1R_e$, excluding the inner regions ($r < 2''$) since this is smaller than
1751 the FWHM of the PSF of our observations.

1752 Fig. 33 shows the derived values of β_z at $1R_e$, for each galaxy, as a function of intrinsic ellipticity ($\varepsilon = 1 - q$).
1753 Galaxies with higher ellipticities have higher values of β_z. This means that flatter galaxies are more anisotropic than
1754 rounder galaxies. The grey line shows the relation $\beta_z = 0.7 \times \varepsilon_{intr}$ from Emsellem et al. (2007). In general, we find
1755 higher values of β_z compared to those seen in Cappellari et al. (2007) for the early-type galaxies in their sample from
1756 the SAURON survey. However, they applied axisymmetric Schwarzschild dynamical models to only 24 of their galaxies
1757 (a subsample that was consistent with axisymmetry), while the Schwarzschild dynamical models we use also include a
1758 set of box orbits that allow for triaxiality. Therefore, the scatter that we see in our relation, is likely to be due to the
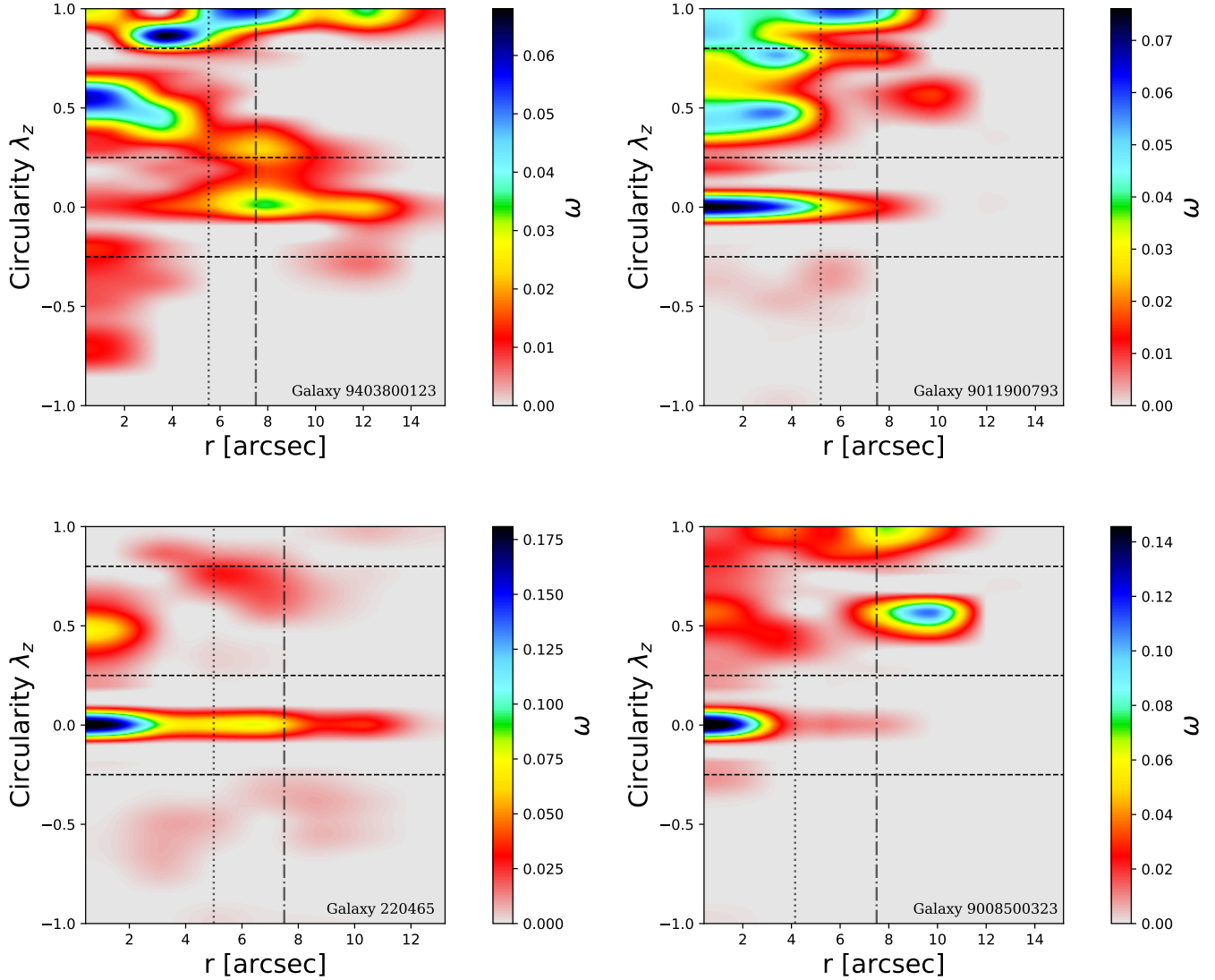
Figure 30. Example galaxy 9403800123 (top left panel), 9011900793 (top right panel), 220465 (bottom left panel) and 9008500323 (bottom right panel): triaxiality. Variation of the axial ratios $p = b/a$, $q = c/a$ and triaxial parameter $T = (1 - p^2)/(1 - q^2)$. The red, blue and black curves correspond to p, q and T. The filled regions indicate the errors and the grey shaded region indicates the seeing limit ($r < 2''$). The vertical grey dotted and dash-dotted lines are located at $1R_{\mathrm{e}}$ and at R_{max}, respectively. **9403800123 and 9011900793 are oblate in shape, while 220465 is triaxial and 9008500323 is close to prolate.**

contribution from hot orbits. This is better shown by color-coding the galaxies in the $\beta_z - \varepsilon$ plane by their fraction of hot orbits. As seen in Fig. 33, we have contributions $> 20\%$ from hot orbits in all of the galaxies in our sample. The negative β_z values that we find can be explained with the velocity ellipsoids not being cylindrically aligned, as mentioned in Sec. 4.3.
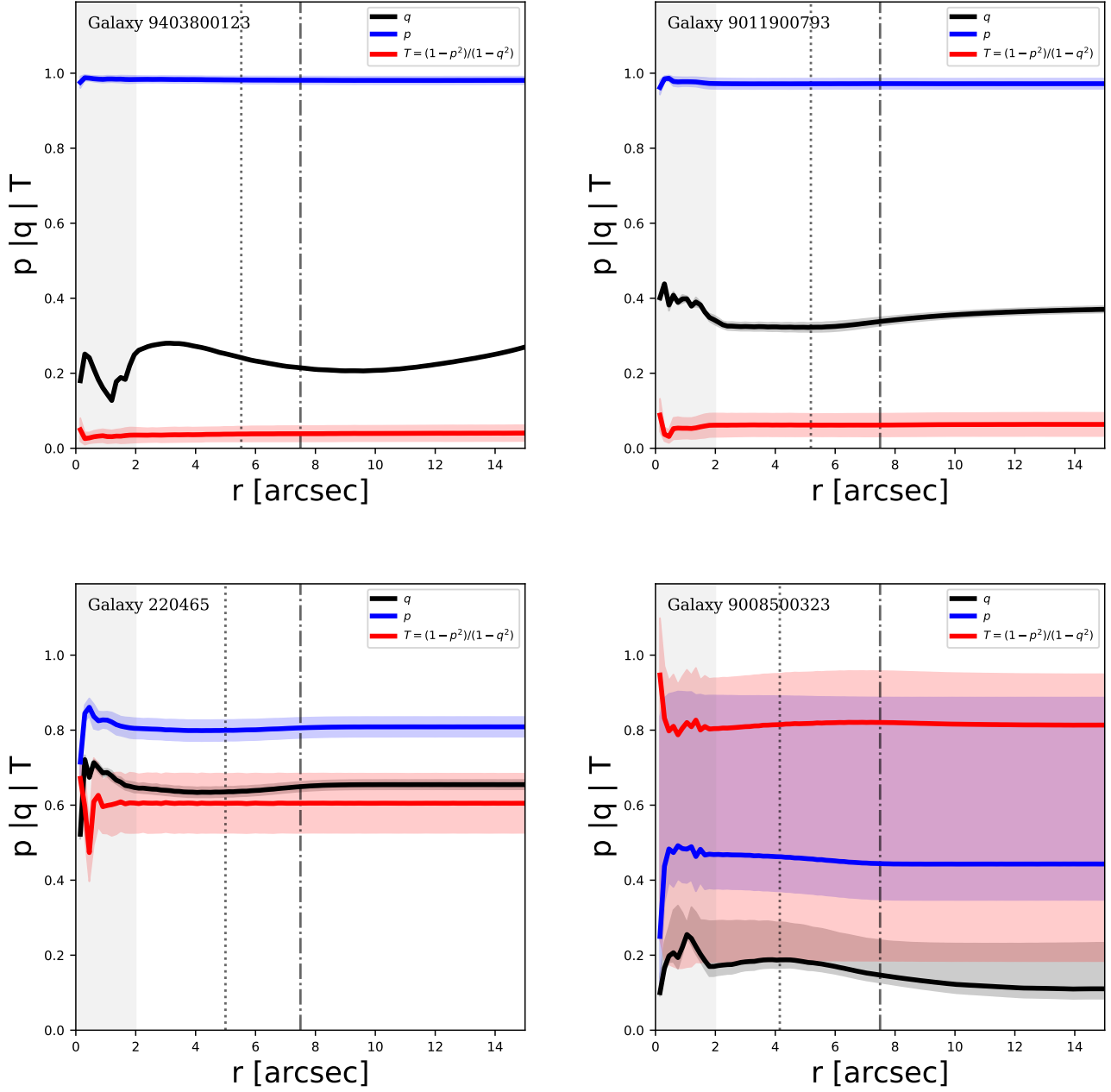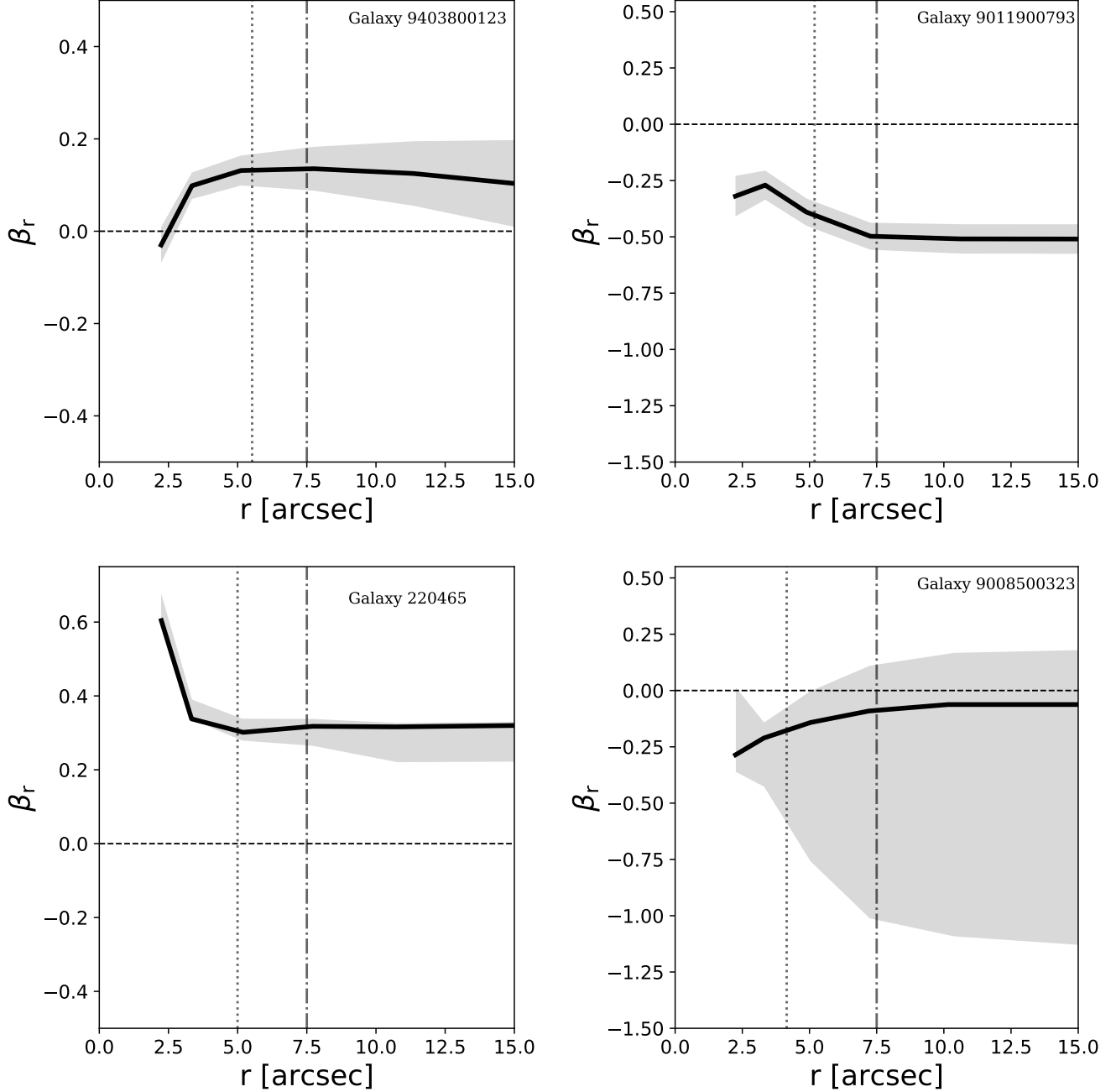
Figure 31. Example galaxy 9403800123 (top left panel), 9011900793 (top right panel), 220465 (bottom left panel) and 9008500323 (bottom right panel): velocity anisotropy profile, β_r, as a function of the radius. The solid curves represent the velocity anisotropy profile obtained by the best-fit model. The filled region indicates the errors. The vertical grey dotted and dash-dotted lines are $1R_e$ and R_{max}, respectively.

E. RATIO OF ORDERED TO RANDOM MOTION

For completeness, we also measure the ratio of ordered to random motion V/σ, also measured within $1R_e$, using the definition from Cappellari et al. (2007):

$$(V/\sigma)^2 = \frac{\sum_{i=0}^{N_{spx}} F_i V_i^2}{\sum_{i=0}^{N_{spx}} F_i \sigma_i^2}. \tag{E3}$$
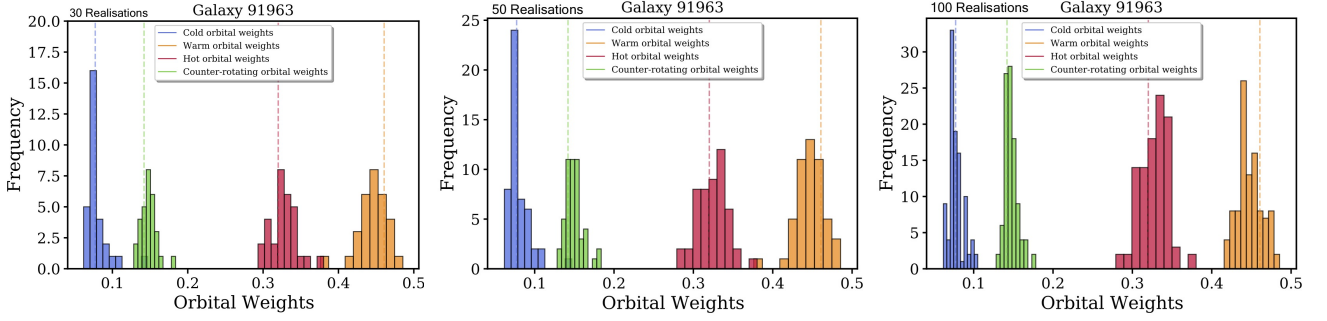
Figure 32. Distribution of the orbital weights for the Monte Carlo realisations around the best-fit model values found for example galaxy 91963. Left-hand plot: 30 realisations; central plot: 50 realisations; right-hand plot: 100 realisations. The dashed lines represent the best-fit values. The unimodal distributions of the orbital components become more evident when increasing the number of realisations. We use 50 Monte Carlo realisations to derive the uncertainties for our galaxies to optimise the model run-time required.
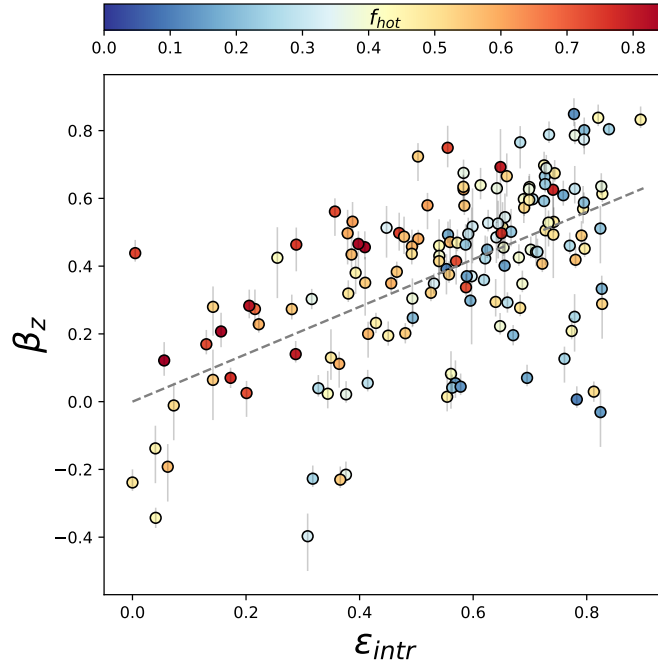
Figure 33. Velocity dispersion anisotropy, β_z, within $1R_e$ as a function of intrinsic ellipticity ($\varepsilon = 1 - q$), color-coded by their fraction of hot orbits. The grey line shows the relation $\beta_z = 0.7 \times \varepsilon_{intr}$ from Cappellari et al. (2007). Galaxies with higher ellipticities have higher values of β_z. This means that flatter galaxies are more anisotropic than rounder galaxies.

Results obtained using V/σ are similar to those obtained for $\lambda_{Re,EO}$ (see Fig. 11 in Sec. 4.4) and are shown in Fig. 34.
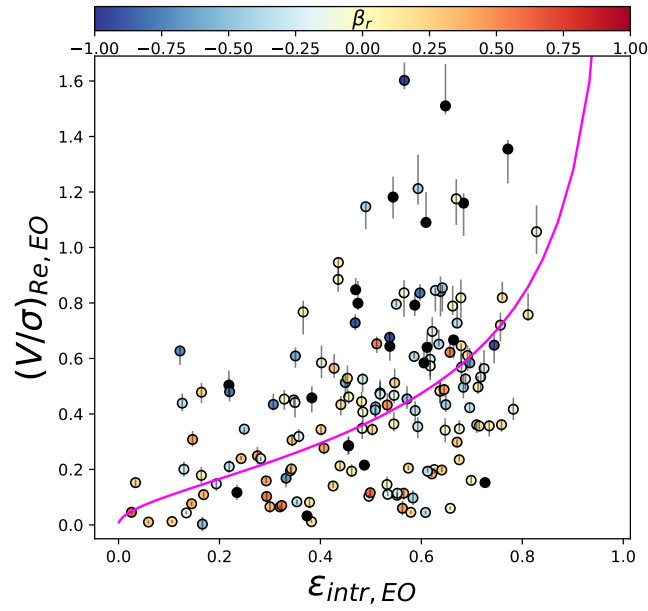
Figure 34. V/σ as a function of the ellipticity $\varepsilon_{intr,EO}$ derived from MGE fits to the edge-on projected maps, calculated at $1R_e$. The magenta line corresponds to the relation $\beta_z = 0.7\varepsilon$ for edge-on galaxies (Emsellem et al. 2007). Data points are color-coded by the velocity anisotropy β_r. As expected, V/σ increases with increasing intrinsic ellipticity.

We thank the anonymous referee for their careful reading of the paper and their constructive comments. We have addressed their concerns as described below. Our comments are highlighted in bold font here, and new text is highlighted in bold font throughout the updated paper.

1) A recent manuscript by Quenneville et al. 2021 was posted to arXiv highlighting issues with the Schwarzschild code used here, and their findings could significantly impact this work. Given Quenneville et al. 2021, I recommend the orbital mirroring mistake in code be corrected so that the positions and velocities combine to give a valid trajectory for the the tube orbits. In addition, given the periodic oscillation Quenneville et al. found in chi^2 with the triaxiality parameter for some n_l2 values, exploring the orbital sampling should be done here too. An oscillation in triaxiality parameter could cause an iterative grid search to get stuck in a local minimum.

Moreover (independent of the Quenneville et al. 2021 results), the authors should demonstrate that the sampling with the iterative grid search is sufficient for this data set. For example, Section 4 states that on average 500 models are built for each galaxy. Even if all 500 models were run for just the initial sampling stage, assuming uniform spacing in all six dimensions, then only 2-3 values were sampled along each dimension. So either a small range for each parameter is being examined or the sampling is sparse.

Schwarzschild models are time intensive and applying them to a large galaxy sample is incredibly challenging, particularly now that the authors are using triaxial models and have a six-dimensional space to explore. However, conducting detailed tests and describing the results of those tests for several galaxies in sample is necessary to demonstrate the robustness of the results for the larger sample. While the results for two example galaxies with different numbers of spatial bins within ~1.4-1.7 Re are presented and Appendix A describes a test related to the kinematic extent of the data, galaxies with different intrinsic shapes should also be explored. Therefore, as a start, it would be good to select, at a minimum, four galaxies - two oblate axisymmetric galaxies with different inclination angles (edge-on and not edge-on), a triaxial galaxy, and a prolate galaxy, as determined from the current models. If possible, it would be even better to select more than one galaxy from each group and include objects with data covering differing radial extents. Then, correct the orbital mirroring mistake, and re-run the models for the example galaxies to assess the impact. Also, for these example galaxies, explore the orbital sampling, using different values of n_l2 to see if the iterative grid search, as is, recovers the same parameters. Finally, for the example galaxies, increase the sampling used for the iterative grid search, running different numbers of models for both the initial sampling stage and over all iterations to see how the inferred parameters and their uncertainties change.

We have fixed the mirroring mistake in the code and rerun the models for the entire sample. Our new results have not significantly changed the key results in our paper. The impact of the fix on the retrieved values from the models in our data and previous data is also being explored in collaboration with the DYNAMITE team in detail and will be presented soon. Minor changes were made to the text in Section 4 (values of the derived quantities and kendall tests' values - highlighted in bold). However, moderate changes have been made to Section

4.2 - showing the intrinsic shape distribution. We have updated the figures (Fig. 3 to Fig. 18 and Fig. 24 to Fig. 34) with the new derived properties.

We have selected 4 galaxies as example galaxies: 1 edge-on oblate, 1 non edge-on oblate, 1 triaxial and 1 prolate galaxy. As suggested by the referee, for these four galaxies we have increased n_l2 by a factor of 4, and re-fit the models. The best-fit values retrieved by this search are consistent, within the 1-sigma confidence level, with the best-fit values retrieved by our regular runs.

We have run an average of 1250 models for each galaxy in our sample. For the 4 example galaxies we have also increased the sampling used for the iterative grid search. The best-fit parameters for both the "standard" and the "super-sampled" grid search are consistent with one another within the 1-sigma confidence level, converging on global minima.

2.) What is the range of reduced chi^2 values for the sample? The paper doesn't report this information, or the typical value, but for the two example SAMI galaxies, the reduced chi^2 is ~4 and ~15. These, particularly the latter case, seem very high compared to reduced chi^2 values often found when using Schwarzschild models (e.g., Yildirim et al. 2017, Krajnovic et al. 2018, Zhu et al. 2018, Thater et al. 2019, Liepold et al. 2020). Usually the reduced chi^2 tends to be at or below 1, especially if the input kinematics are symmetrized. Are the kinematics here point symmetrized? The footnote explains that the high reduced chi^2 values are due to "variables being co-dependent". I'm not sure what is meant by that statement. The authors should clarify. If a reduced chi^2 close to 1 is not expected, what is considered a good model?

Also, since the SAMI galaxies have kinematics measured out to h4, given what was noted in Appendix A for the CALIFA test galaxies, what happens if h5 and h6 (or even going beyond to h7 and h8) are set to 0 and the model is allowed to fit to these higher moments? Will the fit significantly improve and the reduced chi^2 drop? If so, is there an impact on the inferred model parameters, or does the chi^2 surface remain the same shape but just the normalization change? This could be checked using the same example galaxies from comment #1 above. In addition, in Appendix A, when setting h3 and h4 to 0, what uncertainties for h3 and h4 are used?

The referee was correct in pointing out that the chi^2 values should be close to 1. We found a minor error in our final calculation of the reduced chi^2 where the chi^2 was calculated from the pixel values, but normalised by the number of Voronoi bins. The reduced chi^2 value is now calculated from the binned maps and normalised by the number of Voronoi bins. This resolved the issue with the high reduced chi^2 values. The range of reduced chi^2 for the sample has values between 0.54 and 8.12, with a mean value chi^2= 2.33 and a standard deviation of 1.34. The distribution of the reduced chi^2 is shown in the figure below. The average chi^2 value being greater than one is expected because the input kinematics are not symmetrised, while the models are.
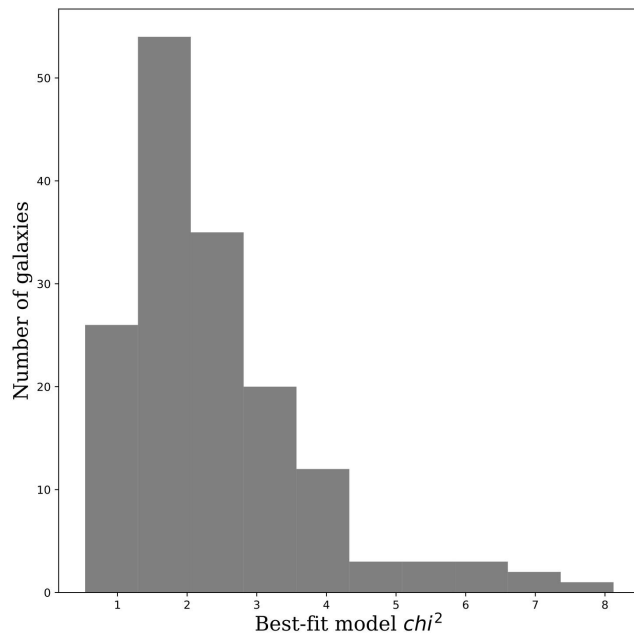
We have changed the footnote text in Sec. 3.4 as follows:
"*The values of chi^2 are not always equal to 1 for the best-fit models of the galaxies in our sample. This is because the input kinematic maps of the galaxies in our sample were not symmetrised. Therefore, comparing the observed maps to the model maps, which are symmetric, can result in values of chi^2 higher than 1."*

As suggested by the referee, we also tested whether including h5 and h6 made a significant difference to our best-fit model for the example galaxies. Fixing h5 and h6 to 0 and allowing the model to fit these higher moments does not significantly improve the fit. The variations in h5 and h6 are quite small (~0.06) and there are no significant changes in the kinematic fit, nor in the chi^2 (derived from the fit to the measured moments - for example chi^2 changed from 2.22 to 2.18 for galaxy 9403800123) level or morphology.

In Appendix A, we fixed the uncertainties of h3 and h4 to 0.5. This information has been added to the text in Appendix A as well:
"*However, the models are better able to reproduce the observations (particularly the velocity dispersion) when they are also allowed to model the higher-order stellar kinematic moments (h_3 and h_4), even though they are set to zero, with uncertainties set to 0.5."*

3.) Appendix A examines how the inferred orbital fractions depend on the radial extent of the data. What about other parameters, like the intrinsic shape, dark matter fraction, and M/L?

We have added Fig. 21 to show the variation of the intrinsic shape, the mass-to-light ratio and the dark matter fraction with the radial extent. Similar to the fractions of orbits, these parameters are well retrieved within 1 R_e when the radial coverage reaches at least 1 R_e (with less than 1% variation). When the radial coverage only reaches 0.5 R_e, the derived value of f_DM, for example, has an average variation of 15%, with some cases where it was

overestimated by over 30%. We have also added the residual values for the aforementioned parameters in Table 1, Appendix A and the following text:
"*We also show the residuals for the fraction of dark matter within 1$R_{\rm}$ ($f_{\rm DM}$), the mass-to-light ratio in the r-band (M/L_r) and the intrinsic axis ratios at 1$R_{\rm e}$ $p_{\rm Re}$ and $q_{\Re}$ in Fig. 21.*"

4.) In Section 2.4, the paper states that galaxies with irregularities in their kinematic maps, that have strong bars, or that have a bright object in the field were excluded from the sample. What is meant by irregularities in the kinematic maps? If the authors are referring to non-axisymmetric features like kinematic twists or misaligned kinematic and photometric position angles, why are the galaxies excluded from the sample? Triaxial stellar dynamical models should be able to reproduce those kinematic features. If such galaxies instead were fit, the percentage of galaxies that fall into the oblate, triaxial, and prolate categories in Section 4.2/Figure 6/Section 6.1.2, the abstract, and conclusion may change, so that choice in the sample selection and the possible implication should be made clear.

By 'irregularities' we mean kinematic maps of galaxies that are affected by mergers, secondary galaxies, nearby objects that influence the stellar kinematics of the main object or artificial features due to a poor-fit that were visually identified, not misalignments or non-artificial kinematic features in the kinematic maps. We have corrected the text in Sec 2.4 to clarify:
"*Following van de Sande et al. (2017a), we exclude all galaxies whose kinematics are influenced by mergers, that have strong bars or that have a bright object in their stellar velocity field.*"

5.) The stellar masses come from photometry and an assumed IMF. The stellar masses could also be derived from the MGEs and the M/L from the dynamical models. How do the two values compare? Can the authors comment on their preference to use stellar masses from the photometry instead of the dynamical models?

We choose to use the photometry-derived stellar masses to be consistent with the whole SAMI sample and previous results in the literature where the stellar mass presented was not the dynamical mass derived from the Schwarzschild modelling (e.g. CALIFA and MaNGA). Our derived dynamical mass shows a tight correlation with the photometric stellar mass, with some saturation at high stellar masses, consistent with what has been seen in the literature (e.g. Cappellari et al. 2006, van der Wel et al. 2008, Taylor et al. 2010, Newman et al. 2010, Cappellari et al. 2012) *. The following sentence has been added to Sec. 2.3:*
"We use the photometric stellar masses for our analysis in order to be consistent with previous SAMI studies and to have consistent comparisons with previous results in the literature (e.g. from CALIFA and MaNGA)."

6.) As mentioned in the introduction, one new aspect of this work compared to the orbit-based modeling of CALIFA and MaNGA galaxies is the use of h3 and h4. Is there anything to say about how the inclusion of h3 and h4 has been helpful for constraining the model parameters, whether similar future work should also strive to fit h3 and h4, or any other lessons learned?

Yes, as mentioned in the Appendix, including h3 and h4 in the fits improved the fit to lower moments. Future works should strive to fit h3 and h4 to include them in the modelling, since even values with high uncertainties can really improve the fits. Moreover, since h3 and h4 are quantities that are predicted to be connected with a galaxy's assembly history, studying their relation to the internal orbital structure of galaxies could help disentangling the different possible formation scenarios. We did not find a significant difference between the orbital components of fast-rotating galaxies in different classes (determined using the V/sigma- h3 correlation) in the lambda_z-r space (Fig. 14), but this is an interesting aspect that should be further explored in future works where more reliable values of h3 and h4 are available (e.g. the forthcoming Hector survey).

We have added the following text to Sec. 6:
"*We recommend the inclusion of the higher-order kinematic moments h_3 and h_4 in future works since even values with high uncertainties improve the model fits.*
***Moreover, since h_3 and h_4 are quantities that are predicted to be connected with a galaxy's assembly history (Naab et al. 2014), studying their relation to the internal orbital structure of galaxies provides an extra tool to help disentangle the different possible formation scenarios. We did not find a significant difference between the orbital components of fast-rotating galaxies in different classes (determined using the V/sigma- h3 correlation) in the lambda_z - r space (Fig. 14), but this is an interesting aspect that should be further explored in future works with larger samples of accurate h_3 and h_4 values (e.g. the forthcoming Hector survey; Bryant et al. 2016)*."**

Additional Minor Comments:

7.) Section 2.2 - it should be made clear that the position angle of the Gaussian components were required to be the same.

We have specified that the position angles of the Gaussian components were required to be the same in Sec 2.2 by adding the following sentence:
"*For each fit, the position angle of the Gaussian components were required to be the same.*"

8.) Figure 3 and Figure 4 - the labels and units for the x and y axes are missing. It is a little difficult to see the numbers associated with the color bar.

We have added the missing labels and made the numbers clearer.

9.) Figure 18 and Figure 19 in Appendix A - it is very difficult to see the values associated with the color bar. Also, numbers for the x-axis are missing, as are titles and units for the x and y axes.

Missing labels and numbers have been added and we have increased the size of the numbers in the color bars.

10.) Figure 21 and Figure 22 in Appendix B - it would be good to make it clear what band the M/L is in and that these are solar units.

We have added the information on the band (r-band) and the units.

11.) Section 4.4 - is there an understanding about why the re-projection did not work well for the 25 galaxies?

Yes, the issue was resolved by correcting the orbital mirroring mistake. We have removed the sentence from the paper.

12.) Section 5.1 and 5.2 - since the orbital circularity is within 1 Re and within R_max,h34, respectively, perhaps these sub-sections don't need to be distinct from the integrated properties section. It seems similar to the decision to include the T_Re, beta_r, and lambda_RE,EO sub-sections in the integrated properties section.

We agree with the referee and we have integrated Sec. 5.2 and Sec. 5.1 in Sec. 4

13.) Section 6.1.1 - if measurements of f_dm could be impacted by the form of the dark matter halo assumed, did the previous studies to which this work is compared to also assume an NFW profile?

Yes, the previous studies used for comparison all used a NFW dark matter profile. This has been clarified in the paper by modifying the following sentence in Sec. 5.1.1:

"In general, our results for f_DM are broadly consistent with previous stellar dynamic determinations within 1Re found in the literature which also all assume a NFW dark matter halo distribution."

14.) Figure 14 and Figure 15 - are there uncertainties on f_DM and the orbital fractions for the literature data points? Or, were they intentionally left off the plot?

We have added error bars identifying the 1-sigma scatter in the data points for each mass bin for CALIFA. The uncertainties for the other f_DM values and orbital fractions (that are taken as the values given by the authors in their papers), were not available.

Data Editor's review:
One of our data editors has reviewed your initial manuscript submission and has the following suggestion(s) to help improve the data, software citation and/or overall content. Please treat this as you would a reviewer's comments and respond accordingly in your report to the science editor. Questions can be sent directly to the data editors at data-editors@aas.org.

Per the AAS software policy, https://journals.aas.org/policy-statement-on-software/, the authors should modify their AASTeX v6+ manuscript to highlight the code they used (both cited and unmentioned in the current text) with the new \software command, e.g.

\software{pPXF (Cappellari & Emsellem 2004; Cappellari 2017), The Voronoi binning code of Cappellari & Copin (2003), DYNAMITE (Jethwa et al. 2020), MgeFit (Cappellari 2002), Scipy (Jones et al. 2001)}

We have added a line in the Acknowledgment section to highlight the code used: "\software{pPXF \citep{Cappellari2004, Cappellari2017}, MgeFit \citep{Cappellari2002}, Voronoi binning code \citep{Cappellari2003}, Scipy \citep{2020SciPy-NMeth}, UNSW Katana computational cluster \citep{Katana2010}.}"